Coherent Control of Photoassociation

Ruzin Ağanoğlu

Institut für Theoretische Physik

Freie Universität Berlin

A thesis submitted for the degree of

Doctor of Philosophy

Vorsitzender: Prof. Dr. Ludger Wöste
Freie Universität Berlin

Erstgutachter: Dr. Roland Mitrić
Freie Universität Berlin

Zweitgutachter: Prof. Dr. Christiane Koch
Universität Kassel

Mitglieder: Prof. Dr. Bretistav Friedrich
Fritz-Haber-Institut der Max-Planck-Gesellschaft, Berlin

Mitglieder: Dr. Beate Schattat
Freie Universität Berlin

Mitglieder: Dipl.-Phys. Oliver Gause
Freie Universität Berlin

Tag der Disputation: 23.01.2012

Zusammenfassung

In dieser Arbeit werden die Kohärenz Eigenschaften der Materie im Rahmen der Photoassoziation von ultrakalten Alkali-Atomen mit kurzen und ultrakurzen Laserpulsen untersucht.

Der ultrakalte Bereich kann mit Temperaturen unterhalb von 100μK beschrieben werden. Wenn die relevante Energien in der Nähe des ultrakalten Regimes ist, werden Quanten-Eigenschaften der Materie sichtbar. In diesem Regime zeigt Materie, wie Atome und Moleküle, Welleneigenschaften. Kohärente Kontrolle benutzt die Welleneigenschaften der Materie, um einen physikalischen Prozess in Richtung eines gewünschten Ziels zu lenken. Das kann mit kohärenter Strahlung wie Laser-Licht realisiert werden. Insbesondere können Femtosekunden-Laserpulse geformt werden. Sie sind damit zu einem Standardwerkzeug für kohärente Kontrolle geworden. Da die Materie ihre Welleneigenschaften am deutlichsten bei extrem niedrigen Temperaturen zeigt, stellt ultrakalte Materie das perfekte Objekt für kohärente Kontrolle dar. Die Verwendung inkohärenter Felder auf ultrakalte Materie gibt uns keine gute Möglichkeiten, ihre Quanten-Eigenschaften zu kontrollieren. Das Ziel dieser Arbeit ist es, ultrakalte und ultraschnelle Regime im Rahmen der Photoassoziation zusammen zu bringen. Photoassoziation, d.h. die Anregung von zwei kollidierenden Atomen durch Laserlicht, erzeugt sehr schwach gebundene Moleküle.

Im ersten Teil dieser Arbeit sind Femtosekunden-Photoassoziation-Experimente simuliert worden. In diesen Experimenten und Simulationen wird das breite Spektrum der Femtosekunden-Pulse, sowohl

atomarer als auch molekularer Übergänge, so manipuliert, dass atomaren Übergänge verhindert und die molekularen Übergänge gefördert werden. Dann werden die Wirkung von Chirp und der Effekt der zusätzlichen Phase auf den Puls untersucht. Die Population im angeregten Zustand und im Grundzustand wird mit Hilfe von Quantendynamischen Simulationen überprüft. Die treibende ultraschnelle Dipol-Dynamik wird vorgestellt.

Die Photoassoziation-Rate wird begrenzt durch die niedrige anfängliche Dichte von atomare Paaren mit einem Atomabstand, bei dem die Photoassoziation durchführbar ist.

Im zweiten Teil dieser Arbeit untersuchen wir eine neue Methode, welche Shape-Resonanzen benutzt, um die Dichte von atomaren Paaren mit dem richtigen Abstand für Photoassoziation, zu erhöhen.

Eine Shape-Resonanz ist ein metastabiler Zustand, welcher auftritt wenn ein Teil der Wellenfunktion die Rotationsbarriere bei $J>0$ überkommt, und einen gebundene Zustand bildet, wahernd der andere Teil der Wellenfunktion von der Barriere gestreut wird. Die meisten der Shape-Resonanzen in alkalischen und Erdalkalimetallen treten typischerweise bei Temperaturen von wenigen Milli-Kelvin auf. Deshalb ist das thermische Gewicht einer Shape-Resonanz bei Photoassoziation-Temperaturen recht klein. Durch Anlegen eines nicht-resonanten Lasers an das System wird die Energie des resonanten Zustands in die Nähe der Energien gebracht, bei der Photoassoziation geschehen kann. Somit werden das thermische Gewicht einer Shape-Resonanz verstärkt und die anfängliche Paar-Dichte erhöht. Dieser Effekt wird sowohl auf adiabatischen als auch nicht-adiabatische Zeitskalen in Bezug auf die Rotationsperiode des Systems untersucht. Intensitätsauswirkungen auf die Resonanz-Energie und die Lebensdauer werden vorgestellt.

Abstract

In this work, the coherence properties of the matter is studied in the frame of photoassociation of ultracold alkali atoms by using short and ultrashort laser pulses.

Ultracold can be described with temperatures below 100μK. When energy approaches the ultracold regime, quantum properties of matter becomes visible. In this regime matter such as atoms and molecules show wave properties. Coherent control employs the wave properties of matter to steer a physical process toward a desired target. It can be implemented with coherent radiation such as laser light. In particular, femtosecond laser pulses can be shaped. They thus have become a standard tool for coherent control. Since matter shows its wave properties most clearly at ultralow temperatures, ultracold matter represents the perfect object for coherent control. In the other hand using incoherent fields on ultracold matter does not give us good opportunities to drive quantum properties of it. In this work, it is aimed to bring together ultracold and ultrafast regimes in the frame of photoassociation. Photoassociation, excitation of two colliding atoms by laser light creates very weakly bound molecules.

In the first part of this study, femtosecond photoassociation experiments are simulated. In these experiments and simulations, the broad spectrum of the femtosecond pulses addressing both atomic and molecular transitions is manipulated in a way to prevent the atomic transitions and to promote the molecular transitions. Then the effect of chirp and the effect of additional phase to the pulse are examined. Excited and ground state population are monitored by

carrying out quantum dynamical simulations. The driving ultrafast dipole dynamics are presented.

The photoassociation rate is limited by the low initial atomic pair density at inter-nuclear separations where photoassociation is feasible. In the second part of this study, a new scheme is proposed in order to manage this low pair density by manipulating the shape resonances of the initial atom pair. A shape resonance which is a metastable state occurs when some part of the wavefunction of partial waves with J>0 trapped by a rotational barrier shows a bound structure in the closer internuclear distances where the rest of it shows a scattering wavefunction behavior. Most of the shape resonances in alkaline and alkaline earth metals occur typically at temperatures of a few milli-Kelvin. Therefore, the thermal weight of a shape resonance at photoassociation temperatures is quite small. By applying a non-resonant laser to the system the energy of the resonant state is brought close to the energies those corresponding to the photoassociation temperatures. Thus, the thermal weight of a shape resonance is amplified and initial pair density is enhanced. This effect is studied in both adiabatic and non-adiabatic time scales with respect to the rotational period of the system, intensity effects on the resonance energy and lifetime are presented.

Contents

List of Figures

Chapter 1

Introduction

Light is the principle tool to understand the world around us. The physicist deals with light phenomena by using optics. Light is composed of electromagnetic waves and if there is a well defined phase and frequency relation between them light is coherent. Light emitted from a laser source is coherent radiation. Invention of the laser in 1960s [1] is one of the most remarkable advances of science. It has been used for medical diagnostics and surgical applications, precision measurements, navigation, chemical research and many other areas with direct impact on public life. Coherence properties of laser light set it an effective control tool for physical and chemical processes. In this study it is aimed to applying control schemes to matter by using these coherence properties and explore light-matter interactions.

Atoms and molecules behave as matter waves when they are sufficiently decoupled from the environment. Coherent control employs the wave properties of matter to steer a physical process toward a desired target and needs coherent radiation to be implemented. The field of coherent control has been developed theoretically and experimentally and chemical reactions can be nowadays controlled in the laboratory by controlling the energy distribution among the reactants' different degrees of freedom. Molecular rotation occurs on the 1-100 ps time scale while the vibrational motion of the molecules takes place on the 10 fs-1 ps scale. Coherent control of the molecular system, driving it

[1] Charles H. Townes, Nicolay G. Basov, Aleksandr M. Prokhorov, Nobel Prize in Physics 1964.

from an initial to a final state on these time scales shows us the motion picture of the chemical reaction [2].

Following the advent of ultrafast laser sources and their use to control molecular matter waves, detailed insights into elementary chemical reactions have been recently gained. Developed utilities and coherent control methods have allowed us to understand and control photoinduced chemical reactions such as photoionization, charge transfer, photoisomerization, photo-catalytic processes, photoassociation and even photosynthesis.

Leading edge research in coherent chemistry is now focusing on the application of the developed methods on cold and ultracold systems such as ensembles of ultracold atoms in magneto-optical traps and Bose-Einstein condensates [3]. Since these systems are very well defined quantum objects, exciting features can be extracted from them via tailored laser light manipulation.

In the frame of this Ph.D. work, coherent control of photo-induced reactions by using short (picosecond, nanosecond) and ultrashort (femtosecond) laser pulses in the frame of photoassociation is studied. The core of this work is the application of shaped laser pulses to the photoassociation of ultracold colliding pair of atoms and excitation of them from their initial electronic ground state to the molecular states.

Photoassociation by using ultrashort pulses is proposed more than a decade ago by M. Machholm, A. Giusti-Suzor, and F. H. Mies Machholm *et al.* (1994). Following this proposal several control and enhancement schemes are discussed Dion *et al.* (2001); Koch *et al.* (2006b). In our institute one of the first experimental realization of ultracold molecule photoassociation by shaped femtosecond laser pulses is presented by the experimenter group of Prof. Dr. L. Wöste. The simulations for molecular excitation by performing quantum dynamical calculations of the light-molecule interaction in order to gain detailed insight into the mechanism of femtosecond photoassociation are carried out during this Ph.D. study and presented in Chapter 4 of this thesis. This is done by numerically solving the time-dependent Schrödinger equation for the system of two colliding ultracold atoms and their interaction with the field of

[2] Ahmed Zewail, Nobel Prize in Chemistry 1999.

[3] Eric A. Cornell, Wolfgang Ketterle, Carl E. Wieman, Nobel Prize in Physics 2001.

a shaped femtosecond laser pulse. These results reproduce the experimental data with very good accuracy giving detailed insight into the relevant processes and published in scientific journals Eimer *et al.* (2009); Merli *et al.* (2009); Weise *et al.* (2009).

Gaining experience in coherent control and photoassociation dynamics, a new scheme is proposed in order to increase photoreaction efficiency in Chapter 5 of this thesis. In this scheme the resonance phenomena is exploited. A resonance is distinguished with its high amplitude from the other states and it is related to the rotational motion. By manipulating the separation of atoms in an ensemble, either a naturally existing resonance can be moved towards the desired energies to form molecules or a resonance can be created in these energy scales. A prior laser light, i.e. before the photoassociation pulse, of frequency which does not correspond to molecular transition is used to bring atomic encounters into optimal separation to form molecules.

The interaction of this laser field with an ensemble of atoms induces a dipole moment due to change in the charge distribution and polarization. The induced dipole couples to the field and gives rise to a second order effect on the system. Since the polarizability for the parallel and perpendicular axis are different, polarizability becomes anisotropic. This picture shows a classical analogy with a dumbbell rotating under the influence of the exerted torque on it. The effect of the anisotropic polarizability interaction with the laser field creates coherent superpositions (hybrids) of the rotational states Dooley *et al.* (2003); Lemeshko & Friedrich (2009); Ortigoso *et al.* (1999). In the intermediate and strong field regime, the rotational and vibrational motions are coupled. Control of rotational and vibrational motion is achieved by varying the pulse parameters such as pulse intensity and duration. Initial atomic pair density conntected to the photoassociation efficiency is increased by manipulating the initial distribution of atoms in this way. Thus, two dimensional control of a photo-induced reaction forming diatomic molecules is accomplished.

Chapter 2

Description of Interacting Atoms

The nature of forces effective between two neutral atoms varies by the order of magnitude of the inter-atomic separation R. As the electronic wavefunctions of the two atoms overlap, the two atoms feel a strong interaction with each other due to Coulomb interaction and electron exchange processes. These can lead to the formation of a bound molecule. At large distances where the electrons can no longer move from one atom to the other the phenomena change completely. The probability amplitude decreases with the decreasing overlap of the wavefunctions exponentially as the inter-atomic separation increases. The electrostatic interaction between the electric dipole moments of the two neutral atoms becomes the predominant effect. This gives rise to a total energy which is attractive and which decreases not exponentially but with the inverse powers of (1/R), i.e. $1/\mathrm{R}^6$ for the case of two alkali atoms in their ground states. This is the origin of van der Waals forces. In the case of one alkali atom lies in the excited state (e.g., $2p$) while the other stays in its ground state ($2s$), the energy of the interaction between two varies with $1/\mathrm{R}^3$ due to modified van der Waals forces Cohen-Tannoudji *et al.* (2006). In general, long-range potentials which specify the concerned type of interaction in this thesis are defined by a sum of inverse-power terms Chang (1967); Margenau (1939)

$$V_{LR}(R) = \sum_{i=1}^{N} \frac{C_{m_i}}{R^{m_i}} = \frac{C_{m_1}}{R^{m_1}} + \frac{C_{m_2}}{R^{m_2}} + \frac{C_{m_3}}{R^{m_3}} + \cdots + \frac{C_{m_N}}{R^{m_N}}. \tag{2.1}$$

In Eq. 2.1 V_{LR}, m_i and C_{m_i} stand for the long-range potential, integer powers and dispersion coefficients, respectively. Integer powers and dispersion coefficients are determined by the nature of constituent atoms to which the given state dissociates and the symmetry of the particular molecular state. Explanation of governing rules for which terms contribute to the long-range potentials can be found in several references LeRoy & Bernstein (1970); Meath (1972).

2.1 A Long Range Alkali Dimer Molecule: Single Atom Pair

The alkali atoms have been used in a wide range of atomic, molecular and optical physics research such as thermal collisions, spectroscopy, laser cooling and quantum computation. Therefore the features of their potentials, especially long-range potentials representing the nature of interaction has been investigated by many researchers both experimentally and theoretically Dashevskaya *et al.* (1969); Julienne & Vigué (1991); Marinescu & Dalgarno (1995); Masnou-Seeuws & Pillet (2001b); Movre & Pichler (1977). A purely long-range molecule in which the motion of the two atoms is confined to the region of large distances where only electrostatic interactions are effective provides the concept of *physicists' molecule* Jones *et al.* (2006); Stwalley *et al.* (1978). The physical properties of such a molecule can be related with high precision to the constituent atoms. These purely long-range potentials support bound vibrational levels very close to the dissociation threshold. These bound levels are very shallow compared to the ordinary chemically bound levels. By the emergence of *photoassociation* studies, it has been possible to produce high precision spectra of these vibrational levels.

2.1.1 Motion of a Diatomic Molecule

The different types of motions of a molecule occur on different time scales. As electrons move faster than the nuclei, the nuclei are affected from the averaged potential caused by the spatially spread electronic charge of the electrons. Therefore, the electronic distribution can be studied by considering the nuclei being fixed. This is the Born-Oppenheimer approximation, that leads to separate (but coupled) Schrödinger equations for the electronic and nuclear wavefunctions.

A diatomic molecule can be treated as a rigid rotator in the simplest approximation. Such a system consists of two particles with masses m_1 and m_2 joined by a weightless rod. Rotation axis is considered to be passing through the center of mass and perpendicular to the plane of the masses. The coordinates of each atom and of the molecule as a whole in the laboratory frame can be written in the center of mass frame. In this case the nuclear wavefunction is going to be a product of the wavefunction of the molecule which is represented as a point particle residing at the center of mass and the wavefunction of the relative motion of the atoms. The laboratory coordinates of each atom $r_1 = (x_1, y_1, z_1)$ and $r_2 = (x_2, y_2, z_2)$ are replaced with the center of mass coordinate of the molecule

$$r_{cm} = \frac{m_1 r_1 + m_2 r_2}{m_1 + m_2} = (x_{cm}, y_{cm}, z_{cm}) \tag{2.2}$$

and the internal (relative) coordinate of the atoms with respect to each other

$$r_{rel} = r_1 - r_2 = (x, y, z). \tag{2.3}$$

The total Hamiltonian of the system consists of center of mass motion and internal motion of vibrations and the rotations of the each atom in the molecule

$$\hat{\mathbf{H}} = \hat{\mathbf{H}}_{CM} + \hat{\mathbf{H}}_{int} \tag{2.4}$$

where $\hat{\mathbf{H}}_{CM}$ is the Hamilton operator for the center of mass motion and $\hat{\mathbf{H}}_{int}$ is the Hamilton operator for the internal motion.

The electronic motion, nuclear vibrations and rotations of the molecular frame occur on attosecond, femtosecond and picosecond time scales, respectively. The timescale of the translational motion is of the order of milliseconds in the ultracold regime. Here, one can assume translation of the molecule's center of mass is frozen compared to vibrations and rotations. Thus translational motion does not affect the internal configuration of the system, only relative motion of atoms needs to be taken into account. Schrödinger equation for the internal (relative) motion about the center of mass follows

$$\left[-\frac{\hbar^2}{2\mu}\left(\frac{\partial^2}{\partial x^2}+\frac{\partial^2}{\partial y^2}+\frac{\partial^2}{\partial z^2}\right)+V_i(x,y,z)\right]\varphi_i(x,y,z)=E_{int}\varphi_i(x,y,z) \tag{2.5}$$

where $\mu = \frac{m_1 m_2}{m_1+m_2}$ is the reduced mass of the molecule, V_i is the electronic eigenvalue (potential energy surface) which depends on internuclear separation parametrically and E_{int} is the contribution of the internal motion to the total energy. Here it is assumed that there are no external forces acting on the system.

The motion along the internuclear axis can be separated from the rotational motion of the molecule reduced to one-body by coordinate transformation into spherical polar coordinates $(x, y, z) \rightarrow (R, \theta, \phi)$ with $R = \sqrt{x^2+y^2+z^2}$ due to the symmetry of the system.

The nuclear wavefunction yields to

$$\varphi_n(x,y,z) = \mathfrak{R}_i(R)Y_{JM}(\theta,\phi) \tag{2.6}$$

with $Y_{JM}(\theta,\phi)$ spherical harmonics and $\mathfrak{R}_i(R)$ the radial part of the nuclear wavefunction. Indices n and i in Eq. 2.6 represent all quantum numbers of the nuclear motion and the vibrational quantum number, respectively.

The time independent Schrödinger equation for the vibrational motion is

$$\left[-\frac{\hbar^2}{2\mu}\frac{1}{R}\frac{d^2}{dR^2}R+\frac{\hbar^2 J(J+1)}{2\mu R^2}+V_i(\mathbf{R})\right]\mathfrak{R}_i(\mathbf{R})=E_{int}\mathfrak{R}_i(\mathbf{R}). \tag{2.7}$$

Substitution of $\chi_{ki} = \mathfrak{R}_{ki}(R)R$ leads to

$$\left[-\frac{\hbar^2}{2\mu}\frac{d^2}{dR^2}+\frac{\hbar^2 J(J+1)}{2\mu R^2}+V_i(\mathbf{R})\right]\chi_i(\mathbf{R})=E_{int}\chi_i(\mathbf{R}). \tag{2.8}$$

2.1.2 Rotations of a Diatomic Molecule

If the inter-particle separation is assumed to be fixed during the rotation in such a rigid rotator, the vibrations of two atoms are neglected. The kinetic energy of this rotating molecule is

$$\hat{\mathbf{T}} = \frac{1}{2}m_1\hat{v}_1^2 + \frac{1}{2}m_2\hat{v}_2^2 \tag{2.9}$$

where v_1 and v_2 are the linear velocities of masses m_1 and m_2, respectively. If ω is the angular velocity and since r_1 and r_2 remain unchanged during the rotation kinetic energy can be rewritten as

$$\hat{\mathbf{T}} = \frac{1}{2}\hat{\mathbf{I}}\omega^2 \tag{2.10}$$

with $\hat{\mathbf{I}} = m_1\hat{r}_1^2 + m_2\hat{r}_2^2$ moment of inertia of the system about the rotation axis. This case can be reduced to an equivalent one-body problem by replacing $\hat{r}_1$ and $\hat{r}_2$ into Eq. 2.10 where r_e is the average distance between the two atoms in the molecule. The moment of inertia takes the form of

$$\hat{\mathbf{I}} = \mu\hat{r}_e^2. \tag{2.11}$$

Thus Eq. 2.10 can be written as

$$\hat{\mathbf{T}} = \frac{\hat{\mathbf{J}}^2}{2I} \tag{2.12}$$

where $\hat{\mathbf{J}} = \hat{\mathbf{I}}\omega$ is the angular momentum of rotation and I is the expectation value of $\hat{\mathbf{I}}$. Since vibrations and rotations of atoms are separated, the Schrödinger equation in the spherical coordinates

$$\frac{1}{\mathbf{R}^2}\frac{\partial}{\partial\mathbf{R}}\Big(\mathbf{R}^2\frac{\partial\varphi}{\partial\mathbf{R}}\Big) + \frac{1}{\mathbf{R}^2}\frac{1}{\sin\theta}\frac{\partial}{\partial\theta}\Big(\sin\theta\frac{\partial\varphi}{\partial\theta}\Big) + \frac{1}{\mathbf{R}^2\sin^2\theta}\frac{\partial^2\varphi}{\partial\phi^2} + \frac{2\mu}{\hbar^2}E = 0 \tag{2.13}$$

takes the form

$$\frac{1}{\sin\theta}\frac{\partial}{\partial\theta}\Big(\sin\theta\frac{\partial\varphi}{\partial\theta}\Big) + \frac{1}{\sin^2\theta}\frac{\partial^2\varphi}{\partial\phi^2} = -2I\frac{E}{\hbar^2}. \tag{2.14}$$

By using quantum mechanical description of the square of the angular momentum operator $\hat{\mathbf{J}}^2$

$$\hat{\mathbf{J}}^2 = -\hbar^2\left[\frac{1}{\sin\theta}\frac{\partial}{\partial\theta}\Big(\sin\theta\frac{\partial}{\partial\theta}\Big) + \frac{1}{\sin^2\theta}\frac{\partial^2}{\partial\phi^2}\right] \tag{2.15}$$

Schrödinger equation for the rotational motion is obtained

$$\hat{\mathbf{H}}_{rot}\varphi = \frac{\hat{\mathbf{J}}^2}{2I}\varphi = E_J\varphi \tag{2.16}$$

with the rotational eigenenergies of $E_J = J(J+1)\,\dfrac{\hbar^2}{2I}$.

Separation of variables for the rotational wavefunction leads to $\varphi = \Theta(\theta)\Phi(\phi)$ and the following form of the Schrödinger equation

$$\frac{\hbar^2}{2I}\left[\frac{1}{\sin\theta}\frac{d}{d\theta}\left(\sin\theta\frac{d\Theta}{d\theta}\right) - \frac{M^2\Theta}{\sin^2\theta}\right] + E_J\Theta = 0 \tag{2.17}$$

with

$$\hat{\mathbf{J}}_z^2 = -\hbar^2\frac{\partial^2}{\partial\hat{\phi}^2} \tag{2.18}$$

and

$$\frac{d^2\Phi}{d\hat{\phi}^2} = -M^2\Phi \tag{2.19}$$

if angular momentum component along the quantization axis $\hat{\mathbf{J}}_z$ is chosen to be on the rotation axis. In this case $\hat{\mathbf{J}}_z$ and $\hat{\mathbf{J}}^2$ commute and they have simultaneous eigenfunctions.

The allowed solutions for the eigenfunctions take the form of

$$\Phi_M(\phi) = \frac{1}{\sqrt{2\pi}}e^{iM\phi} \tag{2.20}$$

$$\Theta_{JM}(\theta) = \sqrt{\frac{(2J+1)(J-|M|)!}{2(J+|M|)!}}P_J^{|M|}(\cos\theta) \tag{2.21}$$

where $P_J^{|M|}$ is the associated Legendre polynomials.

2.2 Ensemble of Atoms

Density operator description can be a useful tool in the cases where many atoms are involved. Energy contributions coming from different degrees of freedom are stored in the system regarding the partition functions.

Partition function is defined as

$$Z(T,V,N) = \sum_i \exp(-\beta E_i) \tag{2.22}$$

with $\beta = 1/k_B T$. The terms T, V, N and E_i represent temperature, volume, number of particles and the eigenenergy of the ith state, respectively.

Energy contributions come from translational, rotational, vibrational motion and electronic excitation in a two atom picture. Under assumption of separable degrees of freedom, the partition function can be factorized into independent components

$$\begin{aligned} Z(T,V,N) &= \sum_{allstates} \exp\Big(\beta(\varepsilon_{trans} + \varepsilon_{rot} + \varepsilon_{vib} + \varepsilon_{elec})\Big) && (2.23)\\ &= Z_{trans} + Z_{rot} + Z_{vib} + Z_{elec} && (2.24) \end{aligned}$$

as Z_{trans}, Z_{rot}, Z_{vib} and Z_{elec} being the contributions of translational, rotational, vibrational motions and electronic excitation to the partition function with the corresponding energy contributions ε_{trans}, ε_{rot}, ε_{vib} and ε_{elec}.

The density operator for an ensemble of atoms at their thermal equilibrium before any interaction is

$$\hat{\rho}(\mathbf{t_0}) = \frac{1}{Z}\exp(-\beta\hat{\mathbf{H}}). \tag{2.25}$$

2.3 Light Matter Interaction: Atoms and Molecules Interacting with Laser

Application of an external field distorts or polarizes atoms or molecules. Quantum mechanically their distorted wavefunctions can be represented in terms of the linear combination of eigenfunctions. If the frequency of the field matches a transition frequency of the atom or the molecule, mixing of wavefunctions between initial(ground) and final(excited) states can be observed. This process is a time-dependent process, as the field is a time dependent field Atkins & Friedman (2010); Cohen-Tannoudji *et al.* (2006).

Hamiltonian for a molecular system in interaction with laser light can be written as

$$\hat{\mathbf{H}} = \hat{\mathbf{H}}_0 + \hat{\mathbf{H}}_{int} \tag{2.26}$$

where $\hat{\mathbf{H}}_0$ is the Hamiltonian of the field-free system, $\hat{\mathbf{H}}_{int}$ is the part of the Hamiltonian describing the light-matter interaction.

By using multipole expansion and calculating the interaction with the electric field of the laser light, interaction energy of the field with the matter W can be written in the following form:

$$W = V_0 \int \rho(r)dr + \Big[\frac{\partial V}{\partial r}\Big]_0 \rho(r) r dr + \frac{1}{2!}\Big[\frac{\partial^2 V}{\partial r^2}\Big]_0 \rho(r) r^2 dr + ... \tag{2.27}$$

In the expansion $\rho(r)$ is the charge density, V is the potential, the first term is monopole, second term is dipole and third term is quadrupole terms, respectively. $\Big[\frac{\partial V}{\partial r}\Big]_0 = E(r,t)$ is the electric field at the origin.

Electric field can be written as an oscillating plane wave

$$\mathbf{E}(r,t) = \hat{\mathbf{e}}\frac{E_0(t)}{2}(e^{i(\mathbf{k}\cdot\mathbf{r}+\omega t)} + e^{-i(\mathbf{k}\cdot\mathbf{r}+\omega t)}) \tag{2.28}$$

where $\hat{e}$ is the unit vector.

Taylor's series expansion of $e^{i(\mathbf{k}.\mathbf{r})}$ leads to

$$e^{\pm i(\mathbf{k}.\mathbf{r})} = 1 \pm i\mathbf{k}(\mathbf{r}-\mathbf{r}_0) \mp \frac{1}{2}(\mathbf{k}\cdot\mathbf{r})^2 \pm ... \tag{2.29}$$

The typical wavelengths corresponding to electronic transitions in diatomic molecules are large as compared to the molecule size. If the $kr = \frac{2\pi r}{\lambda} \ll 1$ *dipole approximation* can be done and $e^{\pm i(\mathbf{k}.\mathbf{r})}$ term can be replaced by 1. Thus electric field of the light is assumed to be only time dependent.

Interaction Hamiltonian can be replaced by the dipole term

$$\hat{\mathbf{H}}(t) = \hat{\mathbf{H}}_0 - \hat{\mu}\cdot\mathbf{E}(t) \tag{2.30}$$

where $\hat{\mu}$ is the dipole moment operator.

$$\hat{\mu} = \sum_i (-e)\hat{r}_i + \sum_n Z_n e \hat{\mathbf{R}}_n \tag{2.31}$$

$$= \hat{\mu}_{el} + \hat{\mu}_{nuc}. \tag{2.32}$$

For a general system of electrons and nuclei, the dipole moment operator is defined as the sum of dipole moment operators for electrons $\hat{\mu}_{el}$ and nuclei $\hat{\mu}_{nuc}$. Each component involves the particle charge multiplied by the position vector.

2.3.1 Atomic to Molecular State Transitions via Dipole Interaction

When an atom pair absorbs radiation, light changes the electron motion and the atom pair can undergo electronic transitions. As the time scale of the nuclear motion is very long compared to the time scale of the electronic motion, the motion of the nuclear frame can be assumed frozen. In this case a vertical vibronic transition occurs between the vibrational levels of the ground and excited state potentials that resemble each other most. Thus Franck-Condon principle is preserved by keeping the dynamical state of the nuclei least varied Atkins & Friedman (2010).

This vibronic transition is governed by the transition dipole operator $\hat{\mu}$. In the frame of the Born-Oppenheimer approximation, the transition dipole moment can be calculated by taking the following integrals

$$\begin{aligned} < \varepsilon_f \upsilon_f |\hat{\mu}| \varepsilon_i \upsilon_i > = & \int \psi^*_{\varepsilon_f}(\mathbf{r};\mathbf{R})\psi^*_{\upsilon_f}(\mathbf{R})(\hat{\mu}_{el}+\hat{\mu}_{nuc})\psi_{\varepsilon_i}(\mathbf{r};\mathbf{R})\psi_{\upsilon_i}(\mathbf{R})dV_{el}dV_{nuc} \\ = & \int \psi^*_{\upsilon_f}(\mathbf{R})\Big(\int \psi_{\varepsilon^*_f}(\mathbf{r};\mathbf{R})\hat{\mu}_{el}\psi_{\varepsilon_i}(\mathbf{r};\mathbf{R})dV_{el}\Big)\psi_{\upsilon_i}(\mathbf{R})dV_{nuc} \\ + & \int \psi^*_{\upsilon_f}(\mathbf{R})\hat{\mu}_{nuc}\Big(\int \psi_{\varepsilon^*_f}(\mathbf{r};\mathbf{R})\psi_{\varepsilon_i}(\mathbf{r};\mathbf{R})dV_{el}\Big)\psi_{\upsilon_i}(\mathbf{R})dV_{nuc} \end{aligned} \tag{2.33}$$

where $|\varepsilon_{i(f)}\upsilon_{i(f)}>$ is the initial (final) vibronic state with the associated wavefunctions $\psi_\varepsilon(\mathbf{r};\mathbf{R})\psi_\upsilon(\mathbf{R})$. Here $\mathbf{r}$ and $\mathbf{R}$ represent the electronic and nuclear coordinates, respectively. Operator $\hat{\mu}_{el}$ governs the electronic and operator $\hat{\mu}_{nuc}$ governs the nuclear part of the dipole transition.

Since the electronic potential surfaces are orthogonal to each other, the integral over the electronic coordinates vanishes in the last term. By assuming the position of the nuclei does not change significantly, the $\hat{\mu}_{el}$ can be assumed as a constant value. The electric dipole transition moment follows

$$< \varepsilon_f \upsilon_f | \hat{\mu} | \varepsilon_i \upsilon_i > \quad = \quad d_{el}^{fi} \int \psi_{\upsilon_f}^{*}(\mathbf{R}) \psi_{\upsilon_i}(\mathbf{R}) dV_{nuc}. \tag{2.34}$$

The square of the integral in 2.34 is the so-called Franck-Condon factor for this transition. The dipole transition moment describes the strength of the interaction that causes the transition in which the state changes from i to f.

2.3.2 Response of the System to the Applied Optical Field

A dipole interaction model for atoms was first proposed by Silberstein Silberstein (1917) and further developed for molecules in aggregates by DeVoe DeVoe (1965). The operator for the induced dipole moment of atom i in a N-atom system can be written as Applequist *et al.* (1972)

$$\hat{\mu}_i \quad = \quad \alpha_i \Big[\mathbf{E}_i - \sum_{j \neq i}^{N} \mathbf{T}_{ij} \hat{\mu}_j \Big] \tag{2.35}$$

where α_i is the polarizability tensor of unit i, $\mathbf{E}$ is the electric field vector of the applied optical field, and $\mathbf{T}$ is the dipole field tensor whose form can be found in several literature Applequist *et al.* (1972); Böttcher (1973).

The induced dipole moment operator for the molecule $\hat{\mu}_{mol}$ can be written as a sum of dipole moment operators of N atomic entities under the influence of a uniform electric field $\mathbf{E}$

$$\hat{\mu}_{mol} \quad = \quad \sum_{i=1}^{N} \hat{\mu}_i = \Big[\sum_{i=1}^{N} \sum_{j=1}^{N} \mathbf{B}_{ij} \Big] \mathbf{E} \tag{2.36}$$

where $\mathbf{B}$ is the tensor relating the interaction of units i and j with the electric field Applequist *et al.* (1972).

The interaction between the field and the dipole is driven by the molecular polarizability tensor α_{mol}

$$\alpha_{mol} = \Big[\sum_{i=1}^{N}\sum_{j=1}^{N}\mathbf{B}_{ij}\Big]. \tag{2.37}$$

In the case of a diatomic molecule AB with isotropic polarizabilities α_A and α_B, the diagonal form of the α_{mol} has two independent components. These are $\alpha_{\parallel}$ parallel and $\alpha_{\perp}$ perpendicular components to the internuclear axis and they have the following form Applequist *et al.* (1972); Silberstein (1917)

$$\alpha_{\parallel} = \frac{\alpha_A + \alpha_B + 4\alpha_A\alpha_B/r^3}{1 - 4\alpha_A\alpha_B/r^6} \tag{2.38}$$

$$\alpha_{\perp} = \frac{\alpha_A + \alpha_B - 2\alpha_A\alpha_B/r^3}{1 - \alpha_A\alpha_B/r^6} \tag{2.39}$$

Equations 2.38 and 2.39 indicates the anisotropy of the molecule even though the atoms are isotropic. Another related quantity for this dipole interaction model is the polarizability anisotropy $\Delta\alpha$ and it is determined by the difference of the parallel and perpendicular components of the polarizability tensor

$$\mathbf{\Delta}\alpha = \alpha_{\parallel} - \alpha_{\perp}. \tag{2.40}$$

The interaction Hamiltonian for the considered molecule - field interaction has the following form

$$\hat{\mathbf{H}}_{int} = \frac{J^2}{2\mu\mathbf{R}^2} - \mu E\cos\theta - \frac{1}{2}(\Delta\alpha\cos^2\theta + \alpha_{\perp})E^2 \tag{2.41}$$

where J is the rotational quantum number, θ is the angle between the field and the dipole moment. The term $dE\cos\theta$ in the 2.41 has a non-zero contribution only if the molecule has a permanent dipole moment. Here it is assumed that the field is far from any resonance with all dipole transitions of the molecule.

Chapter 3

Numerical Methods

Numerical analysis of quantum molecular dynamics of a system requires discretized representation of the wavefunctions and operators acting on the system. Grid representation of the operators using fast Fourier transforms has been established to be very robust and effective tool to solve the Schrödinger equation for vibrational states of molecules Balint-Kurti *et al.* (1992); Kosloff (1988); Wyatt & Zhang (1996). Therefore this method is chosen for the numerical simulations in the frame of this work. Operators in the Hamiltonian for potential and kinetic energy are represented on grids in the coordinate space and in the momentum space, respectively. The wavefunction of a quantum state in coordinate space and that in momentum space is related via Fourier transform. By using this transformation desired quantities of interest resulted from operation of the Hamiltonian on the wavefunctions in different spaces are obtained.

3.1 Representation of Wavefunctions and Hamiltonian on a Fourier Grid

Representation of the wavefunction in different spaces at initial time are related via Fourier transformation as

$$\psi(r,t) = \frac{1}{\sqrt{2\pi}} \int_{-\infty}^{\infty} \exp(ikr)\psi(k,t)dk \tag{3.1}$$

in the coordinate space and

$$\psi(k,t) = \frac{1}{\sqrt{2\pi}} \int_{-\infty}^{\infty} \exp(-ikr)\psi(r,t)dr \tag{3.2}$$

in the momentum space.

Action of the Hamiltonian in the coordinate space at initial time can be written as

$$\begin{aligned} < r|\hat{\mathbf{H}}|\psi(t=0) > &= < r|\mathbf{V}(\hat{\mathbf{r}}) + \hat{\mathbf{T}}|\psi(t=0) > \\ &= < r|\mathbf{V}(\hat{\mathbf{r}})|\psi(t=0) > + < r|\hat{\mathbf{T}}|\psi(t=0) > . \end{aligned} \tag{3.3}$$

The operation of $\mathbf{V}(\hat{\mathbf{r}})$ on the wavefunction is *local* and this action simply involves multiplication of the potential and wavefunction values at each defined coordinate point r_i. The operation of the kinetic energy operator $\hat{\mathbf{T}}$ is rather complicated. This operation is *non-local* in the coordinate space and it requires representation of the wavefunction in the momentum space given in Eq. 3.2. Action of the kinetic energy on the wavefunction then involves the inverse Fourier transformation as

$$< r|\hat{\mathbf{T}}|\psi(t=0) >= \frac{\hbar^2}{2m} \frac{1}{\sqrt{2\pi}} \int_{-\infty}^{\infty} k^2 \exp(ikr)\psi(k,(t=0))dk. \tag{3.4}$$

Finally, the resulting matrix element from the action of the Hamiltonian on a state follows

$$< r|\hat{\mathbf{H}}|r' >= \frac{1}{2\pi} \int_{-\infty}^{\infty} \exp(ik(r-r'))Tdk + V(r)\delta(r-r'). \tag{3.5}$$

Equally spaced sampling points both in spatial and momentum space allows to represent a certain number of N_g quantum states. The wavefunction

of the quantum states can be represented within (r,k) grid. In a uniform grid continuous coordinate values r are replaced by a grid of N discrete values r_n. Any grid point r_n will be assigned to

$$r_n = n\Delta r \tag{3.6}$$

with a Δr grid step.

λ_{max} the longest represented wavelength is covered by $L = N\Delta r$ the length of the grid. This determines the smallest represented frequency in the momentum space. The spacing in the momentum space follows

$$\Delta k = \frac{2\pi}{\lambda_{max}}. \tag{3.7}$$

The wavefunction at any desired coordinate value is obtained by interpolation between the grid points, r_n, using the so-called pseudospectral representation:

$$\psi(r_n) \equiv \bar{\psi}(r_n) = \sum_{j=0}^{N-1} a_j g_j(r_n). \tag{3.8}$$

By using a set of analytical basis functions, $g_j(r)$, the relation between the grid points, r_n, and the expansion coefficients, a_j, is established. The orthogonal functions can be chosen as basis functions for Eq. 3.8 fulfilling the orthogonality relation Fattal *et al.* (1996); Wyatt & Zhang (1996)

$$\sum_{n=0}^{N-1} g_j(r_n) g_m(r_n) = \delta_{jm}. \tag{3.9}$$

Fourier grid representation is a special case of orthogonal collocation methods Gottlieb & Orszag (2009) which uses Fourier expansion of the wavefunction. Expansion functions $g_j(r)$ are chosen to be

$$g_j(r) = e^{i2\pi jr/L}, \quad j = -N/2, \ldots, 0, \ldots, N/2 - 1. \tag{3.10}$$

The relation between a_j expansion coefficients and $\psi(r_n)$ wavefunction in the Fourier grid representation corresponds to the following phase space relation

$$a_j = \frac{1}{N} \sum_{n=1}^{N} \psi(r_n) e^{-i2\pi jn/N} \tag{3.11}$$

which reflects the natural relation between coordinate and momentum spaces. Application of fast Fourier transformation (FFT) algorithms scales the total number of operations as $O(N \log(N))$ Cooley & Tukey (1965).

3.1.1 Adaptive Grid

Diagonalization of the Hamiltonian in equidistantly discretized grid numerically scales as $O(N^3)$ Kosloff (1988). If very large De Broglie wavelength (i.e., low temperatures) of atoms should be represented with good accuracy very large grids are desired. In such cases equally spaced spatial grid representation becomes computationally expensive since the number of grid points becomes also very large. In the other hand, if very large collision momentum values should be considered, very dense grids are required in order to resolve the quick oscillatios in spatial coordinate space. For cold or ultracold systems, initially the momenta is not very large. However, when several thousands cm^{-1} deep realistic interatomic potentials are considered, good representation of the vibrational wavefunctions requires to account for this quick oscillations, i.e. a dense grid at short inter-nuclear separation is needed.

The grid representation of the system is optimized by using an adaptive grid with variable grid spacing instead of using a constant one Fattal *et al.* (1996). In order to represent the local kinetic energy correctly a variable grid spacing given by

$$s(r) = \frac{\pi}{\sqrt{2\mu[E_{add} - V(r)]}} \tag{3.12}$$

is used Kokoouline *et al.* (1999).

In this representation, the coordinate grid possesses more sampling points at short internuclear distances where the potential energy curve is steep and less sampling points where the potential energy curve is flat. Being slightly larger than maximum potential energy value V_{max} the maximum asymptotic representable kinetic energy on the grid Kallush & Kosloff (2006). The grid step goes to infinity as $V(R) \rightarrow 0$ and E_{add} is a cutoff energy that ensures a finite grid step.

The mapped grid is set up by defining a transformation function $\beta(r)$ to relate the physical grid and a working grid with a constant grid spacing Δx as

$$\beta(r) = \int_{R_{min}}^{R_{guess\ 1}} \frac{\Delta x \sqrt{2\mu[E_{add} - V(r)]}}{\pi} dr. \tag{3.13}$$

Integration domain spans the coordinate space between R_{min} the initial grid coordinate and the guess coordinate $R_{guess\ 1}$. Local phase space volumes are calculated by carrying on the integration from $R_{guess\ 1}$ to several guess coordinates until the end of the physical grid $R_{guess\ N} = R_{max}$. Integration of Eq. 3.13 leads to $\beta \leq 1$. Smaller values of β distribute more points into the sampled coordinate space while maximum value of $\beta = 1$ corresponds to the minimum classical (WKB) estimation of the represented phase space.

In this representation $\mathbf{V}(\hat{\mathbf{r}})$ potential energy operator stays local. However, in order to represent $\hat{\mathbf{T}}$ the non-local kinetic energy operator, the change of variables from the mapped grid to the physical grid should be calculated. This is done by representing the kinetic energy operator as

$$\hat{\mathbf{T}} = -\frac{\pi^2}{2mL_x^2} \hat{\mathbf{J}}^{-1/2} \hat{\mathbf{D}} \hat{\mathbf{J}}^{-1} \hat{\mathbf{D}} \hat{\mathbf{J}}^{-1/2} \tag{3.14}$$

where $L_x = R_{max} - R_{min}$ is the grid interval, $\hat{\mathbf{J}}$ is the first order Jacobian related to the β parameter as

$$\hat{\mathbf{J}}(R_{guess\ i}) = \frac{dr}{dx}|_{r=R_{guess\ i}} = \beta'|_{r=R_{guess\ i}} = \sqrt{\frac{2\mu}{\pi^2}[E_{add} - V(R_{guess\ i})]} \tag{3.15}$$

and $\hat{\mathbf{D}}$ is the first derivative operator given by

$$\hat{\mathbf{D}}_{i,j} = \left(\frac{d}{dx}\right)_{i,j} = \begin{cases} 0 & i = j \\ \frac{(-1)^{i-j}}{\sin[(i-j)\pi/N]} & i \neq j. \end{cases} \tag{3.16}$$

The unphysical (*ghost*) states may arise if an innsufficient number of sampling points is used in this case. Furthermore, possible accuracy problems may be encountered if the calculation of the derivatives of the Jacobian is desired. In order to prevent this, a mapped sine basis set is employed Borisov (2001); Lemoine (2000); Willner *et al.* (2004).

3.2 Chebyshev Propagator for Time-dependent Quantum Dynamical Simulations

The wavepacket propagation is achieved by employing a Chebyshev propagator. Time dependent non-relativistic Schödinger equation

$$i\hbar\frac{\partial\psi(t)}{\partial t} = \hat{\mathbf{H}}\psi(t) \tag{3.17}$$

has the formal solution given in Eq. 3.18 Leforestier *et al.* (1991); Tal-Ezer *et al.* (1992) since $\hat{\mathbf{H}}$ has an explicit time dependence

$$\psi(t) = \hat{\mathbf{U}}(t)\psi(0) = \hat{\mathbb{T}}\exp\left[-\frac{i}{\hbar}\int_0^t \hat{\mathbf{H}}(t')dt'\right]\psi(0) \tag{3.18}$$

where $\hat{\mathbb{T}}$ is the time ordering operator and $\hat{\mathbf{U}}$ is the propagator.

For suffeciently small time steps Δt, one can always assume that between time t and $t + \Delta t$, $\hat{\mathbf{H}}(t)$ is constant thus time ordering is neglected Kosloff (1988, 1994); Tal-Ezer *et al.* (1992); Tannor (2007). Polynomial expansion of the propagator $\hat{\mathbf{U}}(t)$ is done by employing Φ_n the Chebyshev polynomials in order to build a global propagator scheme

$$\hat{\mathbf{U}}(t) = \exp -\frac{i}{\hbar}\hat{\mathbf{H}}t \approx \sum_0^{N_t} a_n\Phi_n\left(-\frac{i}{\hbar}\hat{\mathbf{H}}t\right). \tag{3.19}$$

Re-normalized eigenvalues of the Hamiltonian in the range of [-1, 1] are obtained by shifting the re-normalized Hamiltonian as

$$\hat{\mathbf{H}}_{norm} = 2\frac{\hat{\mathbf{H}} - \hat{\mathbf{I}}(\Delta E/2 + E_{min})}{\Delta E}. \tag{3.20}$$

Since the complex Chebyshev polynomials are defined in the range of $[-i, i]$, Hamiltonian operator is normalized in the spectral range $\Delta E = E_{max} - E_{min}$ in Eq. 3.20. By application of the propagator in Eq. 3.19 with this Hamiltonian, the wavefunction at time t can be approximated as

$$\psi(t) \approx \exp[-\frac{i}{\hbar}(\frac{\Delta E}{2} + E_{min})t] \sum_{0}^{N_t} a_n \left(\frac{\Delta E.t}{2\hbar}\right) \Phi_n(-i\hat{\mathbf{H}}_{norm})\psi(0) \tag{3.21}$$

where $a_n(\alpha)$ expansion coefficients has the following form

$$a_n(\alpha) = \int_{-i}^{i} \frac{e^{i\alpha x}\Phi_n(x)dx}{\sqrt{1-x^2}} = 2J_n(\alpha) \tag{3.22}$$

with $J_n(\alpha)$ Bessel functions and α argument is $\alpha = \frac{\Delta E.t}{2\hbar}$.

Propagation for each time t is realized by operating $\Phi_n(-i\hat{\mathbf{H}}_{norm})$ on the the wavefunction $\psi(0)$ as $\psi_n = \Phi_n(-i\hat{\mathbf{H}}_{norm})\psi(0)$ and the following recursion relation of the Chebyshev polynomials is employed

$$\begin{aligned} &\Phi_0 = \psi(0) \\ &\Phi_1 = -i\hat{\mathbf{H}}_{norm}\psi(0) \\ &\vdots \\ &\Phi_{n+1} = -2i\hat{\mathbf{H}}_{norm}\Phi_n + \Phi_{n-1}. \end{aligned} \tag{3.23}$$

The calculation is truncated when the desired accuracy is obtained.

3.3 Boltzmann Averaging on a Finite Grid

In this study the Hamiltonian of the physical system is represented on a finite coordinate grid and the expectation values of the operators are calculated by using this representation as explained in the previous sections of this chapter. Since the photoassociation of ultracold atoms is the subject of interest, calculation of number of created molecules is necessary. In this section the relation between the physical volume of the considered ultracold atomic ensemble and the coordinate space representation on a finite grid is explained. The system is described in terms of a canonical ensemble.

The probability density operator for a canonical ensemble of N atoms in thermal equilibrium at temperature T can be written as Landau & Lifshitz (1980)

$$\hat{\rho}_{T,N} = \frac{1}{Z_{eq}} e^{-\hat{\mathbf{H}}_N/k_B T} \tag{3.24}$$

where $Z_{eq} = \mathbf{Tr}[e^{-\hat{\mathbf{H}}_N/k_B T}]$ is the partition function and k_B is the Boltzmann constant.

The ultracold ensemble of atoms in a magneto-optical trap (MOT) is considered as a very dilute gas where $\hat{\mathbf{H}}_N$ the Hamiltonian of the system consists only in operators for single particles and two-body interaction of atoms.

The number of created excited state molecules is estimated by employing the $\hat{\mathbf{P}}_{exc}$ projection operator for the excited (final) state and $\hat{\rho}(t_f)_{T,N}$ the density operator for the ground (initial) state at the end of the time evolution in the following way Koch *et al.* (2006a); Machholm *et al.* (1994)

$$\begin{aligned} < \hat{\mathbf{P}}_{exc} >_T &= \mathbf{Tr}[\hat{\mathbf{P}}_{exc}\hat{\rho}(t_f)_{T,N}] \\ &= \mathbf{Tr}[\hat{\mathbf{P}}_{exc}\hat{\mathbf{U}}(t_0,t_f)\hat{\rho}(t_0)_{T,N}\hat{\mathbf{U}}^{\dagger}(t_0,t_f)]. \end{aligned} \tag{3.25}$$

The unitary time evolution operator $\hat{\mathbf{U}}(t_0,t_f)$ includes laser-atomic ensemble interaction and acts on $\hat{\rho}(t_0)_{T,N}$ the initial distribution of atoms on the ground state given by Eq. 3.24. In order to write the ensemble average of the physical observable $< \hat{\mathbf{P}}_{exc} >_T$, the eigenfunctions of a particle in a box, φ_{nJM} are chosen as the basis set where n, J, M stand for translational, angular momentum and magnetic quantum numbers, respectively. In the system of interest, center of mass motion is decoupled from the inter-nuclear degrees of freedom under the assumptions explained in subsection 2.1.1 of this study which is valid for systems of homogeneous ensembles and ensembles in a harmonic trap. Thus, Eq. 3.25 can be calculated only within the internal degrees of freedom.

The density matrix of the initial state is constructed in terms of $\varphi_{nJ}(R,\theta)$ the ro-vibrational eigenfunctions of the pair Hamiltonian, $\hat{\mathbf{H}}_2$, with eigenvalues E_{nJ}, Ağanoğlu *et al.* (2011). The ro-vibrational Hamiltonian of the system

is represented on a finite-size grid of variables $(R;\theta,\phi)$ for inter-nuclear separation and angular coordinates. The azimuthal symmetry about the laser polarization axis is used and therefore the light-matter interaction depends only on the polar angle θ Koch *et al.* (2006a)

$$\rho_{T,2}(R,\theta) = \frac{1}{4\pi R^2}\frac{\sum_{nJ}(2J+1)e^{-E_{nJ}/k_BT}|\varphi_{nJ}(R,\theta)|^2}{\sum_{nJ}(2J+1)e^{-E_{nJ}/k_BT}}\,. \tag{3.26}$$

The expectation value of the projection operator for a pair of atoms follows

$$< \hat{\mathbf{P}}_{exc,2} >_T = \frac{1}{4\pi Z_{eq}}\sum_{n,J}(2J+1)e^{\frac{-E_{nJ}}{k_BT}} < \varphi_{nJ}|\hat{\mathbf{U}}(t_0,t_f)\hat{\mathbf{P}}_{exc}\hat{\mathbf{U}}^{\dagger}(t_0,t_f)|\varphi_{nJ} > \tag{3.27}$$

with $Z_{eq} = \sum_{n,J} < \varphi_{nJ}(R,\theta)|e^{-\hat{\mathbf{H}}/k_BT}|\varphi_{nJ}(R,\theta) >$ the partition function. Here, $< \hat{\mathbf{P}}_{exc} >_T$ is reduced to $< \hat{\mathbf{P}}_{exc,2} >_T$ by considering the condtions of a dilute gas where the unit volume can be chosen to cover only two atoms.

The representation of the physical volume V on a finite grid is related to the number of particles N as

$$P_1 = N\,\frac{v}{V} \tag{3.28}$$

where v is the volume of the *box*. Corresponding probability of finding two atoms in this small *box* is

$$P_2 = N\,\frac{v}{V}\;\;(N-1)\frac{v}{V} \approx P_1^2. \tag{3.29}$$

The total number of excited state molecules is obtained by using the probability of finding 2 atoms in the defined box given in Eq. 3.29 and the expectation value of the projection operator for excited state as

$$\begin{aligned} N_{mol,exc} &= \frac{1}{2}N^2\frac{v}{V} < \hat{\mathbf{P}}_{exc,2} >_T \\ &= \frac{V}{v}P_1^2 < \hat{\mathbf{P}}_{exc,2} >_T\,. \end{aligned} \tag{3.30}$$

3.4 Representation of Two Dimensional Hamiltonian

When a strong laser field is exerted on the atom pairs, vibrational and rotational motions are coupled. The contribution of the field to the energy of the

system becomes comparable to the vibrational or rotational spacing. In such energy scales inevitable hybridization of the rotational and vibrational states makes the use of a two dimensional Hamiltonian represented in both spatial and angular degree of freedom desirable. The Hamiltonian for the rovibrational motion of a diatomic molecule in the presence of strong off-resonant laser can be written as González-Férez & Schmelcher (2005a)

$$\hat{\mathbf{H}} = -\frac{\hbar^2}{2R^2\mu}\frac{\partial}{\partial R}(R^2\frac{\partial}{\partial R}) + \frac{\hat{\mathbf{J}}^2(\theta,\phi)}{2\mu R^2} + V_g(R) - \frac{2\pi I}{c}[\Delta\alpha(R)\cos^2\theta + \alpha_\perp(R)] \tag{3.31}$$

where R and θ,φ are inter-nuclear separation and spherical coordinates, μ is the reduced mass, $V_g(R)$ is the field-free electronic potential energy surface and $\hat{\mathbf{J}}(\theta,\phi)$ is the orbital angular momentum, respectively. In the last term, I represents the laser intensity, $\Delta\alpha$ and $\alpha_\perp$ stand for the polarizability anisotropy and the perpendicular component of the polarizability. In the cases where $\hat{\mathbf{J}}_z$ is a constant of motion, the wavefunction of the system Ψ can be written as $\Psi(R,\theta,\phi) = \Psi_M(R,\theta)e^{iM\phi}$ with M the magnetic quantum number. Moreover, the direction of the applied laser field sets the symmetry of the system and azimuthal symmetry with respect to the laser polarization direction leaves the interaction θ dependent only by averaging out the ϕ dependence. Thus, the magnetic quantum number M stays unchanged.

In order to solve the eigenvalue problem of this system a hybrid computational approach is employed. A basis set expansion in terms of Legendre functions for the angular coordinate is used in combination with Fourier grid representation for the radial coordinate. Further details can be found in references Fleischer *et al.* (2009); González-Férez & Schmelcher (2005a,b).

Chapter 4

Coherent Control of Photoassociation

Two colliding free atoms can absorb a photon and form a bound excited state molecule. This process is named photoassociation. Formation of diatomic molecules by means of photoassociation is first described by Thorsheim, Julienne and Weiner Thorsheim *et al.* (1987) and explained in the frame of scattering resonance formalism. Following this study, several groups Dion *et al.* (2001); Fioretti *et al.* (1998); Gabbanini *et al.* (2000); Lett *et al.* (1993); Miller *et al.* (1993); Nikolov *et al.* (1999, 2000) achieved creation of translationally cold molecules via photoassociation.

At cold and ultracold regime wave nature of the reactants becomes visible and replaces the counterintuition of chemical reactions could occur at ultracold temperatures Ospelkaus *et al.* (2010). Reducing the temperature increases the de Broglie wavelength of the particles to a scale up to 1 μm which is larger than the characteristic molecular dimensions Burnett *et al.* (2002). In this scheme, long-range interactions become important in order to understand and control the reaction dynamics Julienne (2009). At such low temperatures, photoassociation occurs at large inter-nuclear separations.

Ultracold chemical reactions are limited by the available collision channels. Statistical distribution of thermal collision energies becomes very sharp, about few hundred μK wide. Depending on the isotope of interest, only s-wave, p-wave free states dominates the photoreaction in this narrow energy spread,

unless tunneling occurs Stwalley *et al.* (2009). Therefore understanding and controlling the reactions at this temperature regime through external fields, quantum statistics and threshold laws is relatively easier.

Ultracold molecules allow to test motional effects more precisely on fundamental constants, parity and symmetry violation and some other fundamental laws of nature due to their internal structure Flambaum & Kozlov (2007). Many-body systems can be modelled with ultracold molecules by tuning the inter-particle interactions Büchler *et al.* (2007); Carr *et al.* (2009); Micheli *et al.* (2006). The resonance-mediated reactions is also another application area of coherently controlled ultracold molecular physics Ağanoğlu *et al.* (2011); Chakraborty *et al.* (2011).

Photoassociation provides a testing ground for the mentioned physical concepts and applications. In this chapter, firstly the basic concepts of photoassociation are summarized and secondly the results of the femtosecond photoassociation of ultracold rubidium atoms to molecules are presented.

4.1 Basic Concepts of Photoassociation

Coupling of free atoms into a bound excited state depends on the structure of both ground and excited state potentials and the shape of the initial and final wavefunctions. Atomic to molecular transition probabilities in photoassociation can be described by a Frank-Condon factor between the ground and excited state radial wavefunctions for low laser energies. This transition is resonant at Condon point R_C where excited and ground state potential energy difference matches the photon energy Burnett *et al.* (2002); Jones *et al.* (2006)

$$A + A + \hbar\omega_1 \rightarrow A_2^*(v', J'). \tag{4.1}$$

In Eq. 4.1, A refers to the reactant isotope, ω_n stands for the frequency of the radiation, v and J indicate the vibrational and rotational quantum numbers, respectively. There are further possible processes for this excited state molecule. It can either decay radiatively to a bound level of the electronic ground state potential surface

$$A_2^*(v', J') \rightarrow A_2^*(v'', J'') + \hbar\omega_2 \tag{4.2}$$

or into continuum

$$A_2^*(v', J') \rightarrow A + A + \hbar\omega_3. \tag{4.3}$$

Since photoassociation more probably occurs in a narrow band around asymptote of the electronic excited state potential energy surface, the latter case is more likely to occur. The free-bound Franck-Condon factors are large only for weakly bound excited state levels close to the asymptote.

4.1.1 Model for Transitions

The interaction of the ultracold ground state atoms with the laser light can be understood in terms of vertical transitions as mentioned in section 2.3 of this thesis. The outcome of the laser-matter interaction is predetermined by the energy (frequency) shift of the laser light relative to the atomic resonances. In spectroscopy this shift is commonly called *detuning*. If the detuning is positive (blue) with respect to the resonance, atoms can be excited to a repulsive molecular state. This free to free transition process leads to creation of excited atoms. Atoms gain energy depending on the amount of (blue) detuning Δ_{blue} and their kinetic energy will be $E_e = E_g + \hbar\Delta_{blue}$ Almazor *et al.* (2001); Julienne (1996). Ground state atoms can be excited to a bound vibrational level of the attractive excited molecular state if the laser light is negative (red) detuned close the resonance. This process would be a free to bound transition. The transition occurs when the difference of excited and ground potential energy surfaces at the Condon point R_C matches the photon energy $\hbar\omega$

$$V_{exc}(R_C) - V_{gr}(R_C) = \hbar\omega \tag{4.4}$$

where V_{exc} and V_{gr} stand for the excited state and the ground state potential energy surfaces, respectively. Two possible transition processes are depicted in Fig. 4.1 by using $^{85}Rb_2X^1\Sigma_g(5s+5s)$ ground state potential, $^{85}Rb_2 0_u^+(5s5p_{3/2})$ attractive potential (red curve) for the free to bound transition and $^{85}Rb_2 1_u(5s5p_{3/2})$ repulsive potential (blue curve) for the free to free transition.

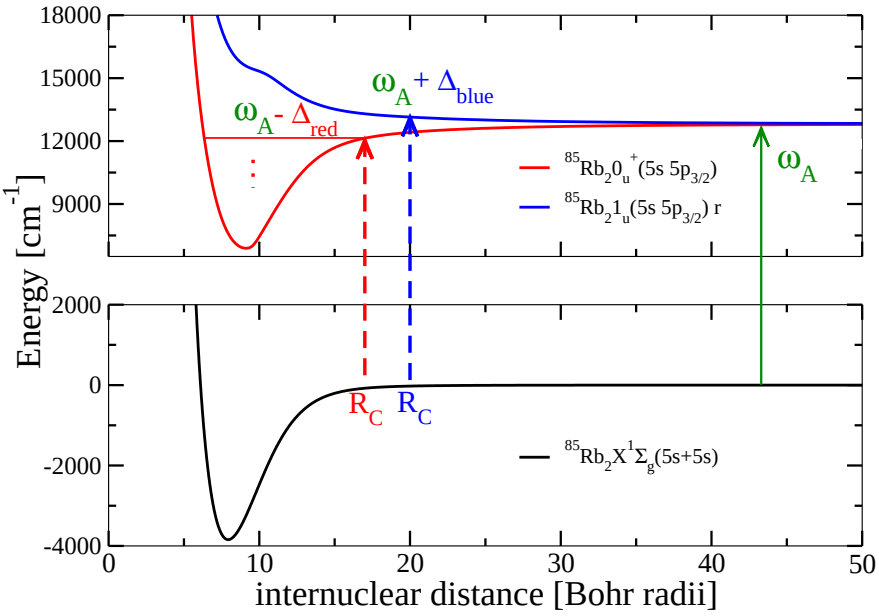

Figure 4.1: Lower panel: $^{85}Rb_2X^1\Sigma_g(5s+5s)$ ground state potential (black curve), upper panel: $^{85}Rb_20_u^+(5s5p_{3/2})$ attractive potential (red curve) and $^{85}Rb_21_u(5s5p_{3/2})$ repulsive potential (blue curve). Atomic transition frequency is represented by ω_A and corresponds to the D_2 atomic resonance. Laser carrier frequency is $\omega_L = \omega_A - \Delta_L$ where Δ_L is the detuning with respect to the asymptote and it refers either Δ_{red} (negative detuning) or Δ_{blue} (positive detuning). In order to excite the ground state atoms to a repulsive excited state, the laser is blue detuned with respect to the atomic resonance. In this case atoms gain $\hbar\Delta_{blue}$ amount of energy and a free to free transition may occur. By employing an attractive excited state potential and red detuning the laser frequency Δ_{red} amount with respect to the disassociation line, a free to bound transition which is resonant with the bound vibrational level indicated by the red horizontal line can be achieved.

4.1.2 Methods for Photoassociation of Ultracold Atoms

Photoassociation of ultracold atoms by using CW lasers is an effective spectroscopic tool to study atomic scattering properties and determination of atomic lifetimes Jones *et al.* (2006). CW lasers are also utilized in order to create ultracold molecules in their electronic ground state via spontaneous emission Masnou-Seeuws & Pillet (2001a). However, the photoassociation rates needed to be increased and production of ground state molecules via spontaneous emissions is not a coherent scheme. The use of short (nanosecond, picosecond) and ultrashort (femtosecond) pulses is proposed to overcome drawbacks (regarding the concerns of coherent control) of CW photoassociation Vala *et al.* (2000); Vardi *et al.* (1997); Zewail (2000). By employing pulse shaping techniques, the dynamics of the molecular formation process as well as the photoassociation rates can be observed and controlled in real time. Coherence properties of the laser pulses are adapted to several control scenarios such as *pump - dump* schemes Koch *et al.* (2006c). A vibrational wave packet on the electronically excited state is created by using a first pulse, so-called pump pulse. The wave packet travels towards the inner turning point of the potential surface. Then a second pulse, so-called dump pulse is employed with a controlled time delay with respect to the pump pulse. The pulse parameters and the time delay between the two pulses are varied in order to improve the efficiency of the population transfer and to selectively populate the ground state vibrational levels. Another proposed coherent control scenario employs *adiabatic Raman passages* Shapiro & Brumer (2003) correlating multi-channel initial wavefunctions to the target states.

4.2 Femtosecond Photoassociation of Ultracold Rb Atoms

In this work, femtosecond laser pulses are employed in order to achieve photoassociation since they possess a large spectrum allowing to tailor the pulse in frequency domain easily. Their very broad spectrum addresses atomic transitions as well as molecular transitions. The photoassociation mostly takes place at the asymptotic regions of the electronically excited state where there is an abundance of the bound levels. In the other hand, at closer internuclear separations of the electronical ground state, the initial distribution of atom pairs is not dense and the initial wavefunction has very small amplitude. Therefore, the atomic transition probability creating hot atoms is several orders of magnitude larger than the molecular transition probabilities. This trade-off is illustrated in Fig. 4.2. Rubidium is chosen as the species of ultracold atoms to photoassociate as this was the atomic species used in the experiments that we model theoretically Eimer *et al.* (2009); Merli *et al.* (2009); Weise *et al.* (2009). As an alkali homonuclear dimer, Rb_2 electronically excited potential surfaces exhibit an R^{-3} asymptotic behavior due to the dipole - dipole interaction while the electronical ground state has R^{-6} asymptotic character.

The creation of hot atoms due to broad spectrum of the femtosecond pulse may hinder the initial ultracold ensemble. In order to prevent losses, at first step the spectral amplitudes corresponding to atomic transitions are suppressed for both D_1 and D_2 lines of the Rb. This is simply done by removing these frequency components in the spectral domain.

4.2.1 Pulse Shaping by Spectral Cut

The procedure to shape pulses is espoused the experimental strategy. In the experiment Mullins *et al.* (2009); Salzmann *et al.* (2008), an ultracold ensemble of gaseous ^{85}Rb atoms is kept in a magneto-optical dark SPOT (spontaneous-force optical trap) Townsend *et al.* (1996) with 10^{11} cm^{-3} atomic densities at the trap temperatures of 100 μK. 90% of the atoms are detected to lie on the $F = 2$ ground hyperfine state. Femtosecond pulses with 4μJ energy, 80 fs

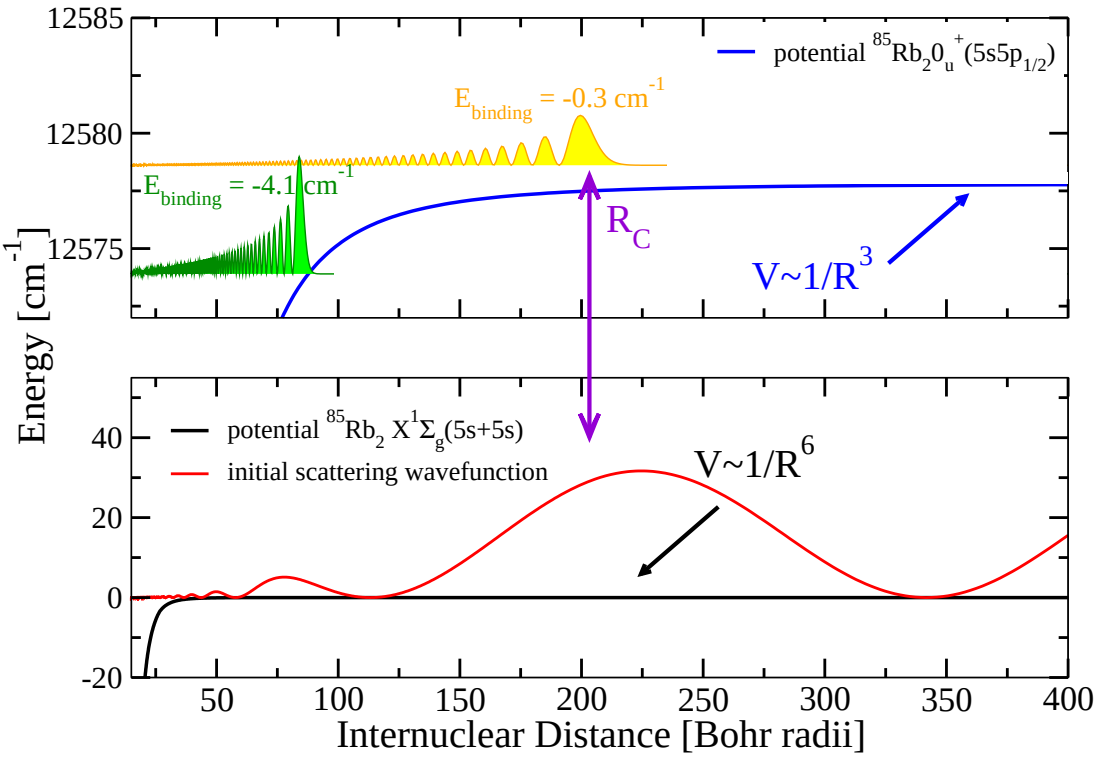

Figure 4.2: Illustration of FC overlap between $^{85}Rb_2$ singlet ground state (black curve) and $^{85}Rb_2 0_u^+$ electronic excited state (blue curve) bound levels below the D_1 resonance. Initial wavefunction (red curve) is chosen to be the scattering state with 100μK energy since it corresponds to the typical temperature of the MOT Mullins *et al.* (2009). Molecular transition probabilities are restricted by the wavefunction overlap at short internuclear separations. Probability of creating a loosely bound level i.e. binding energy of 0.3 cm^{-1} (yellow curve) is larger than creating deeply bound molecules i.e. binding energy of 4.1 cm^{-1} (green curve). R_C is the Condon point where the transition to the 0.3 cm^{-1} bound level is resonant.

fwhm and 100 kHz repetition rate are then shone on the atomic ensemble to study the photoassociation process. In order to prepare the photoassociation pulses, beams with 10% of the output power are sent to the pulse shaper where the spectral composition, phase and amplitude of the pulses can be manipulated. Further technical details of the experimental setup can be found in the references Mullins *et al.* (2009); Salzmann *et al.* (2008).

The initial pulse has 390 cm^{-1} fwhm and it contains the 12 578 cm^{-1} D_1 and the 12 816 cm^{-1} D_2 atomic resonances. The excitation of free-free transitions by the spectral components of the pulse corresponding to these atomic resonances limit drastically the photoassociation efficiency. These spectral components cause loss of atoms from the MOT (magneto optical trap) due to light scattering forces and ionization Salzmann *et al.* (2006). Moreover, the higher frequency components (blue part) of the pulse with respect to these atomic resonances correspond to the antibinding branches of the excited state potential. The effect of the resonant frequencies and the frequencies above them could be suppressed by far detuning the photoassociation laser carrier frequency. However, Franck-Condon factors of the free to bound transition for large detuning are very small due to the very small amplitude of the scattering states at shorter inter-nuclear separations. In the other hand, spectrally shaping the pulse in a way that the resonance frequencies and the frequencies above them are blocked while the frequency components with high amplitude just below the resonance are kept results in higher Franck-Condon overlap for free to bound transitions.

The latter scheme is followed by shaping the photoassociation pulses in a Fourier plane of the zero dispersion compressor. By employing a low-pass filter, all frequencies above the chosen atomic resonance (D_1 or D_2), the respective resonance frequency itself, and some frequencies below this particular line were cut off. In order to achieve molecular transitions below the D_2 line, perturbing frequency components around the D_1 atomic resonance are also removed from the pulse spectrum Merli *et al.* (2009). This procedure is numerically modelled by shaping the pulse in the frequency domain. Firstly, a Gaussian transform - limited pulse in time domain is transformed into frequency domain via Fourier transformation then the disturbing frequencies are

blocked by applying an appropriate $f(w)$ Fermi function

$$f(w) = \begin{cases} 1 - \dfrac{1}{1+e^{\mathbf{a}\,(w-w_1)}} & \text{if } w \leq w_{diff} \\ \dfrac{1}{1+e^{\mathbf{a}\,(w-w_2)}} & \text{if } w > w_{diff} \end{cases} . \tag{4.5}$$

In Eq. 4.5, variable w represents the frequency, w_1 and w_2 are the lower and the upper spectral cut positions with respect to D_2 resonance for the illustrated example in Fig. 4.3. The spectral cut is positioned by comparing the frequency components with $w_{diff} = w_1 + \frac{1}{2}(w_2 - w_1)$. Parameter a determines the steepness of the Fermi function and it is related to the sharpness of the mask used in the experiment. Following the comparison of the experimental results and simulations, it is found out to be a = 2.035 au. For the photoassociation simulations below D_2 resonance, an initial transform - limited pulse with fwhm $\Delta\lambda_L$ = 25 nm, central wavelength λ_L = 785 nm (12 738.85 cm^{-1}), laser power 30 mW at repetition rate 100 kHz and beam radius r_B = 300 μm is used.

The femtosecond photoassociation mechanism is simulated by quantum dynamical calculations for the light-matter interaction of the two-channel Hamiltonian

$$\hat{\mathbf{H}} = \begin{pmatrix} \hat{\mathbf{T}} + V_g(\hat{\mathbf{R}}) & \hat{\mu}E(t) \\ -\hat{\mu}E(t)^* & \hat{\mathbf{T}} + V_e(\hat{\mathbf{R}}) - \Delta \end{pmatrix} \tag{4.6}$$

where $\hat{\mathbf{T}}$, $\hat{\mathbf{R}}$, $V_{g/e}$, $\hat{\mu}$, $E(t)$ and Δ represent the kinetic-energy operator, the inter-nuclear separation, the chosen ground/excited state potential energy surface of rubidium, the transition dipole operator, the electric field of the photoassociation pulse and the detuning of the central frequency of the pulse with respect to the chosen asymptotes, respectively. The electric dipole coupling is represented in the off-diagonal elements of the Hamiltonian. The transition dipole is assumed to be R-independent since the photoassociation transition takes place at the large inter-nuclear separations where transition dipole value is constant. Dipole and rotating wave approximations are employed for constructing the Hamiltonian given in Eq. 4.6 and the couplings between electronic states are not taken into account which is justified in terms of the time scales of the described process.

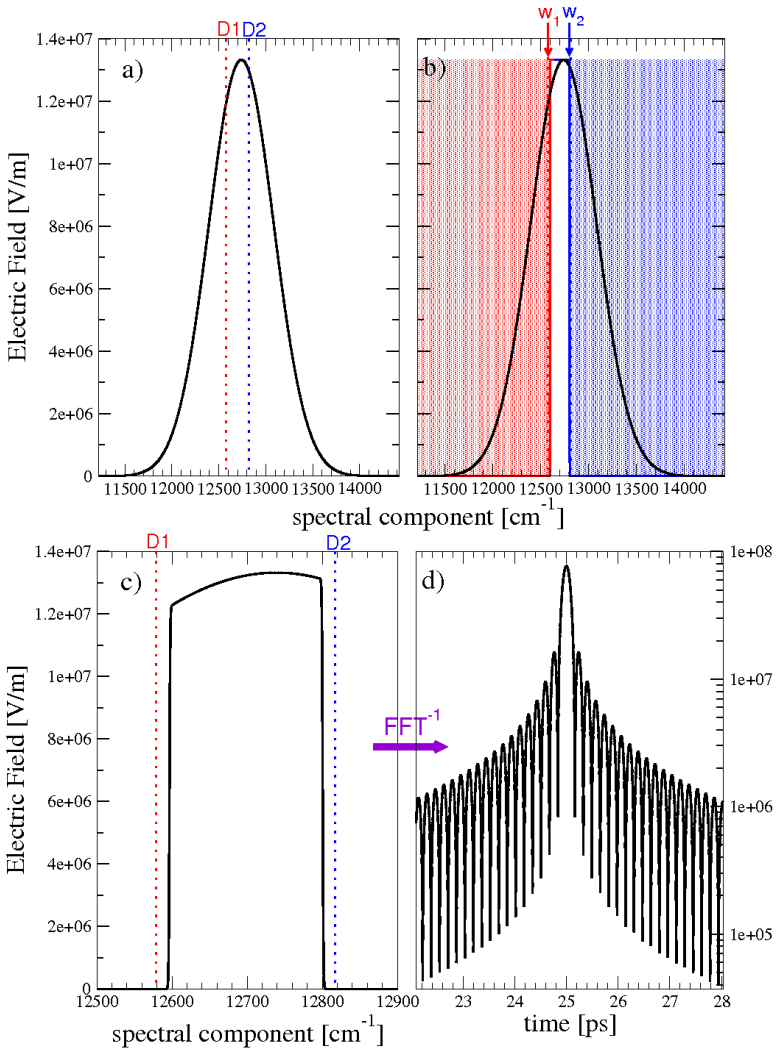

Figure 4.3: a) Gaussian transform - limited pulse is transformed into spectral domain by using FFT. The carrier frequency of the pulse is set to w_L = 12738.85 cm^{-1} (central wavelength λ_L = 785 nm). D_1 (red dotted line) and D_2 (blue dotted line) atomic resonances are shown. b) In order to avoid both atomic resonances, a lower spectral cut is applied at w_1 = -220.0 cm^{-1} and an upper spectral cut is applied at w_2 = -16.0 cm^{-1} both measured with respect to D_2 resonance. This is achieved by employing a Fermi function for the frequencies below the D_1 line (red solid curve) and the frequencies above the D_2 line (blue solid curve). c) The resulting shaped pulse in the spectral domain. d) The shaped pulse is back transformed to the time domain by applying backwards Fourier transformation (FFT^{-1}). Sharp cuts in the spectral domain lead to oscillations and long tails in the time domain.

The potential energy curves of rubidium are obtained by connecting ab initio data at short range Park *et al.* (2001) and $\frac{C_6}{R^6} + \frac{C_8}{R^8} + \frac{C_{10}}{R^{10}}$ asymptotic expansion where the C_i expansion coefficients are taken from Ref. Marte *et al.* (2002). The potential energy curves are then converted into their Hund's case (c) representation by approximating the spin-orbit couplings by their asymptotic values and diagonalizing them as described in Wang *et al.* (1997).

The Hamiltonian is treated on a mapped Fourier grid representation as explained in Chapter 3 of this thesis. The field-free vibrational wavefunctions are obtained by diagonalizing the Hamiltonian for $E(t)$=0 and the time evaluation of the wavefunctions is obtained by solving the time-dependent Schödinger equation

$$i\hbar\frac{\partial}{\partial t}\begin{pmatrix}\Psi_g(R;t)\\ \Psi_e(R;t)\end{pmatrix} = \hat{\mathbf{H}}\begin{pmatrix}\Psi_g(R;t)\\ \Psi_e(R;t)\end{pmatrix} \tag{4.7}$$

where $\Psi_{g/e}(R;t)$ is the ground/excited state time-dependent wavefunction. Time-dependent Schödinger equation of the system given in Eq. 4.7 is solved by employing a Chebyshev propagator as explained in Chapter 3 of this thesis. The scattering state with the energy corresponding to the trap temperature (100 μK) of the ground state potential energy surface is chosen as the initial wavefunction in order to study photoassociation transition. An adequate numerical representation of a quasi-continuum around this scattering energy, requires a large box size. Therefore, typically a grid of size L = 15 000 bohr with N = 1023 or 2047 grid points is employed depending on the choice of the potentials. During the simulations of the photoassociation, it is observed that the dynamics of the system are dominated by the electronic transitions and at the inter-nuclear separations where photoassociation takes place the nodal structure of the scattering states does not affect this transition process. Consequently, simulations with a single initial state justify the photoassociation transitions.

The pulse is described and studied in terms of central wavelength (equivalently carrier frequency), spectral width (fwhm), linear chirp rate, energy and spectral cut-off positions. It is observed that after the sharp cuts in the spectral domain, the pulse gains long tails in the time domain reaching out to few picoseconds around the pulse maxima. As shown in Fig. 4.3, the electric field of

the pulse oscillates with the frequencies of the applied spectral cuts and a beat oscillation pattern with respect to two cuts is observed in the time domain of the pulse.

The prepared photoassociation pulse given the details and shown in Fig. 4.3 is applied to the scattering state with 100μK energy of the $^{85}Rb_2 a^3\Sigma_u^+$(5s + 5s) triplet lowest potential and following photoassociation dynamics on the $^{85}Rb_2 0_g^-$(5s 5p$_{3/2}$) excited state potential is studied. The evolution of the wavefunction on the ground and excited states is shown in Fig. 4.4 with emphasis on the short range (left panels) and long range (right panels) parts. The final wavefunction on the molecular excited state potential (orange curve on the upper panel) created by the photoassociation pulse and the initial wavefunction on the ground state (turquoise curve on the lower panel) has the same nodal structure at long range as indicated by violet dotted lines in Fig. 4.4. The weakly bound excited state molecules have vibrational periods of tens of picoseconds while the timescale of motion of the initial unbound atom pairs which is determined by the MOT conditions is longer than tens of picoseconds. The different time scales of the vibrational periods of created weakly bound excited state molecules and motion of initial atom pairs reveal for the electronic ground state no nuclear dynamics took place on the time scale of the pulse.

In order to prove photoassociation and to search distribution of created excited state molecules on different vibrational levels, the wavepacket on the excited state is projected on the eigenfunctions of this state. The effect of the spectral cut-off position with respect to the D_2 resonance on this vibrational distribution is analyzed. To this end, time dependent simulations are realized and comparison of the effect of two different cut-off positions on the vibrational distribution is presented in Fig. 4.5. The ω_2 cut-off positions with respect to the D_2 line are chosen to be -10 cm^{-1} and -15 cm^{-1} while keeping the ω_1 cut-off position close to the D_1 line is fixed to -218 cm^{-1}. The bars in the upper panel of Fig. 4.5 indicate vibrational distribution on the -27.8 cm^{-1} deep $^{85}Rb_2 0_g^-$(5s 5p$_{3/2}$) excited state potential after the photoassociation pulse is over. On the same figure, the spectral intensities corresponding to the two pulses are indicated by the shaded green and red areas. Here, it is remarked

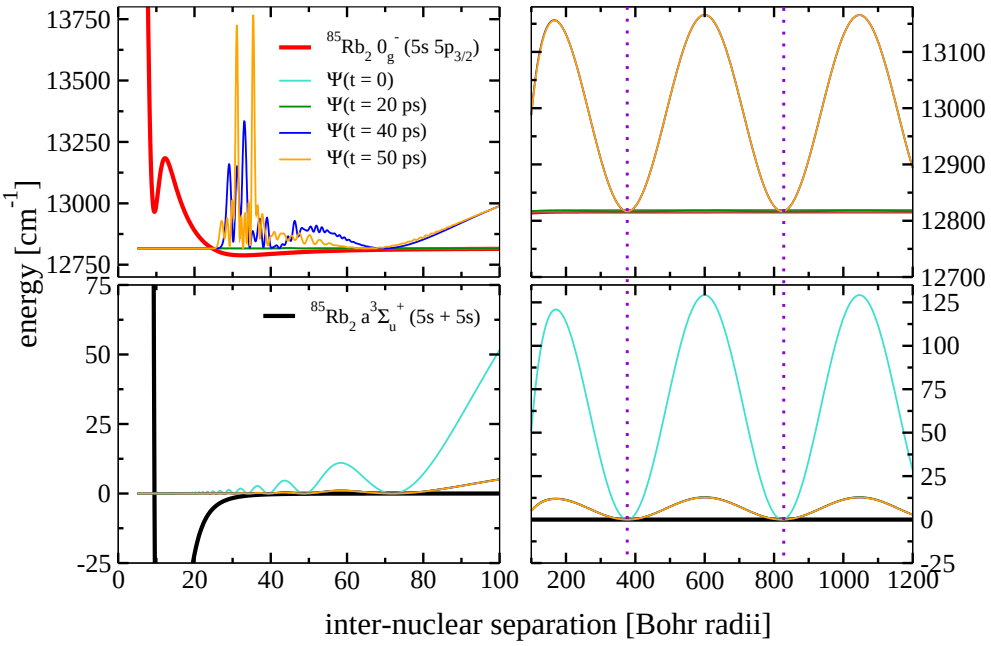

Figure 4.4: Upper panel: Excited state potential of rubidium (red curve) $^{85}Rb_2 0_g^-(5s\ 5p_{3/2})$ and the wavepackets created by the pulse at 0, 20, 40 and 50 ps of the propagation (turquoise, green, blue and orange curves, respectively) on the excited state. Lower panel: Triplet lowest potential of rubidium (black curve) $^{85}Rb_2 a^3\Sigma_u^+(5s + 5s)$ and the part of the wavepacket on the ground state at 0, 20, 40 and 50 ps, respecting the same color coding . Initial wavefunction on the ground state (lower panel, turquoise curve) is chosen to be the scattering state with 100μK energy (corresponds to the MOT temperature for rubidium). The parts of the wavepacket on the excited and on the ground state show the same nodal structure at the long range part of the potential (indicated by violet dottet lines on the right panels) which reveals no nuclear dynamics for the considered time scale.

how the spectrum does not address the most populated bound levels. On the left hand side of this graph the spectral intensities corresponding to the energies of each bound level are plotted. The normalized population of the bound excited state levels is 0.29 10^{-2} and 0.56 10^{-2} for the cases ω_2 = -15 cm^{-1} and ω_2 = -10 cm^{-1}, respectively. However, only a small fraction of the total bound excited state population resides in the vibrational levels resonant within the pulse spectrum. A small portion of the pulse spectrum promotes excitation. The most of the vibrational population lies on the 100th - 129th levels. They have binding energies between 0.1 10^{-1} - 0.2 10^{-6} cm^{-1}. Those very loosely bound levels have bond lengths up to 1000 bohrs. Their population raise from off-resonant excitation. Due to the high peak intensity, long tails of the photoassociation pulse continue interacting with the dipole. This is a transient interaction of the weakly bound molecules and the pulse. In the inset of the upper panel, the vibrational distribution of levels resonant within the pulse spectrum is made visible. Population of these levels are two orders of magnitude less than the off-resonantly populated loosely bound levels. This is due to much smaller free to bound Franck-Condon factors. The vibrational distribution among these levels reproduces the weak-field results in which their population is proportional to the Franck-Condon factors multiplied by the spectral envelope of the pump pulse Poschinger *et al.* (2006); Shapiro & Brumer (2003). The excitation in both weak field and strong field schemes can be understood by noting the decisive quantity as Rabi frequency which is the product of transition dipole and electric field. Since the Franck-Condon factors vary over several orders of magnitude, qualitatively different results are obtained for different regions of the excited-state vibrational spectrum. The resonant levels for the ω_1 = -218 cm^{-1}, ω_2 = -10 cm^{-1} lie up to 18th vibrational level of the $^{85}Rb_2 0_g^-(5s\ 5p_{3/2})$ excited state potential which corresponds to the part of the wavepacket at inter-nuclear separations less than 50 bohrs.

The same procedure is followed in order to monitor the vibrational distribution on the ground state potential and plotted in the lower panel of the Fig. 4.5. The created ground state molecules by projecting the wavepacket on the triplet lowest state of rubidium is 2 orders of magnitude less than the created

excited state molecules. The population in the bound levels of the ground state is calculated to be in the order of 10^{-5} of the initial population.

Simulations are carried out also for different excited state potentials of rubidium. Similar results are obtained when -1252.8 cm^{-1} deep $^{85}Rb_2 1_g(5s\ 5p_{3/2})$ excited state potential is employed and they are shown in Fig. 4.6. In this case, due to the depth of this excited state potential more levels resonant within the pulse spectrum are populated compared to the $^{85}Rb_2 0_g^-(5s\ 5p_{3/2})$ excited state potential. The ratio of the bound excited state levels is 0.27 10^{-2} and 0.52 10^{-2} for the cases ω_2 = -15 cm^{-1} and ω_2 = -10 cm^{-1}, respectively. The results obtained by employing different excited state potentials do not differ in terms of orders of magnitude.

The behavior of the excited and ground state population is studied as a function of applied pulse energy. The population obtained at the end of propagation time (50 ps) on the ground and excited state by employing the photoassociation pulse where the spectral cut-offs are applied on ω_1 = -218 cm^{-1} and ω_2 = -10 cm^{-1} are plotted in Fig. 4.7. The overall and vibrational population of the excited state show in-phase oscillation as a function of the pulse energy. The population oscillation on the ground and excited potential energy surfaces exhibit coherent oscillation. The vibrational population oscillation on the ground state is large when the population oscillation on the excited state is low as trend.

Up to here, the population in the ground and excited states is discussed when the pulse is over. The dynamics of the photoassociation process and the physical mechanism behind it is analyzed in terms of dipole dynamics. This analysis is rendered in Fig. 4.8. In the lower panel of Fig. 4.8 the population in the excited state as a function of time during the application of the pulse is plotted (green curve). Photoassociation pulse after the spectral cuts are applied on ω_1 = -218 cm^{-1} and ω_2 = -15 cm^{-1} with respect to the D_2 line is indicated by the black curve and the normalized excite state population $\int d\mathbf{R}|\Psi_e(\mathbf{R};t)|^2$ is indicated by the green curve. Oscillatory pattern of the pulse due to beating frequencies of the spectral cut-offs is reflected as small modulations on the main oscillation of the excited state population. The transient interaction of

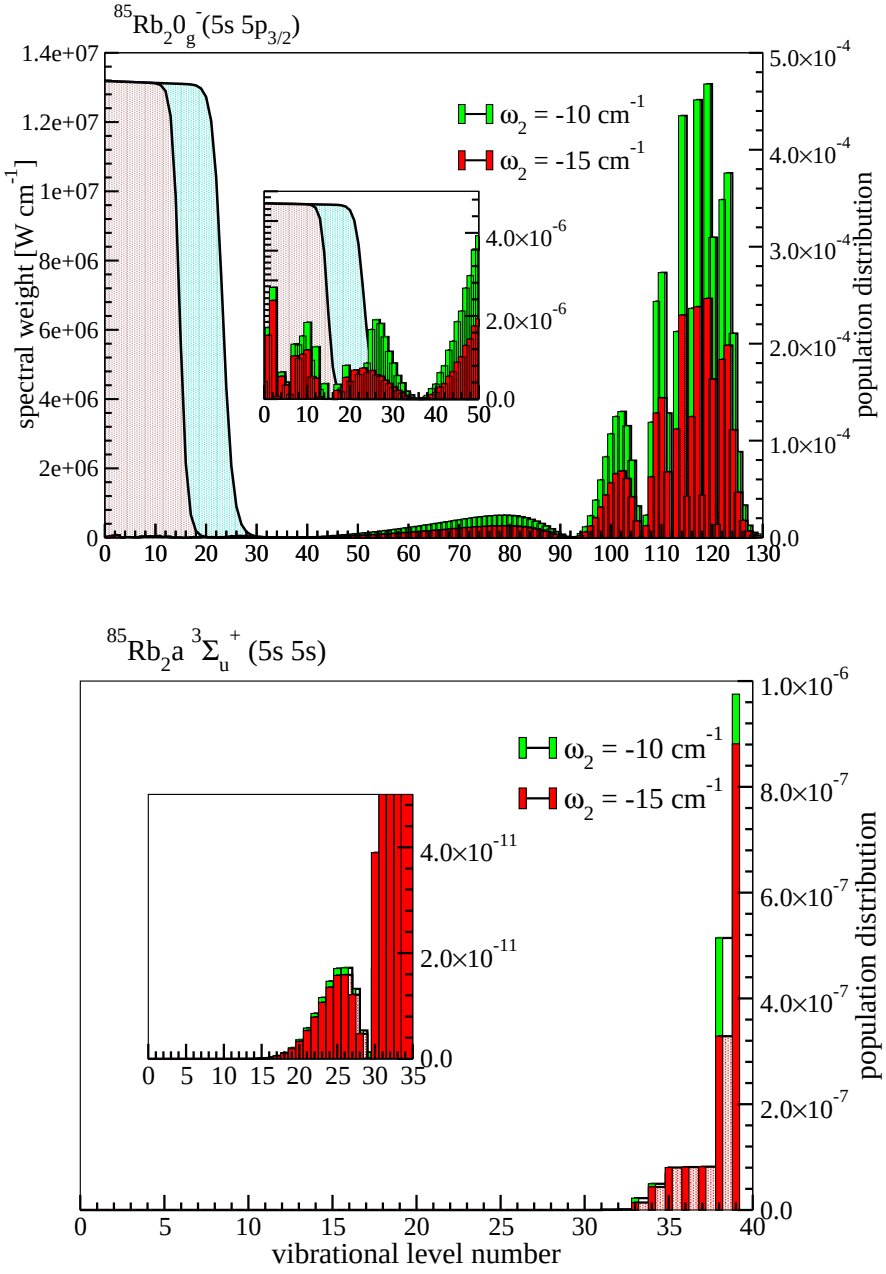

Figure 4.5: Upper panel: Pulse spectrum with respect to the vibrational levels of the $^{85}Rb_2 0_g^-(5s\ 5p_{3/2})$ excited state potential (shaded area) is shown for photoassociation pulses when first cut-off is fixed at ω_1 = -218 cm^{-1} while second cut position is set to ω_2 = -10 cm^{-1} (green) and ω_2 = -15 cm^{-1} (red). Corresponding population distribution on the vibrational levels are shown with the bars respecting the same color coding of the cut positions. Lower panel: Population distribution on the $^{85}Rb_2 a^3\Sigma_u^+(5s\ 5s)$ ground state when the wavepacket is projected onto the eigenlevels of this state. The inset in both cases show a zoom-in for deeper bound levels.

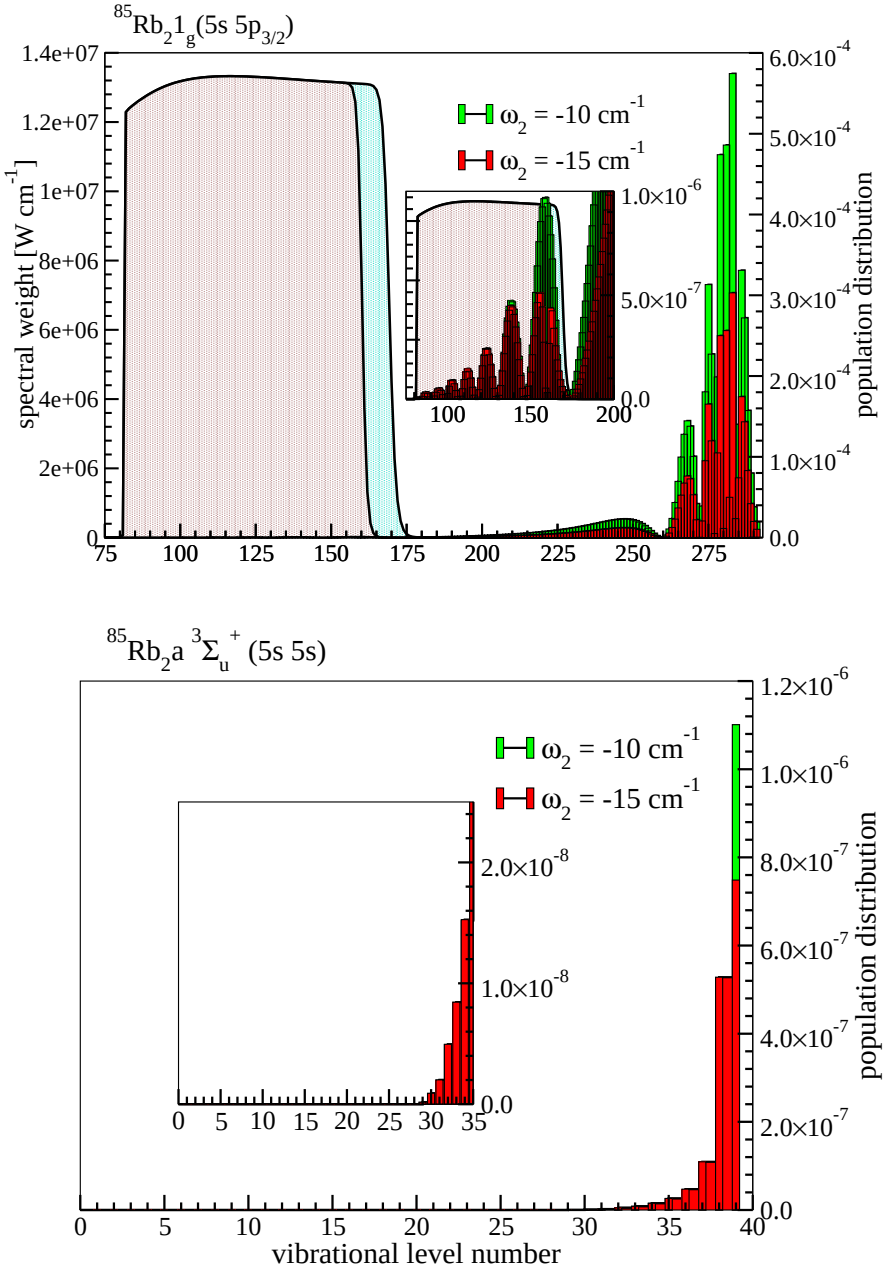

Figure 4.6: Upper panel: Pulse spectrum with respect to the vibrational levels of the $^{85}Rb_2 1_g(5s\ 5p_{3/2})$ excited state potential (shaded area) is shown for photoassociation pulses when first cut-off is fixed at ω_1 = -218 cm^{-1} while second cut position is set to ω_2 = -10 cm^{-1} (green) and ω_2 = -15 cm^{-1} (red). Corresponding population distribution on the vibrational levels are shown with the bars respecting the same color coding of the cut positions. Lower panel: Population distribution on the $^{85}Rb_2 a^3\Sigma_u^+(5s\ 5s)$ ground state when the wavepacket is projected onto the eigenlevels of this state. The inset in both cases show a zoom-in for deeper bound levels.

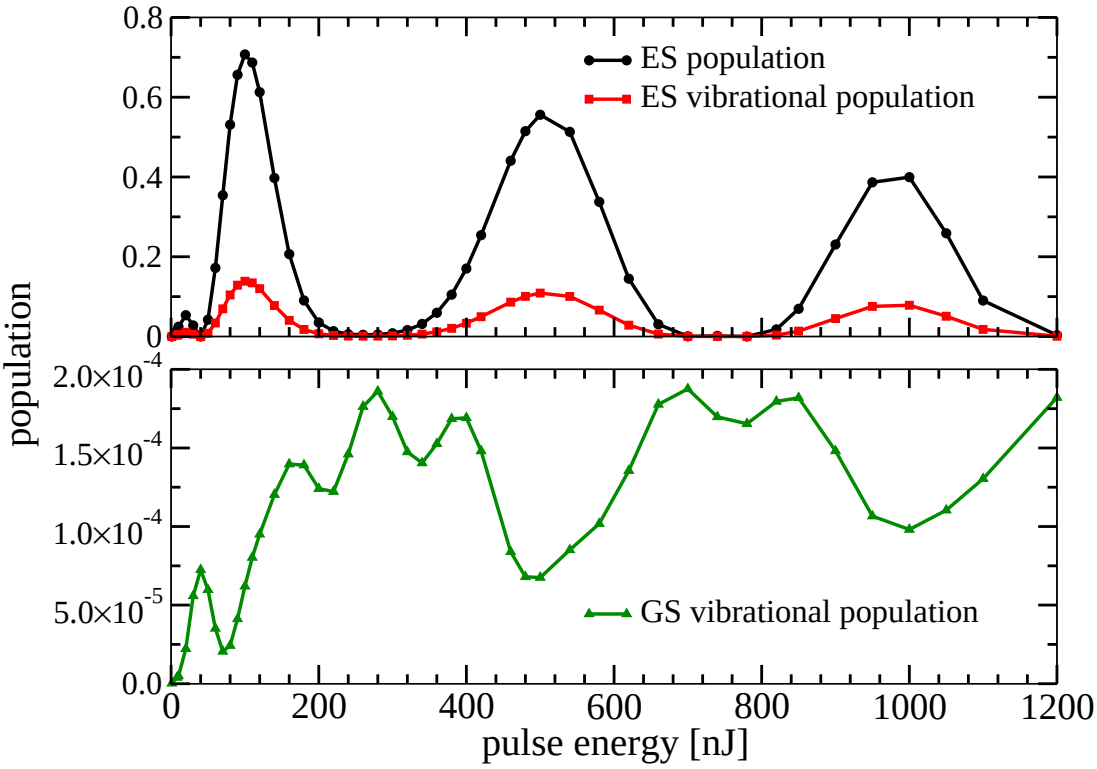

Figure 4.7: Population versus pulse energy. Upper panel: Overall excited state (ES) population (black curve with circles) and ES vibrational population (population only on the bound levels, red curve with squares) on $^{85}Rb_2 0_g^-(5s\,5p_{3/2})$ versus applied pulse energy. Lower panel: $^{85}Rb_2 a^3\Sigma_u^+(5s\,5s)$ ground state (GS) vibrational population versus applied pulse energy. Population undergoes Rabi-cycling by increasing the pulse energy.

the weakly bound molecules and the pulse is governed by the induced transition dipole. This is monitored also via the relative phase between the induced dipole and the field. The derivative of the time-dependent phase of $\int d\mathbf{R}\langle\Psi_g^*(\mathbf{R};t)\hat{\mu}\Psi_e(\mathbf{R};t)\rangle$ as a function of time is shown in the upper panel of the figure by the red curve. The relative phase between the transition dipole $\hat{\mu}(t)$ and the field E(t) is shown by a solid blue curve in the middle panel of the same figure.

During the main peak of the pulse, around t = 25 ps, a dipole is induced by off-resonant excitation. It is at first driven by the strong electric field and follows its oscillation. After the main peak of the pulse is over, the coupling is reduced and the dipole oscillates with its intrinsic frequency close to the D_2 resonance frequency which is indicated by a dotted dashed line in the upper panel of the Fig. 4.8. Because the excited state population lies mostly on the levels close to the dissociation line, cf. Fig. 4.5. The oscillation of the excited state population goes through one period as the relative phase between dipole and field changes by 2π. The dotted blue lines indicate the times when the relative phase crosses odd integer multiples of π. These instances of time coincide with a minima in the oscillation of the excited state population. This oscillation results from a beating between the transition dipole and the field that is oscillating with the cutoff frequency. As the long tail of the photoassociation pulse decays, the oscillations of the transition dipole weaken as well since the energy exchange between pulse and molecules vanishes. Two spectral cut-offs lead to a distinct beat pattern in the amplitude and phase of the electric field which carries over to the all dynamical observables. The dynamics of photoassociation below the D_1 line is also studied where only one cut-off is applied to the spectrum of the pulse and details of this study is reported in reference Merli *et al.* (2009).

The observed coherent transient oscillations Dudovich *et al.* (2002); Monmayrant *et al.* (2006) in the population are studied when two cut-off positions are applied to the spectrum of the pulse resulting the pulse and population in time domain shown in the lower panel of Fig. 4.8. Since the excited state oscillations are caused by the interaction of the molecular dipole with the field these

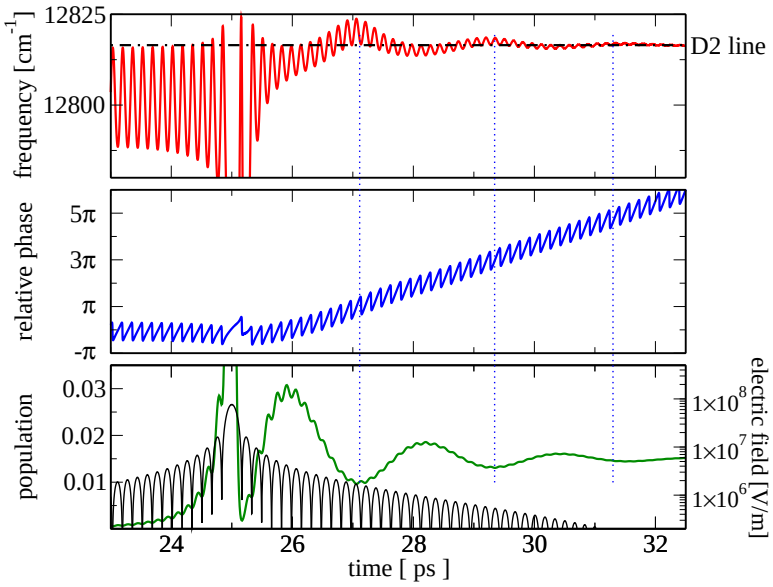

Figure 4.8: Upper panel: The derivative of the time-dependent phase of $\int d\mathbf{R}\langle\Psi_g^*(\mathbf{R};t)\hat{\mu}\Psi_e(\mathbf{R};t)\rangle$ (red curve) and the D_2 resonance line (black dotted dashed line). Middle panel: The relative phase between the transition dipole $\hat{\mu}(t)$ and the field E(t) (blue curve). Lower panel: Pulse in time resulting after the spectral cut-offs at ω_1 = -218 cm^{-1} and ω_2 = -15 cm^{-1} with respect to the D_2 line (black curve). The normalized excited state population (green curve).

modulations are expected to reflect a beating between two or more cut-off frequencies. The depth of the modulations is expected to be due to the difference between these frequencies. In order to gain a detailed understanding of the additional modulations, a spectral analysis is performed and the frequency components and their weights are extracted. The results are shown below for different cut positions in Fig. 4.9 and for two different pulse intensities in Fig. 4.10. For the spectral analysis of the excited state population, the filter diagonalization method is used Mandelshtam & Taylor (1997); Neuhauser (1990). This method allows to extract spectral information from very few oscillation periods. The signal is decomposed into a sum of decaying exponentials as

$$C(t) = \Sigma_k d_k \;\; e^{-i\omega_k t - \Gamma_k t}, \tag{4.8}$$

then the frequencies ω_k, decay constants Γ_k and complex amplitudes d_k are extracted from the signal. Two periods of the data sets are marked by the arrows in all figures Fig. 4.9 and Fig. 4.10. In Fig. 4.9, one cut position is kept constant at -218.0 cm^{-1} while the second cut position relative to the D_2 atomic resonance is varied from -10.0 cm^{-1} (black dashed line) to -15.0 cm^{-1} (red solid line) for a pulse of fwhm corresponding to $\Delta\lambda_L$ = 25 nm and laser power of 30 mW. The square of absolute spectral weights $|d_k|^2$ of the dominating frequencies ω_k are shown in the middle panel of Fig. 4.9, b and c. The zero frequency component of the spectrum gives a constant offset to the oscillations. The cut positions and the difference of the two cut positions ω_k = 203.0 cm^{-1} (red), ω_k = 208.0 cm^{-1} (black) cause the oscillations as well as the modulation on the oscillation. Beside these components, unexpected frequencies like ω_k = 6.5 cm^{-1} (black), ω_k = 200.0 cm^{-1} are also observed. In order to interpret these additional lines, the lifetimes of the corresponding frequencies are examined and shown in the lower panel of Fig. 4.9, d and e. [1] Each frequency corresponding to a cut position or to the difference of cut positions have longer lifetimes than the other frequencies in the spectrum (note the logarithmic scale). The frequencies with short lifetimes are mostly effective at time t = 0 where the pulse is still strong.

[1] Here, *lifetime* stands only for the duration of effectiveness for spectral components. It should not be mixed by the real lifetime of a state.

This indicates that the unexpected lines are caused by the interaction between the molecules and the strong field during the main peak of the pulse.

In order to understand the intensity dependence of the unexpected lines the same spectral analysis is performed for two different intensities. For this analysis the spectral cut-off positions are set to -218.0 cm^{-1} and -10.0 cm^{-1}, the result is shown in Fig. 4.10. For higher intensity (black dashed lines in Fig. 4.9 and Fig. 4.10), a small splitting of the frequencies around the cut positions and around the difference of the cut positions is observed. Moreover, unexpected lines with large spectral weight are observed, cf. middle panel of Fig. 4.10, b and c. For lower intensity (red lines in Fig. 4.10) these unexpected lines disappear. The frequency components at the cut positions and the difference of the cut positions show large, symmetric splitting. The strong intensity dependence of the components with short lifetimes confirms that they are caused by the strong interaction near the pulse maximum.

In Fig. 4.11, the count of Rb_2^+ ions in the experiment is compared to the simulation of the excited state population. The counting of Rb_2 molecules formed via photoassociation is done by using a probe pulse of 500 fs Mullins *et al.* (2009). Therefore, the simulations are also convoluted by using a Gaussian pulse of 500 fs fwhm. In the experimental data, molecular ion count starts from a non-zero value. The creation of molecules incoherently via MOT laser before the application of the photoassociation pulse causes this offset in the molecular ion count for negatives times (i.e., before switching on the photoassociation laser).

The significance of the frequency components close to the resonance are studied by excluding them with a band filter. A representative spectrum of the employed band-filtered photoassociation pulses are shown in the upper panel of Fig. 4.12. The first cut-off position ω_1 is kept -8.0 cm^{-1} while the second cut-off position is varied between +650.0 cm^{-1} and +25.0 cm^{-1} with respect to D_2 resonance. By decreasing the ω_2, more high frequency components corresponding to blue part of the spectrum are added to the pulse. The resulting normalized population versus second cut-off position on the excited state is plotted on the middle panel of Fig. 4.12. The overall excitation is more than the

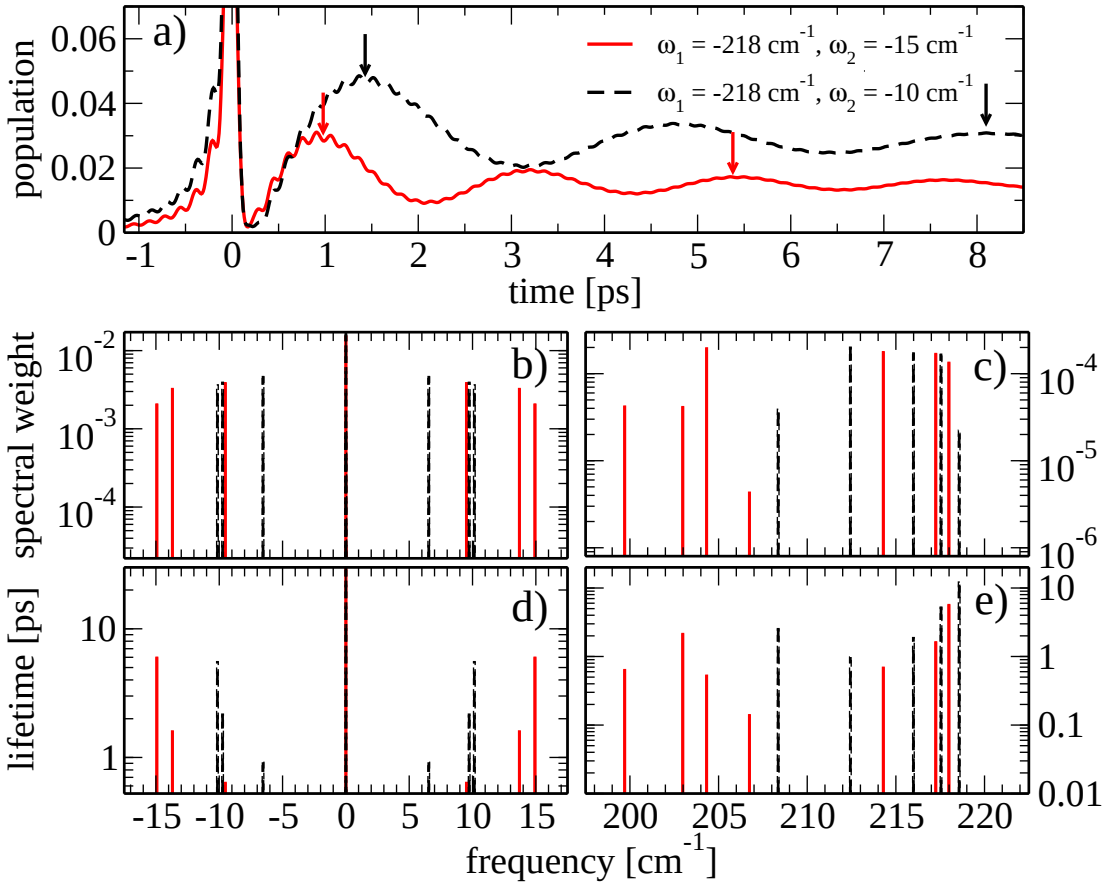

Figure 4.9: Upper panel: Population obtained by using pulses in which one cut position is kept constant at -218.0 cm^{-1} while the second cut position relative to the D_2 atomic resonance is varied from -10.0 cm^{-1} (black dashed line) to -15.0 cm^{-1} (red solid line) for a fwhm corresponding to $\Delta\lambda_L$ = 25 nm and laser power of 30 mW. Middle panel: Absolute spectral weights of the dominating frequencies. Lower panel: Lifetimes of the corresponding frequency components in the logarithmic scale.

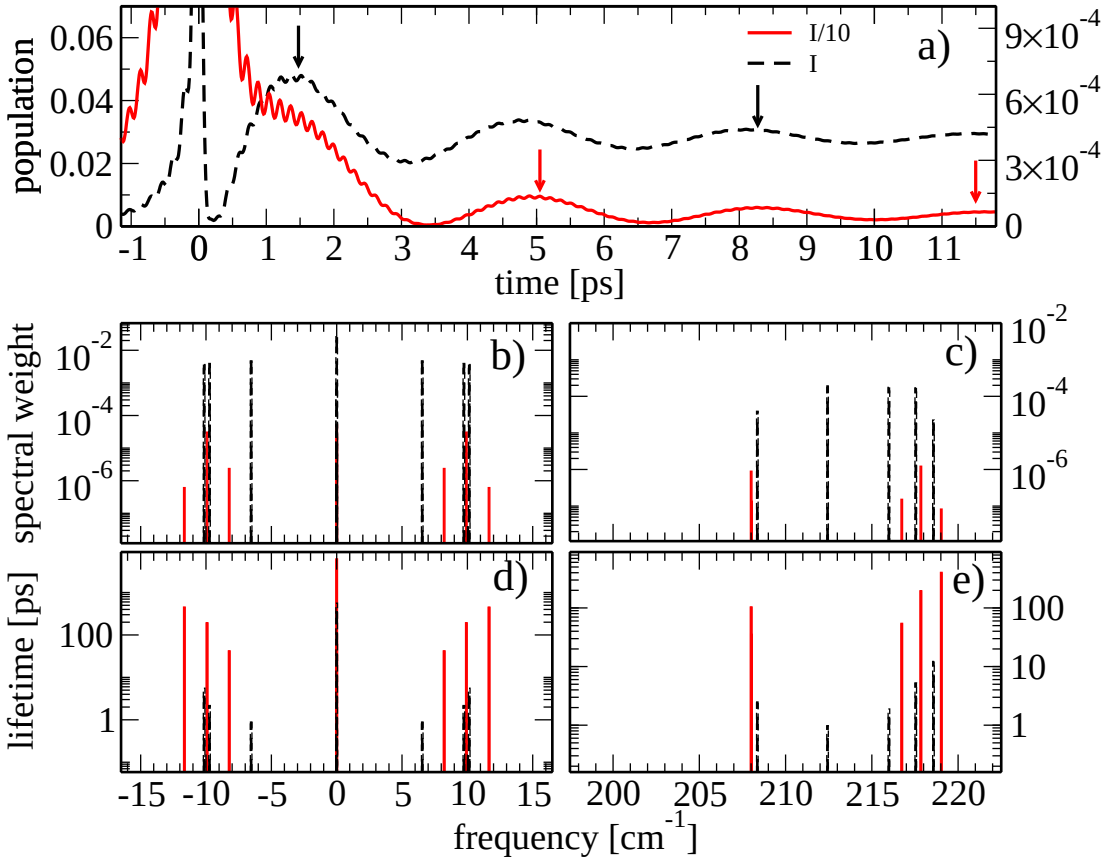

Figure 4.10: Upper panel: Population obtained by using pulses with two different laser intensities corresponding to laser power of P = 0.30 mW (black dashed curve) and P = 0.03 mW (red solid curve), for a pulse with one cut-off position is kept constant at -218.0 cm^{-1} while the second cut-off position relative to the D_2 atomic resonance is varied from -10.0 cm^{-1} and a fwhm corresponding to $\Delta\lambda_L$ = 25 nm. Middle panel: Absolute spectral weights of the dominating frequencies. Lower panel: Lifetimes of the corresponding frequency components in the logarithmic scale.

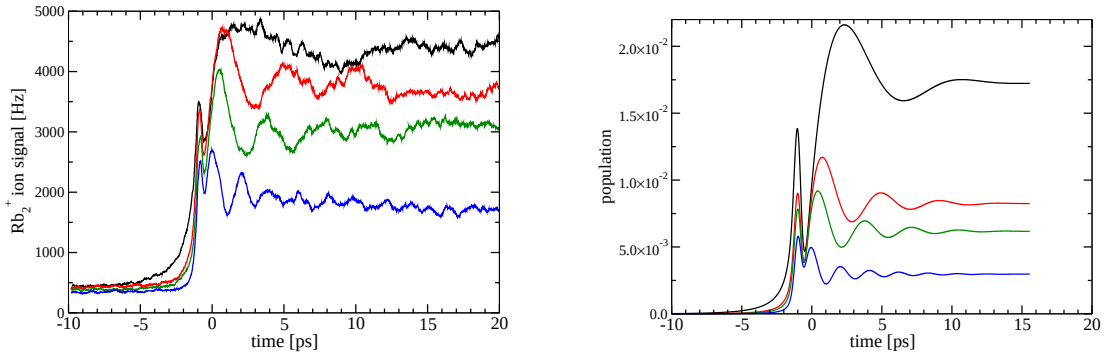

Figure 4.11: Left panel: Rb_2^+ ion count as a function of time. Measurement of Rb_2 molecules resulted from the pump-probe experiment is done by using a photoionization pulse (in addition to the data presented in Merli *et al.* (2009) more measurements of AG Wöste are displayed). Right panel: Corresponding quantum dynamical simulations. In experiments and in simulations the photoassociation dynamics below the D_2 resonance are studied by employing spectral cut-offs where the first one is fixed at ω_1 = -218.0 cm^{-1} while the second one is varied to ω_2 = -4.0 cm^{-1} (black curves), ω_2 = -8.0 cm^{-1} (red curves), ω_2 = -10.0 cm^{-1} (green curves) and ω_2 = -16.0 cm^{-1} (blue curves).

excitation to the vibrational levels but in the same order of magnitude. It is observed that adding more spectral components corresponding to the blue part of the spectrum visibly decreases the excited state population starting from ω_2= +200 cm^{-1}. The vibrational distribution of the ground state is also calculated and compared to the vibrational distribution of the excited state in the lowest panel of the same figure. Adding a small portion of high frequency components to the pulse spectrum slightly improves the excited state population compared to the case where all the blue part of the spectrum is blocked, cf. orange curves in the upper panel of Fig. 4.12 and the right hand side of the lowest panel. If the ω_2 of the band filter is closer to the resonance than +100.0 cm^{-1}, excited state population decreases, cf. blue curves in the upper panel of Fig. 4.12 and the right hand side of the lowest panel. The vibrational distribution of the ground and excited state show opposite behavior with respect to the cut-off position close to the resonance. Adding higher spectral components increase the molecular ground state population while decreasing the molecular excited state population.

Simulations are carried out in order to study photoassociation below the D_1 line, too. Similar results are obtained as in the photoassociation studies below the D_2 line. An exemplary comparison of the simulations and the experimental molecular ion count is presented in Fig. 4.13 for a band filtered pulse spectrum between ω_1 = -40.0 cm^{-1} and ω_2 = -5.0 cm^{-1} with respect to D_1 resonance (12 578.9510 cm^{-1}). In the experimental data (black curve), molecular ion count starts from a non-zero value. Similar to the measurements done for the case of photoassociation below D_2 line, this is due to the creation of molecules incoherently via MOT laser before the application of the photoassociation pulse.

4.2.2 Pulse Shaping by Frequency Chirp

The effect of a linear chirp to the excited state population is searched by applying linear chirp to the spectrum of the pulse where two cut-off positions are also applied at ω_1 = -8.0 cm^{-1} and ω_2 = -218.0 cm^{-1} with respect to the D_2 resonance Merli *et al.* (2009).

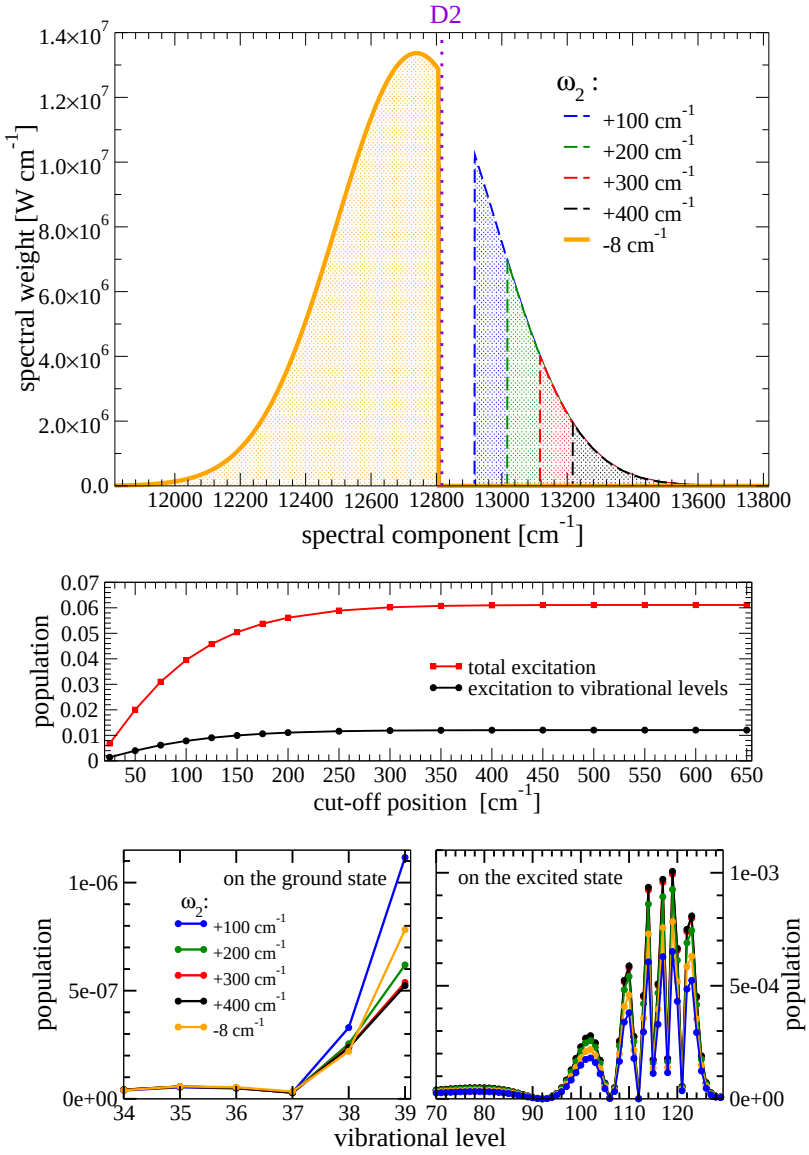

Figure 4.12: Upper panel: Representative spectrum of the band-filtered photoassociation pulses. First cut-off position ω_1 is detuned -8.0 cm^{-1} while the second cut-off position is varied between +400 cm^{-1} (black dashed curve), +300 cm^{-1} (red dashed curve),+200 cm^{-1} (green dashed curve),+100 cm^{-1} (blue dashed curve) with respect to D_2 resonance. The effect of these pulses are compared to the effect of a pulse where only one spectral cut-off is applied at ω_1 = -8.0 cm^{-1} (orange curve). D_2 resonance is marked with the purple dotted line. Middle panel: Normalized population on the whole excited state (red squared curve) and on the vibrational levels (black curve with circles) of the $^{85}Rb_2 0_g^-(5s\ 5p_{3/2})$ excited state potential versus ω_2 cut-off position. Lowest panel: Vibrational population distributions on the $^{85}Rb_2 a^3\Sigma_u^+$(5s + 5s) ground (left hand side) and on the excited state (right hand side).

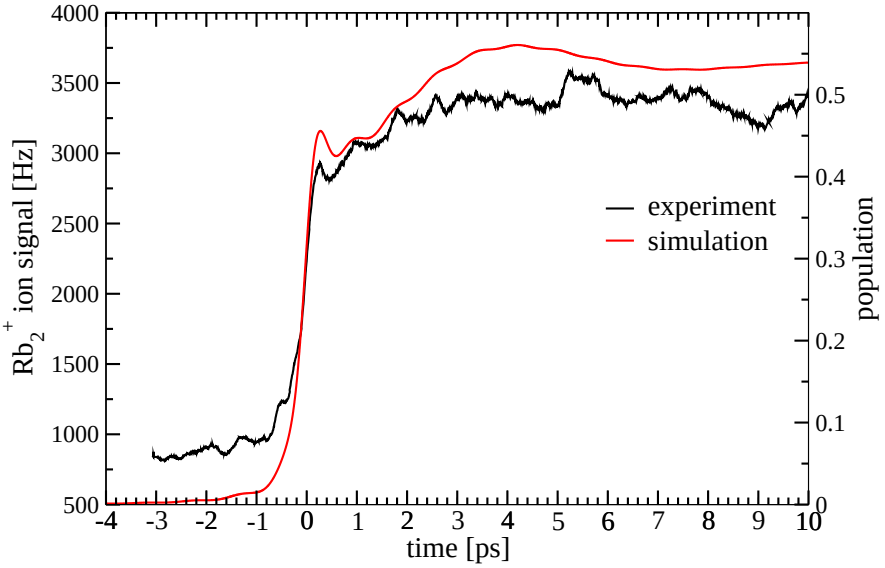

Figure 4.13: Rb_2^+ ion count monitored via pump-probe signal measurement (black curve, Weise *et al.* (2009)) fits very well to the quantum dynamical simulations (red curve). For this exemplary case, a photoassociation pulse is employed with the spectrum in which the frequencies between ω_1 = -40.0 cm^{-1} and ω_2 = -5.0 cm^{-1} with respect to D_1 resonance are blocked. In the experimental data, molecular ion count starts from a non-zero value due to the existence of molecules in the MOT before the propagation starts.

In general the phase of an electric field E(t) can be modulated. E(t) can be written in terms of a temporal envelope $S(t)$ which is a Gaussian in this study, E_0 electric field maximum and instantaneous frequency $\omega(t)$

$$E(t) = \frac{1}{2}E_0 S(t)(e^{i\omega(t)t} + e^{-i\omega(t)t}) \quad (4.9)$$

$$= \frac{1}{2}E_0 S(t)(e^{i\omega_L t}e^{i\frac{d\varphi(t)}{dt}t}) + cc. \quad (4.10)$$

The frequency $\omega(t) = \omega_L + \frac{d\varphi(t)}{dt}$, consists a constant carrier envelope frequency of the electric field ω_L and the phase modulation $\varphi(t)$.

Taylor expansion of the phase modulation $\varphi(t)$ around a reference time instant t_0 can be written as

$$\varphi(t) = \varphi(t_0) + \frac{d\varphi(t)}{dt}|_{t_0}(t-t_0) + \frac{1}{2}\frac{d^2\varphi(t)}{dt^2}|_{t_0}(t-t_0)^2 + \frac{1}{6}\frac{d^3\varphi(t)}{dt^3}|_{t_0}(t-t_0)^3 ... \quad (4.11)$$

The first term in the expansion $\varphi(t_0)$ is the constant phase of the field, second term is related to the shift of ω_L with respect to frequency. The following terms in the expansion $\chi_2 = \frac{d^2\varphi(t)}{dt^2}\,|_{t_0}$ and $\chi_3 = \frac{d^3\varphi(t)}{dt^3}\,|_{t_0}$ gives the linear and quadratic chirps, respectively. They describe the change of the instantaneous frequency in time. If the high (low) frequency components travel faster than the low (high) frequency components of the pulse leading edge, the pulse is so-called up(down)-chirped or positively(negatively) chirped.

Equivalently, electric field in spectral domain $\tilde{E}(\omega)$ can be written in terms of its spectral amplitude $\tilde{S}(\omega)$ and its phase as

$$\tilde{E}(\omega) = \tilde{S}(\omega)e^{-i\varphi(\omega)} \tag{4.12}$$

after a Fourier transformation.

Taylor expansion of the phase follows

$$\varphi(\omega) = \varphi(\omega_L)+\frac{d\varphi(\omega)}{d\omega}|_{\omega_L}(\omega-\omega_L)+\frac{1}{2}\frac{d^2\varphi(\omega)}{d\omega^2}|_{\omega_L}(\omega-\omega_L)^2+\frac{1}{6}\frac{d^3\varphi(\omega)}{d\omega^3}|_{\omega_L}(\omega-\omega_L)^3... \tag{4.13}$$

where the first term is constant, second term gives the shift of the pulse in time, second and third terms are the linear and quadratic chirps, respectively.

By omitting higher order expansion terms and considering only linear spectral chirp rate $\chi_2\prime = \frac{d^2\varphi(\omega)}{d\omega^2}$, the electric field can be expressed as

$$\tilde{E}(\omega) = \tilde{E}_0 e^{-\frac{(\omega-\omega_L)^2}{2\sigma_w^2}-i\chi_2\prime\frac{(\omega-\omega_L)^2}{2}}. \tag{4.14}$$

The chirp rate $\chi_2\prime$ causes a phase shift of each spectral component of the field. The Fourier transform of $\tilde{E}(\omega)$ results in electric field in time domain $E^c(t)$ and can be expressed in the following compact form

$$E^c(t) = E_0\sqrt{f}e^{-\frac{(t-t_0)^2}{2\sigma_t^{c2}}}e^{-i\frac{(t-t_0)^2}{2}\chi_2} \tag{4.15}$$

where the factor f represents the stretch of the pulse in time, χ_2 the resulting chirp rate in time domain and σ_t^c is the standard deviation of the chirped pulse in time domain. The σ_t^c of the Gaussian envelope of the chirped pulse $E^c(t)$ is

$$\sigma_t^c = \sqrt{\frac{1}{\sigma_w^2}+\chi_2\prime^2\sigma_w^2}. \tag{4.16}$$

The chirp rate in time χ_2, is given by

$$\chi_2 = \frac{\sigma_w^2}{\sigma_t^2}\chi_2\prime \tag{4.17}$$

where σ_t is the standard deviation of the unchirped pulse in time domain.

Chirping results in a prolongation of the pulse in the time domain reducing the local field intensity with a factor of $\sqrt{f}$ as seen in the Eq. 4.17 to conserve the total pulse energy where

$$f = \sqrt{\frac{2\sigma_w^2}{(\sigma_w^4 + \frac{1}{\chi_2\prime^2})} + 1}. \tag{4.18}$$

The factor f can be represented in terms of standard deviation σ_t in time domain as

$$f = \sqrt{1 + \frac{2\chi_2\prime^2}{\sigma_t^2}}. \tag{4.19}$$

One can notice from the definition of the transform limit $\sigma_w^2\sigma_{t(TL)}^2 = 1$, in the case of a chirped pulse $\sigma_w^2\sigma_t^{c2} = (1+\chi\prime^2\sigma_w^2)$ is greater than 1. Thus the frequency chirp prolongs the pulse duration in time domain while keeping the spectral band width unchanged in the frequency domain. Keeping the pulse energy constant results reduction in the peak intensity. Both up-chirped and down-chirped pulses caused decrease in the excited state population. Applied chirp factors and their effects on the vibrational population of the $^{85}Rb_2 0_g^-(5s\ 5p_{3/2})$ excited state potential are plotted in Fig. 4.14. Contrary to the proposals done previously Luc-Koenig *et al.* (2004); Vala *et al.* (2000), an enhanced photoassociation is not observed in this case. In this study different than the studies explained in references Luc-Koenig *et al.* (2004); Vala *et al.* (2000), off-resonant excitation dominates the dynamics of the system. The proposed enhancement schemes with frequency chirp in these references requires mutual interaction of wavepacket rolling down the potential curve and the coupling with the field of laser on a timescale of picoseconds. Such an interplay between nuclear and electronic dynamics is not observed with chirped femtosecond pulses. The linear chirp affect the dynamics of the induced dipole and shifts the peak of the population oscillations arising from the energy exchange between the induced

dipole and the electric field of the pulse. Dynamics of the system are therefore very sensitive to phase manipulations of the pulse which affect the relative phase between dipole and field. Applied chirp in addition to the spectral cut-offs strongly influences the ultra fast dipole dynamics. Since the excitations in this system are long range and can be reduced to a two-level system model, the interaction between the molecule and the field is also analyzed in terms of the evolution of the Bloch vectors and presented in reference Merli *et al.* (2009).

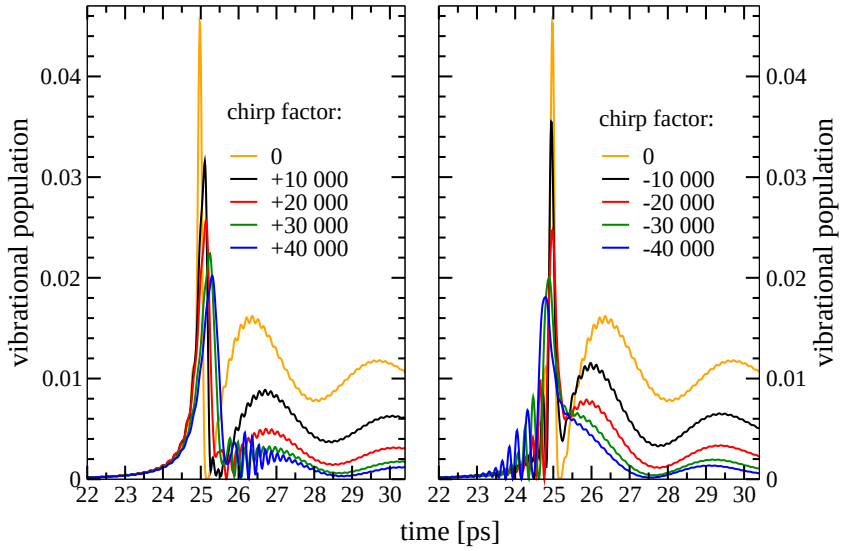

Figure 4.14: Vibrational populations on the $^{85}Rb_2 0_g^-(5s\ 5p_{3/2})$ excited state obtained by chirped pulses with the chirp factors (χ_2) of 10 000 fs^2 (black curve), 20 000 fs^2 (red curve), 30 000 fs^2 (green curve) and 40 000 fs^2 (blue curve) compared to the vibrational population without chirp (orange curve). Left panel: Chirp factors are chosen to be positive. Right panel: Chirp factors are chosen to be negative.

4.2.3 Adding a Phase Step and a Phase Window to the Pulse Spectrum

Transient population enhancement possibilities are searched by applying a spectral phase function $e^{i\phi}$ to the pulse spectrum.

In the case of a "resonant" transition, the off-resonant terms (both blue and red detuned components) with respect to the transition frequency create destructive interferences and the final transition amplitude depends only on the resonant terms. Application of an anti-symmetric, i.e. step-wise phase function inverts the sign of the spectral components about the resonance, inducing constructive interference and therefore maximizing the transient transition amplitude Dudovich *et al.* (2002).

Phase function $e^{i\phi}$ is added step-wise to the band filtered pulse spectrum in which spectral cut-offs are applied to ω_1 = -8 cm^{-1} and ω_2 = +200 cm^{-1} with respect to D_2 resonance. Position of the phase step ω_{step} is varied between -450 cm^{-1} and +450 cm^{-1} with respect to D_2 resonance. Phase ϕ is varied between $\pi/8$ and $3\pi/4$. The spectrum and the resulting vibrational populations with respect to applied phases are plotted in Fig. 4.15. Application of phase step to spectral components below the D_2 resonance reduce the vibrational population on the molecular excited state. However, the behavior of the vibrational population versus ω_{step} is not symmetric, because the applied photoassociation pulse is not symmetric due to removal of disturbing frequencies around the atomic resonance by the band filter. A turning point is observed at 12 881 cm^{-1} (+ 65.0 cm^{-1} with respect to D_2 resonance). An enhancement in the population up to a factor of 1.25 is calculated in this scheme which is the half of the enhancement observed for a "resonant" transition explained in reference Dudovich *et al.* (2002).

Since the non-symmetric phase function can change the amount and the sign of the contributions from the spectral components where $\omega \geq \omega_{step}$, enhancement possibilities with a different pulse spectrum are searched. This time a band-filtered spectrum which consists more blue part, i.e. ω_2 = +50 cm^{-1} is employed and phase function is applied for $\phi = \pi/2$ since this is the phase with largest impact as displyed in Fig. 4.15. In this case vibrational population

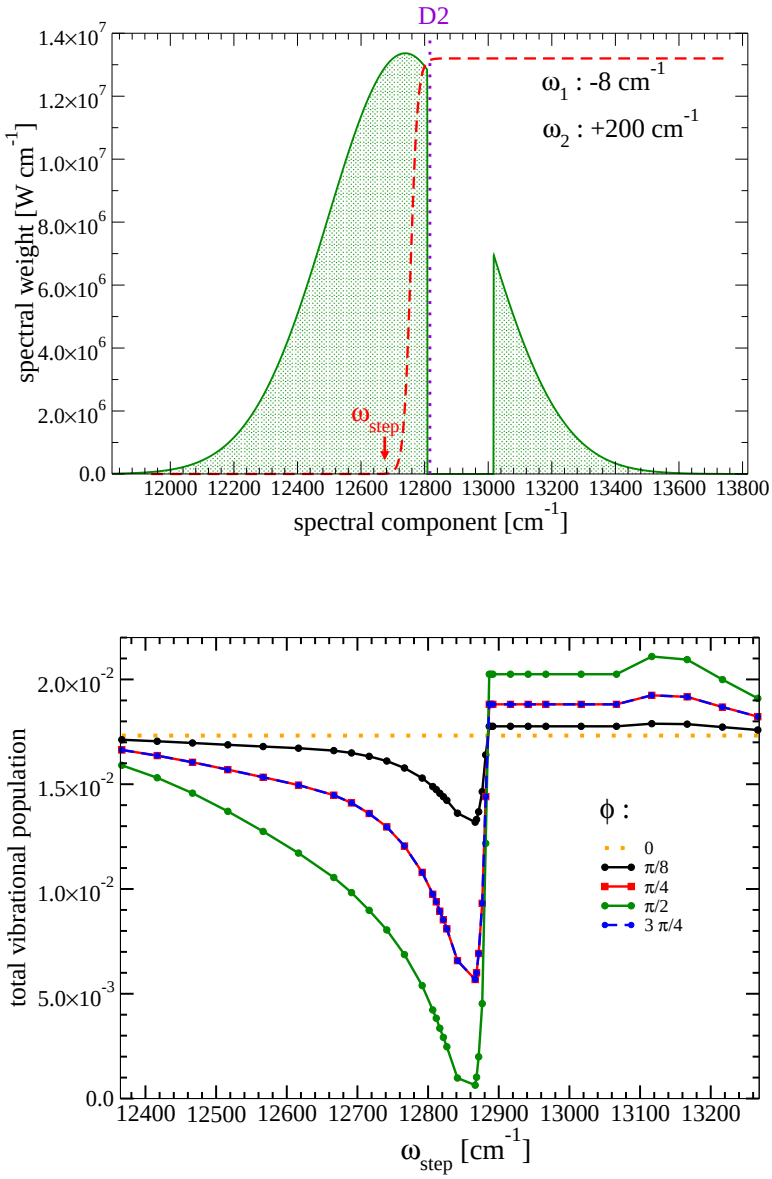

Figure 4.15: Application of an additional phase $e^{i\phi}$ to the band filtered spectrum of the pulse starting from ω_{step}. Upper panel: A pulse spectrum which gives high population transfer is chosen as indicated in Fig. 4.12 with cut-off positions applied to ω_1 = -8 cm^{-1} and ω_2 = +200 cm^{-1}. Phase is applied starting from ω_{step} which is varied between -450 cm^{-1} and +450 cm^{-1} with respect to D_2 resonance. D_2 resonance is indicated by the purple dotted line. Lower panel: Obtained vibrational populations on the $^{85}Rb_2 0_g^-(5s\ 5p_{3/2})$ excited state after 50 ps propagation for $\phi = \pi/8$ (black curve), $\pi/4$ (red curve), $\pi/2$ (green curve) and $3\pi/4$ (blue curve). Vibrational population without additional phase is indicated by the orange dotted line.

is increased up to a factor of 4.00 compared to the case of $\phi = 0$ as shown in Fig. 4.16. As explained and plotted in Fig. 4.12, pulse spectrum which consists high frequency components close to the atomic resonance leads to decreasing vibrational population in the excited state. Application of the step-wise phase function brought constructive contribution from these disturbing frequency components. In Fig. 4.16, the vibrational population versus step position is plotted for two different pulse spectrums. The black curve indicates population obtained by employing the pulse spectrum where the frequency components between ω_1 = -8 cm^{-1} and ω_2 = +50 cm^{-1} are blocked and the phase function $e^{i\pi/2}$ is applied for $\omega \geq \omega_{step}$. The population obtained by the same pulse spectrum without additional phase is indicated by the black dotted line. Maximum enhancement is obtained for ω_{step} = +200 cm^{-1}. Similar behavior and turning point is observed as in the previous case where ω_2 = +200 cm^{-1}. Although more population enhancement is achieved by applying the phase step, the population obtained by the pulse spectrum which consists less blue part is higher, cf. green curve in Fig. 4.16. This is mainly due to sign conversion of the contributions from the spectral components which are already constructive without additional phase.

The derivative of the time-dependent phase of the dipole and the vibrational population on the excited state versus time are plotted in Fig. 4.17 obtained by employing the band filtered pulse spectrum between ω_1 = -8 cm^{-1} and ω_2 = +50 cm^{-1} with (black curve) and without (blue curve) phase function $e^{i\pi/2}$. Phase step is placed at ω_{step} = +100 cm^{-1}. Application of the phase shifts the position of maximas in the derivative of the time dependent phase of the dipole. Thus interaction of dipole and the field differs for the cases with and without additional phase. The main oscillation period of the transient population remains the same as displayed in the lower panel of Fig. 4.17. However, additional phase affects the overall population amplitude and the small modulations on top of the main oscillation, cf. inset in the lower panel of Fig. 4.17.

A similar analysis for additional phase effects is done by employing the additional phase function only on a certain spectral window. Since profiting more from the idle part of the photoassociation pulse is aimed, a band filtered

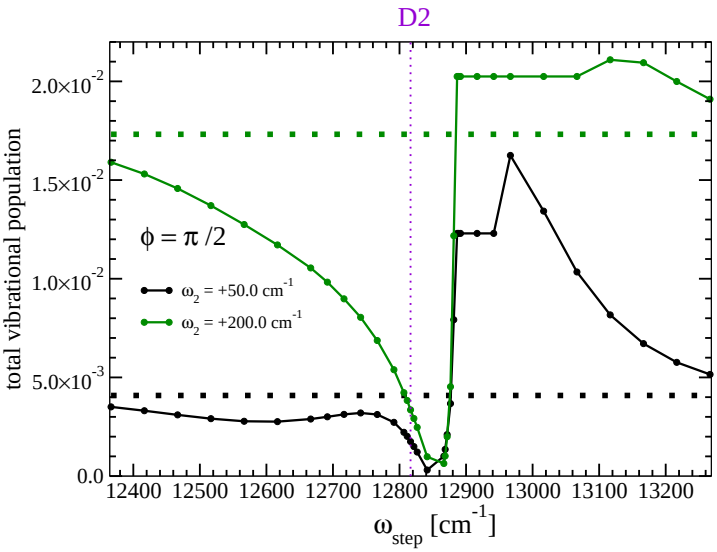

Figure 4.16: Vibrational population versus phase step position ω_{step} is plotted for two different band-filtered pulse spectrums where first cut-off position ω_1 is set to -8 cm^{-1} while second cut-off position ω_2 is set to +200 cm^{-1} (green curve) and to +50 cm^{-1} (black curve). Phase function is applied for $\phi = \pi/2$. For each pulse spectrum, the vibrational population obtained without additional phase is indicated by the dotted line respecting the same color coding. D_2 resonance is indicated by the purple dotted line.

pulse spectrum consisting more high frequency components is chosen for the analysis. The spectral cut-offs are placed at ω_1 = -8 cm^{-1} and ω_2 = +50 cm^{-1} in the pulse spectrum as shown on the left panel of Fig. 4.18. An additional phase $e^{i\phi}$ with $\phi = \pi/2$ to the spectral window between $\omega_{win.1}$ and $\omega_{win.2}$ of this pulse is employed and the vibrational population on the $^{85}Rb_20_g^-(5s\ 5p_{3/2})$ excited state is plotted for different window widths on the right panel of Fig. 4.18. The configuration is chosen such as the second foot of the phase window is kept at $\omega_{win.2}$ = 300 cm^{-1} while the first foot $\omega_{win.1}$ is varied between 0 and 200 cm^{-1}. The maximum population enhancement is observed for phase window position of $\omega_{win.1}$ = 150 cm^{-1} , $\omega_{win.2}$ = 300 cm^{-1}. For this configuration the obtained vibrational population is 5.4 times higher than the case without any

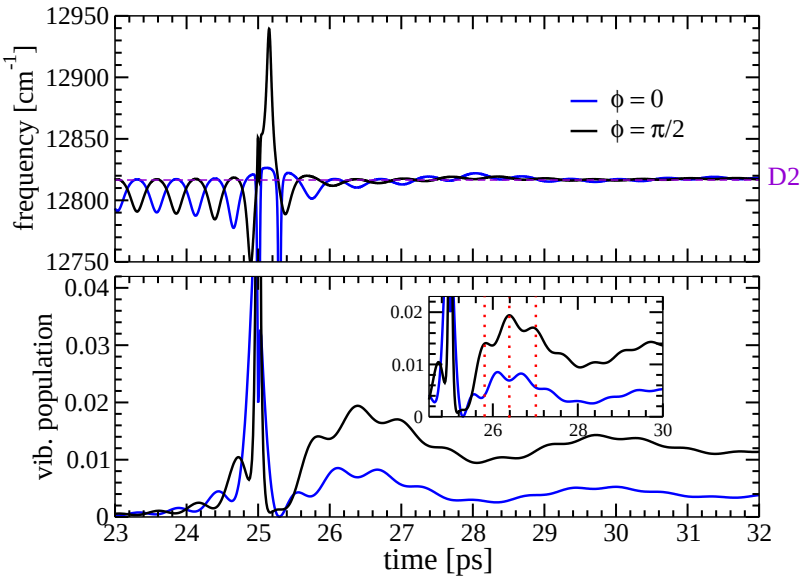

Figure 4.17: Differential phase of the dipole and the vibrational population versus time obtained by employing the band filtered pulse spectrum between ω_1 = -8 cm^{-1} and ω_2 = +50 cm^{-1} with (black curve) and without (blue curve) phase function $e^{i\pi/2}$. Upper panel: The derivative of the time-dependent phase of the dipole. Application of the phase shifts the position of maximas and modifies the form of the peak corresponds to the pulse maxima at about 25 ps. Lower panel: Vibrational population on the $^{85}Rb_2 0_g^-(5s\ 5p_{3/2})$ excited state. Splitting of the differential phase of the dipole causes the double peak in the population for the case without additional phase (blue curve). Application of phase for $\phi = \pi/2$ removes the splitting and thus the double peak structure in the population (black curve). The inset shows the population oscillation for a short time scale and the effect of the additional phase to the period of the modulations on top of the main oscillation is indicated by the red dotted lines.

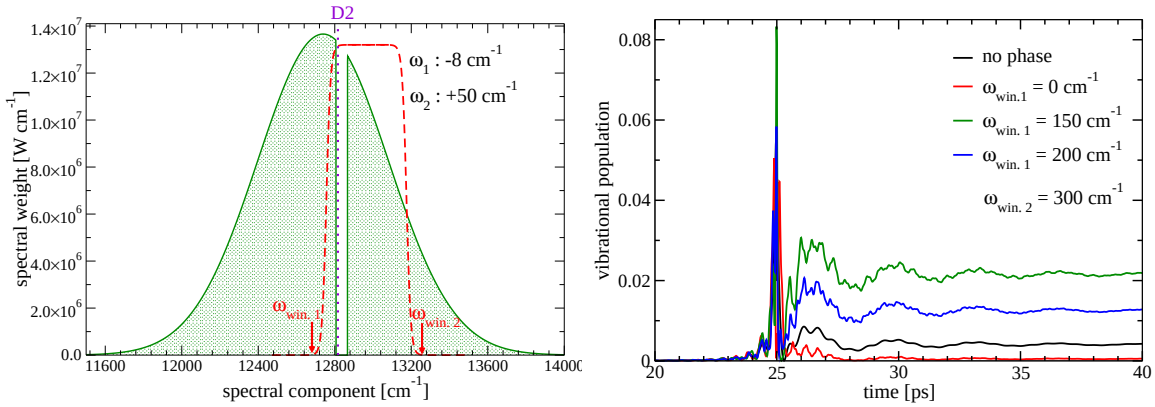

Figure 4.18: Application of an additional phase $e^{i\phi}$ with $\phi = \pi/2$ to the band filtered spectrum of the pulse within a certain spectral window. Left panel: Filtered pulse spectrum between ω_1 = -8 cm^{-1} and ω_2 = +200 cm^{-1} is indicated by the green shaded area. The phase function is applied to this spectrum between $\omega_{win.1}$ and $\omega_{win.2}$. D_2 resonance is indicated by the purple dotted line. Right panel: Vibrational population on the excited state obtained by employing different phase windows. The second foot of the phase window is kept at $\omega_{win.2}$ = 300 cm^{-1} while the first foot $\omega_{win.1}$ is varied between 0 and 200 cm^{-1}.

additional phase and 1.3 times higher than the maximum vibrational population obtained by employing a phase step as shown in Fig. 4.16. Thus, almost the same amount of vibrational population is acquired by employing a pulse consisting more blue part of the spectrum which had disturbing frequencies for molecular formation before this phase manipulation.

4.2.4 Scan with a Spectral Window

The effect of the spectral components to the molecular formation is also studied by moving a narrow spectral window around the atomic resonance Eimer *et al.* (2009). The molecular population is calculated at 25.0 ps (the time instance corresponding to the pulse maxima) and at 50.0 ps (the end of propagation). A spectral window of 13.0 cm^{-1} is used for photoassociation simulations below the D_1 and D_2 resonances following the experiment presented in reference Eimer *et al.* (2009). Simulation results regarding the photoassociation below

the D_2 line are presented here. The narrow spectral window is moved around

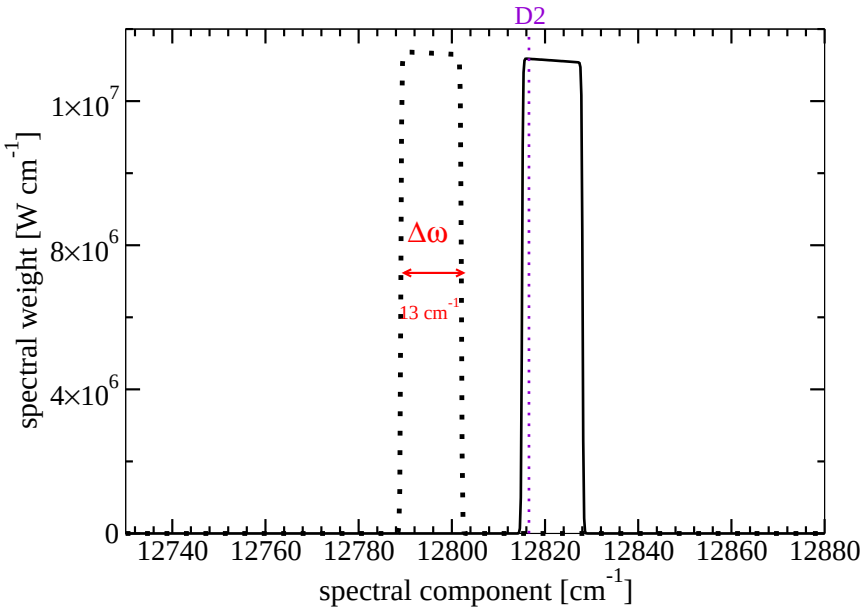

Figure 4.19: A spectral window of 13.0 cm^{-1} (black curves) is employed to study photoassociation below the D_2 line. The center of the spectral window is shifted starting from -21.0 cm^{-1} until +21.0 cm^{-1} with respect to the D_2 resonance which is indicated by the purple dotted line.

the resonance as plotted in Fig. 4.19. The calculated excited state population, cf. Fig. 4.20 is symmetric around the resonance between -10.0 cm^{-1} and +10.0 cm^{-1} for both red and blue detuned pulses with respect to the resonance. This is not surprising since the observed dynamics are originated from electronic excitations and the process is dominated by the high laser peak intensity. However, the excited state population obtained at the end of propagation with large positive detuning decreases faster compared to the population obtained by employing the same amount of negative detuned pulses. The behavior of excited state population versus detuning obtained at the end of the propagation drastically differs from the one obtained at the time instance coinciding the pulse maximum. The first case exhibits a maximum when the center of the

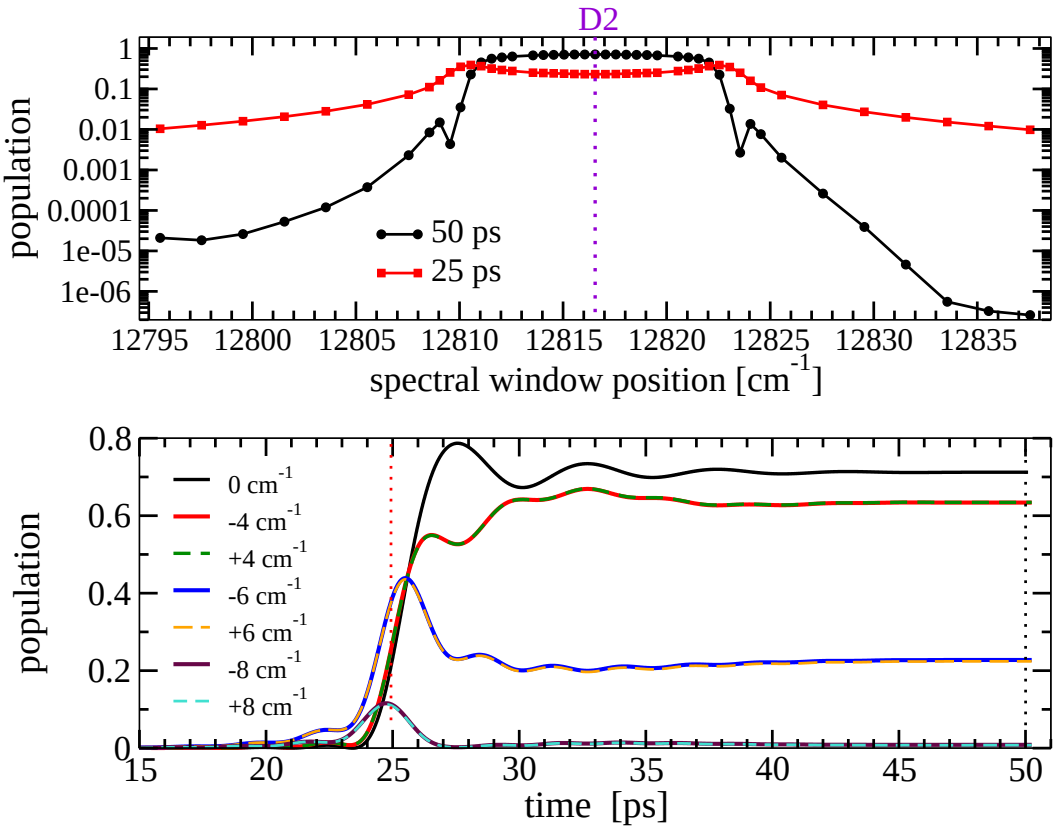

Figure 4.20: Excited state population acquired by employing a narrow spectral window. Upper panel: Population versus spectral window position calculated at the end of propagation (black curve with circles) and at the time instance coinciding the pulse maxima (red curve with squares). D_2 resonance is indicated by the purple dotted line. Lower panel: Excited state population versus time simulated by employing the spectral window when the center of the window coincides with the resonance (black curve), ± 4 cm^{-1}, ± 6 cm^{-1} and ± 8 cm^{-1} detuned with respect to the D_2 resonance. The two time instances corresponding to the pulse maxima and the end of propagation are marked by red and black vertical dotted lines, respectively.

spectral window is on resonance while the second case exhibits a double maximum structure at $\pm$ 6.0 cm^{-1} around the resonance. Moreover, the maximum

excited state population of the first case is about the double of the maximum excited state population of the latter case.

4.3 Conclusion and Outlook

In this chapter, some concepts of coherent control are applied to the ultracold diatomic systems in the frame of photoassociation. One of the first femtosecond photoassociation experiments is simulated. In these experiments and simulations, the broad spectrum of the femtosecond pulses addressing both atomic and molecular transitions is manipulated in a way to prevent the atomic transitions and to promote the molecular transitions. At first step, this is achieved by removing the disturbing frequencies from the pulse spectrum. Then the effect of chirp and the effect of additional phase to the pulse are examined. Excited and ground state population are monitored by carrying out quantum dynamical simulations. The driving ultrafast dipole dynamics are presented. The high peak intensity of the photoassociation pulse causes strong field effects and multi-photon processes. Removal of the disturbing frequencies from the pulse spectrum creates a long pulse tail of the electric field in the time domain and induced dipole interacts with this tail. Due to this interaction, coherent transient oscillation is observed in the molecular population. The period of this oscillation of the molecular population depends on the spectral cut-off position. Population oscillation and its modulations are analyzed by employing filter diagonalization method. Resulting analysis addressed the dominating spectral components and how long these components are effective. Application of an additional phase to the pulse within a certain spectral window, increased the molecular transition rate up to an order of magnitude. However, overall excited state population stayed in 1% of the initial ground state population. This is mainly due to the low initial atomic-pair density close to the inter-nuclear separations where the photoassociation is feasible. Application of external fields to the atomic ensemble may increase the atomic pair density and thus the photoassociation probability. In the next chapter, a new

scheme is proposed in order to increase the initial atomic pair density by manipulating naturally existing shape resonances via application of non-resonant laser fields.

Chapter 5

Controlling Shape Resonances via Non-resonant Laser Fields

In this part of the thesis the prospects for coherently controlling naturally existing *shape resonances* are studied. An efficient control scheme for photoassociation by including shape resonances is proposed.

Reactions at ultracold temperatures can also be profoundly influenced by the resonances when they dominate the quantum dynamics via tunneling. Magnetically induced Feshbach resonances are also used to enhance cold and ultracold molecular formation rate in reaction schemes such as Feshbach optimized photoassociation (FOPA) Pellegrini *et al.* (2008). Magnetic Feshbach resonances provide mechanisms to tune scattering properties of the ultracold collisions. However, using magnetic fields for controlling ultracold reactions has limitations. DC magnetic fields cannot be tuned very fast and magnetic Feshbach resonances have usually very narrow widths. These issues restrict the detection and control of the scattering length in a narrow magnetic field range Li & Krems (2007). Moreover, magnetically induced Feschbach resonances are restricted to the species with non-zero nuclear spin and they are efficient at the even lower the temperatures i.e. nK regime. There exist also electric field induced Feshbach resonances and electric fields can be tuned much faster than magnetic fields Krems (2006). In the case of electrically induced Feshbach resonances, the required electric field strengths are usually very high, i.e. 250-700 kV/cm Marinescu & You (1998) and they are still experimentally unfeasible,

i.e. currently available DC electric fields are about 200 kV/cm Bethlem *et al.* (2000).

In this work, naturally existing shape resonances are exploited in order to increase initial atom pair distribution at the internuclear separations where photoassociation is more effective. A shape resonance which is a metastable state occurs when some part of the wavefunction of partial waves with J>0 trapped by a rotational barrier shows a bound structure in the closer internuclear distances while the rest of it shows a scattering wavefunction behavior as shown in the Fig. 5.1 due to the form of the potential surface Boesten *et al.* (1996, 1997); Londoño *et al.* (2010).

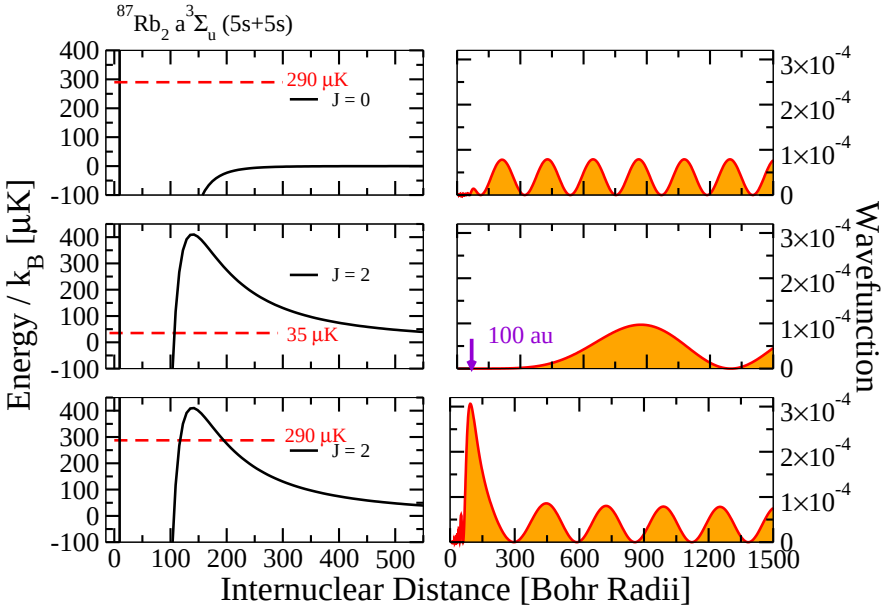

Figure 5.1: Left panel: ^{87}Rb lowest triplet potential with angular momentum J =0 and 2 (black curves). In the upper-most graph of the panel, the scattering state with 290 μK, in the middle graph the scattering state with 35 μK, in the lowest graph scattering state with 290 μK initial energies are indicated with the red dashed lines. A quasi-bound state is formed due to the rotational barrier (J=2) for 290 μK energy only. Right panel: Corresponding scattering functions. In the case of the shape resonance, the wavefunction has an enhanced amplitude in the photoassociation distances, i.e. 100 Bohr radii.

However, most of the shape resonances in alkaline and alkaline earth metals occur typically at temperatures of a few milli-Kelvin. Therefore, the thermal weight of a shape resonance in a much colder MOT or optical trap is quite small Ağanoğlu *et al.* (2011). The position of the shape resonance has to be driven towards the trap temperatures. This idea is shown in Fig. 5.2. External fields can be employed to change the effective rotational barrier Lemeshko & Friedrich (2009) and thus the shape resonance. A non-resonant laser field is employed to manipulate the ground electronic potential surface Ağanoğlu *et al.* (2011).

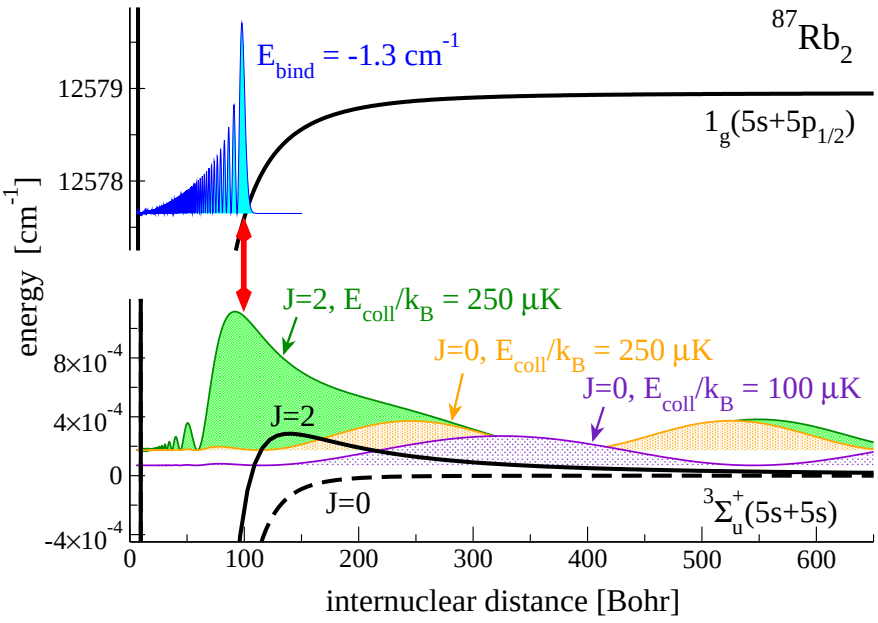

Figure 5.2: ^{87}Rb lowest triplet and the $1_g(5s+5p_{1/2})$ excited state potentials. A Franck-Condon overlap is more favorable between 250 μK initial scattering state (close to the shape resonance) in the presence of the J=2 rotational barrier (green curve) and the excited state bound level with 1.3 cm^{-1} binding energy (blue curve) than the other initial scattering states. However, the thermal weight of the shape resonance is quite small in a typical Rb MOT which is at temperatures about 100 μK.

Low-J shape resonances are universal for diatomic molecules and they are predicted experimentally and theoretically from the scattering properties of the ultracold atoms Gao (1998, 2009); Londoño *et al.* (2010). In this work d-wave shape resonance of an alkali metal ^{87}Rb and g-wave shape resonance of an alkaline earth metal ^{88}Sr are chosen for case study of controlling a shape resonance. Rubidium is widely used in ultracold physics in order to explore the mechanisms of light-matter interaction. Its physical properties such as potential energy curves and polarizability anisotropy are accurately known. ^{88}Sr possesses no hyperfine splitting and $^{88}Sr_2$ is produced by photoassociation Nagel *et al.* (2005). Due to its very small atom-atom interactions Ferrari *et al.* (2006a) this isotope is not very favorable for Bose-Einstein condensates Mickelson *et al.* (2010) but this feature becomes preferable where long coherence times and potential sensitivity is desired when the disturbing collisions are present. This made ^{88}Sr a good candidate for research pursuing precision standards and fundamental physics Ferrari *et al.* (2006b); Zelevinsky *et al.* (2008).

The potential energy curve of the $^{87}Rb_2 a^3\Sigma_u^+(5s + 5s)$ lowest triplet potential energy surface is obtained by connecting ab initio data at short range Park *et al.* (2001) and $\frac{C_6}{R^6} + \frac{C_8}{R^8} + \frac{C_{10}}{R^{10}}$ asymptotic expansion where the C_i expansion coefficients are taken from Ref. Marte *et al.* (2002). Polarizabilities are based on ab initio calculations of Ref. Deiglmayr *et al.* (2008) in the short range and Silberstein's formula in the long range given in Eq. 2.38 and Eq. 2.39. It is observed that both short range and long range polarizabilities fit very well for the inter-nuclear separations larger than 8.5 angstrom as plotted in Fig. 5.3 and the short range polarizabilities are not effective in this study. Using ab initio data for short range and using Silberstein's expansion for polarizabilities gave identical results.

Spectroscopically obtained data is used for $^{88}Sr_2 X^1\Sigma_g^+$ potential energy surface which the analytical fit is also presented in the Ref. Stein *et al.* (2008). The polarizabilities are approximated by using Silberstein's expansion given in Eq. 2.38 and Eq. 2.39 with the atomic polarizabilities taken from Lide (2003).

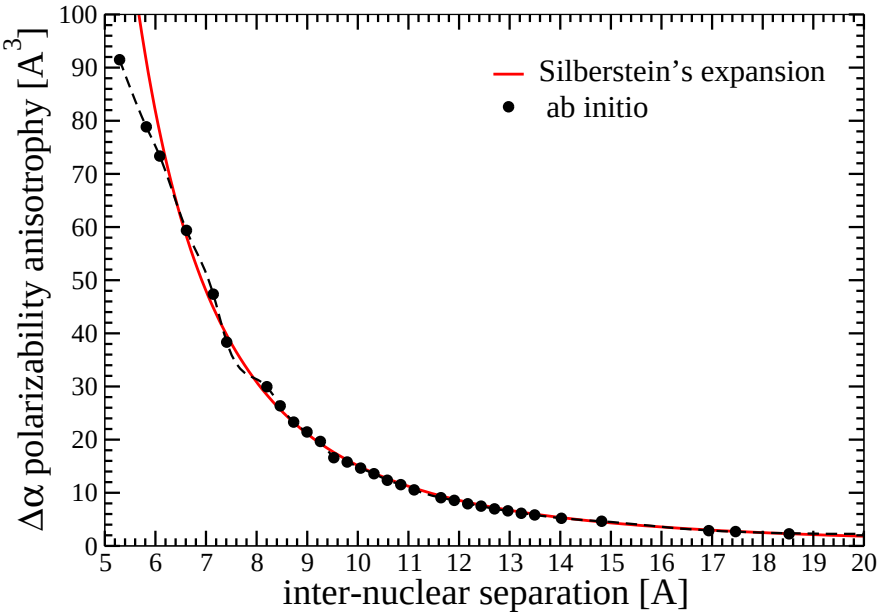

Figure 5.3: Short range polarizability anisotropy of $^{87}Rb_2$. The ab initio data taken from Deiglmayr *et al.* (2008) (black dotted curve) fits very well to the calculated data by using Silberstein's expansion given in Eq. 2.40 (red curve).

5.1 Effect of Non-resonant Laser Field on the Initial Ensemble

The Hamiltonian of an atom pair in its electronic ground state in the presence of a non-resonant laser field can be written as

$$\hat{\mathbf{H}}_2 = \hat{\mathbf{T}}_{\mathbf{R}} + \frac{\hat{\mathbf{J}}^2}{2\mu\hat{\mathbf{R}}^2} + V_g(\hat{\mathbf{R}}) - \frac{2\pi I}{c}[\Delta\alpha(\hat{\mathbf{R}})\cos^2\hat{\theta} + \alpha_\perp(\hat{\mathbf{R}})] \tag{5.1}$$

where the first and second terms denote the vibrational and rotational kinetic energies, respectively, and $V_g(\hat{\mathbf{R}})$ is the field-free ground electronic potential energy surface Ağanoğlu *et al.* (2011). The last term of 5.1 represents the interaction with a non-resonant laser field, with I the laser intensity and $\Delta\alpha(\hat{\mathbf{R}})$ the polarizability anisotropy, given in 2.40 for the far-resonance limit. Derivation of the Hamiltonian given in 5.1 is done by considering laser frequencies far

from any resonance and larger than the inverse of both the pulse duration and the rotational period. According to these justifications rotating wave approximation is applied to the calculations Pershan *et al.* (1966).

Due to the fact that the considered interaction of the non-resonant light with the ultracold atomic ensemble is a second-order type of interaction, Eq. 5.1 possesses I laser intensity and $\cos^2\theta$ instead of E_0 field amplitude and $\cos\theta$. This results with high-field-seeking field dressed eigenstates for the system. It is expected that energy of an eigenstate decreases by increasing the laser intensity as shown in Fig. 5.4.

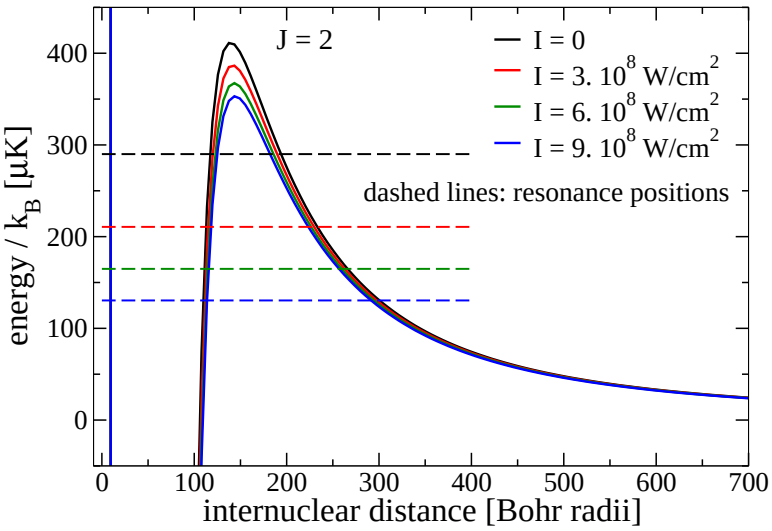

Figure 5.4: Effect of the non-resonant laser light on the $^{87}Rb_2$ a $^3\Sigma_u(5s+5s)$ lowest triplet potential with J = 2 (black curve). The field free d-wave resonance lies at about 290 μK. Application of a non-resonant laser modifies the rotational barrier and thus the resonance position. Field-dressed 1D potential energy curves are plotted for the laser intensities 3 10^8, 6 10^8 and 9 10^8 W/cm^2 with red, green and blue curves, respectively. Increasing the laser intensity, decreases the energy of this resonant state and moves it towards lower temperatures.

5.2 Effective 1D Model

In the field-free case, molecular levels are characterized with their vibrational, rotational and magnetic quantum numbers (v, J, M). Scattering states in the continuum are represented with (n, J, M) translational quantum numbers corresponding a scattering energy E_n. This discretization of the continuum is a result of grid representation of the system as explained in Chapter 3 of this thesis. Radial part (R-dependent) of the problem is treated on a mapped Fourier grid while angular part (θ-dependent) of it is treated by employing Legendre transformation Bačić & Light (1989); Light *et al.* (1985). The help of Dr. R. González-Férez in order to implement the part of the computer code treating the angular degree of freedom is greatfully acknowledged. Since high laser intensities mix more rotational states, more partial waves and consequently more Legendre polynomials are needed to be included to reach the desired convergence of the numerical parameters. It is calculated to be $J_{max} > 11$ for Rubidium and $J_{max} > 13$ for Strontium when the used laser intensities are considered. The calculations for Rubidium in this study are carried out with J_{max} =14 in the adiabatic regime and J_{max} =19 in the non-adiabatic regime while for Strontium with J_{max} =14 in the adiabatic regime.

Direction of the applied laser field defines the symmetry of the system. In this case, azimuthal symmetry about the laser polarization axis keeps the light - matter interaction θ dependent only by averaging out the φ dependence, hybridizing the rotational motion while keeping the magnetic quantum number M unchanged. The field-free degeneracy of the states with a certain J and different M is lifted because of the interaction with the field. The effect of the non-resonant field becomes the largest for the lowest magnetic quantum number, M=0. Due to this fact in the following calculations only the case of M=0 is considered.

In order to search the effect of the non-resonant light on the atomic ensemble, as a first approximation an effective one dimensional model is developed. First model is based on the work of B. Friedrich and M. Lemeshko Lemeshko & Friedrich (2009). The effect of the non-resonant laser field is included into the expectation value of the rotational quantum number J resulting an effective

rotational quantum number J^* which is not necessarily an integer number. J* is a function of the anisotropy polarizability $\Delta\alpha$ and the intensity I Lemeshko & Friedrich (2009). Thus the centrifugal term added to the V_{gs} ground state potential energy surface possesses the effect of the field resulting V_{gs}^{eff}, a modified ground state potential after the non-resonant field is switched off, given by

$$V_{gs}^{eff}(R) = V_{gs}(R) + \frac{<\hat{\mathbf{J}}^2>\hbar^2}{2\mu R^2}. \tag{5.2}$$

Expectation value $<\hat{\mathbf{J}}^2>$ and the rotational constant B are calculated by using the wavefunction of the last bound level since the modified resonance has very close form to it due to its quasi-bound nature. $V(\hat{\mathbf{r}})$ term of the radial Hamiltonian given in Eq. 3.3 is substituted with the obtained V_{gs}^{eff}. Thus by storing the contribution coming from the angular degree of freedom to the R-dependent ground state potential the two dimensional problem is reduced to a one dimensional problem.

Feasibility of the scheme to manipulate the pair density is determined by calculating the lifetime of the quasi-bound state. By adding a purely imaginary optical potential $V_{CAP}(R)$ of the form

$$V_{CAP}(R) = \begin{cases} 0 & \text{if } R < R_0 \\ -i\eta R^2 & \text{if } R_0 < R < R_{max} \\ 0 & \text{if } R > R_{max} \end{cases} \tag{5.3}$$

to the ground state $V_{gs}^{eff}(R)$, a complex Hamiltonian is obtained. Here η is the imaginary potential strength, R_0 is the beginning and R_{max} is the end of the optical potential Riss & Meyer (1993). The lifetime is given by the inverse of the imaginary part of the eigenvalue corresponding to the resonance. The resonance is identified by its isolated position of energy and lifetime among all other scattering states as plotted in Fig. 5.5. It is converged with respect to the optical potential parameters and distinguished in the complex energy plane Riss & Meyer (1993).

As the resonance moves towards lower temperatures, it resembles more to a bound level which has lifetime close to infinity and determination of the convergence conditions in order to calculate lifetime becomes challenging. Therefore, in addition to explained complex absorbing potential (CAP) method, a

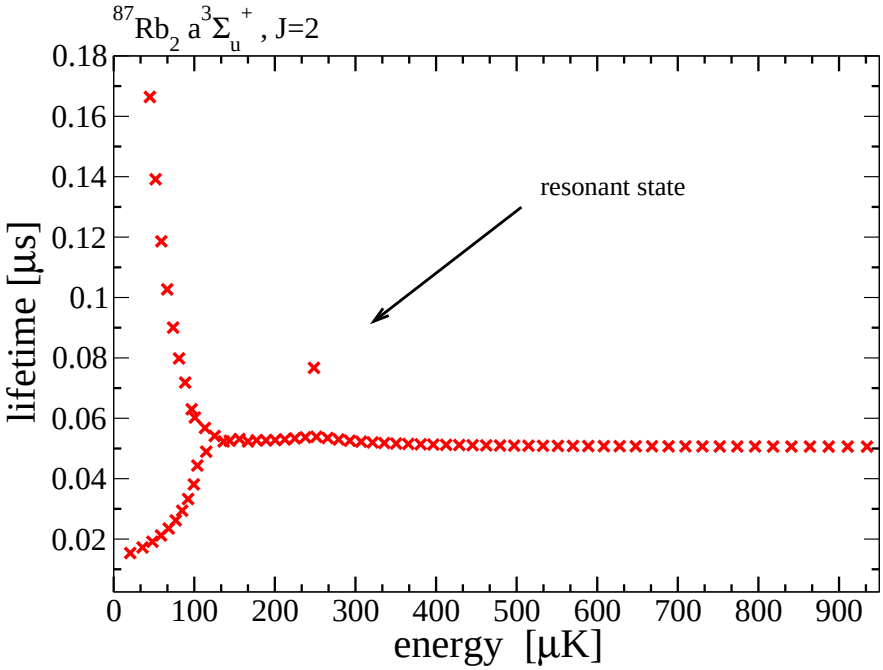

Figure 5.5: Shape resonance of J = 2 state on the $^{87}Rb_2$ a $^3\Sigma_u(5s+5s)$ lowest triplet potential surface is identified on the complex energy plane. The isolated point around energy = 250 μK corresponds to the resonant state. The optical potential parameters are chosen to be R_{max} = 11308 au, R_0= 508 au and η = 5.0 10^{-10} for this particular calculation. The position of the resonant state does not change by changing these parameters within the convergent limit.

second method is employed in order to calculate lifetime of the resonance as well. In this second method, rotational constants $B_n =< n|\frac{\hbar^2}{2\mu\hat{\mathbf{R}}^2}|n >$ of normalized continuum states n are plotted versus energy of the states E_n and fitted to a Lorentzian. The lifetime τ_r of the resonance is related to the width Γ_r of the resonance as $\tau_r = \hbar/\Gamma_r$ Londoño *et al.* (2010). This method has limitations as the resonance position is shifted towards lower energy by the non-resonant field since fewer box-discretized continuum states contribute to the peak such that measurement of the width of the Lorentzian becomes more difficult.

Comparisons of the lifetimes resulting from the full 2D treatment of the sys-

tem and the effective 1D modelling showed the inadequacy of the 1D model even at relatively low laser intensities. Following this observation, the perpendicular component of the polarizability is added to the 1D reduced Hamiltonian and the model is based on the previous work of P. Schmelcher and R. González-Férez González-Férez & Schmelcher (2009). By diagonalizing the angular part of the Hamiltonian given in Eq. 5.1 for each coordinate grid point, eigenvalues $E_J(R; I)$ are obtained. E_J in Eq. 5.4 corresponds to the contribution of the rotational part of the Hamiltonian under the influence of the non-resonant laser field of intensity I Ağanoğlu *et al.* (2011).

$$\Big[\frac{\hat{\mathbf{J}}^2}{2\mu\hat{\mathbf{R}}^2} - \frac{2\pi I}{c}(\Delta\alpha(R)\cos^2\hat{\theta} + \alpha_\perp(R))\Big]\Phi_J(\theta; R, I) = E_J(R, I)\Phi_J(\theta; R, I) \quad (5.4)$$

The effective wavefunctions can be written as a linear combination of these angular wavefunctions over rotational states,

$$\Psi_{n,J}(R, \theta; I) = \sum_{J'} \psi_{nJ'}(R; I)\Phi_{J'}(\theta; R, I). \quad (5.5)$$

By adding the contribution of the angular part E_J to the bare ground state potential energy surface V_{gs} the effective 1D potential energy curves are obtained,

$$V_{gs}^{eff}(\hat{\mathbf{R}}; I) = V_{gs}(\hat{\mathbf{R}}) + E_J(\hat{\mathbf{R}}; I). \quad (5.6)$$

The wavefunctions of the Eq. 5.5 are used in the Hamiltonian given in Eq. 5.1.

Integration over the angular degree of freedom as

$$\Big[\hat{\mathbf{T}}_\mathbf{R} + V_g(\hat{\mathbf{R}}) + E_J(\hat{\mathbf{R}}; I) - E\Big]\psi_{n,J}(R; I) = \\ -\sum_{J'}\psi_{n,J'}(R; I)\int_0^\pi \Phi_J^*(\theta; R, I)T_R\Phi_{J'}(\theta; R, I)\sin\theta d\theta \quad (5.7)$$

results zero on the right hand side of Eq. 5.7. Thus Schrödinger equation in the new effective 1D model follows

$$\Big[\hat{\mathbf{T}}_\mathbf{R} + V_g(\hat{\mathbf{R}}) + E_J(\hat{\mathbf{R}}; I)\Big]\psi_{n,J}(R; I) = E_n\psi_{n,J}(R; I). \quad (5.8)$$

The lifetime and resonance energies calculated by using two different 1D models described above and full 2D model are compared in Fig. 5.6. It is observed that the 1D model with V_{gs}^{eff} obtained by following the steps between 5.4 - 5.6 gives relatively more consistent results with full 2D model than the 1D model where only an effective rotational quantum number J* is included to the Hamiltonian.

In the adiabatic approximation the effect of the non-resonant laser is only reflected by the modified barrier height. The coupling between rotational and vibrational motion is neglected. Effective 1D models are derived in the energy scale where the adiabatic approximation is valid; rotational wavefunctions depend parametrically on the radial coordinate variable. Increasing the applied non-resonant field intensity leads deviation from the adiabatic regime and 1D models cannot cover coupling between rotational states of different vibrational bands as shown in Fig. 5.6. As the laser intensity increases the position of the resonance is driven towards lower energies. It is found that laser intensities smaller than 10^9 W/cm^2 are sufficient to bring resonance close to the 100μK; typical rubidium MOT temperatures. The shift in the resonance energy with respect to the field-free resonance position is underestimated by the effective 1D model for the intensities larger than 4.0 10^8 W/cm^2.

5.3 Effect of the Rotational Mixing

The effect of the coupling between rotational and vibrational motion is searched by using full 2D description of the system. The contribution of the partial waves (rotational weights) c_J^I to the resonance for each intensity I is calculated by projecting the wavefunction of the resonance Ψ_{res}^I onto the field-free eigenstates φ_{nJ} Ağanoğlu *et al.* (2011); Lemeshko & Friedrich (2010),

$$c_J^I = \sum_n \int dR \int d\cos\theta \Psi_{res}^{I*}(R,\theta)\varphi_{nJ}(R,\theta). \tag{5.9}$$

$^{87}Rb_2$ triplet lowest potential has a d-wave resonance (J=2) at about 300 μK in the field-free case. As the non-resonant laser is applied to the system, the wavefunction of the resonance becomes a superposition of different rotational

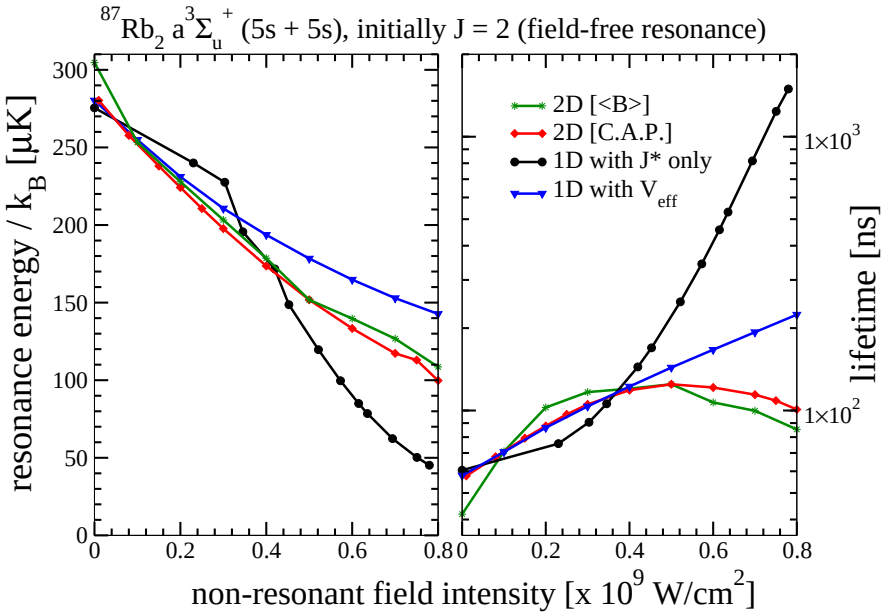

Figure 5.6: Energy (left panel) and lifetime (right panel) of the shape resonance on the $^{87}Rb_2$ a $^3\Sigma_u^+(5s+5s)$ lowest triplet potential surface as a function of applied non-resonant laser field intensity is plotted. The 1D model calculations with V_{gs}^{eff} of Eq. 5.6 (blue curve) are better matched with the 2D calculations than the results obtained with V_{gs}^{eff} of Eq. 5.2 (black curve). Position and the lifetime of the resonance is calculated in 2D by employing CAP method (red curve) and by determining the peak width and peak position of the rotational constants (green curve). CAP method is employed for all 1D calculations. Increasing the laser intensity increases the difference between resonance energies obtained in 1D and 2D. 1D models becomes inadequate for calculating the resonance lifetime starting from the intensities higher than 4.0 10^8 W/cm^2. Time scales of rotational and vibrational motion start becoming comparable.

states. Increasing the laser intensity mixes more rotational states; the state with largest weight, as plotted in Fig. 5.7 is the J=0 state which has purely scattering character. As seen in Fig. 5.6, for the intensities larger than 5.0 10^8 W/cm^2 a turnover in the lifetime is observed. The contribution of J=0 states becomes larger than 30% for the corresponding intensities. The higher J states do not contribute significantly[1] to the resonance. Therefore, the resonance starts loosing its quasi-bound character.

In order to test the universality of this control scheme, effect of the non-resonant laser on a different element, ^{88}Sr is studied, too. It is observed the g-wave resonance can be controlled in a similar fashion of rubidium. The g-wave resonance of $^{88}Sr_2 X^1\Sigma_g^+$ is calculated to be 1750 μK. Application of a non-resonant laser and increasing the intensity moved the resonance position towards lower energies. Since this shape resonance of strontium lies at higher energies than the one of rubidium the required non-resonant laser intensities to bring it to typical strontium MOT temperatures is higher. ^{88}Sr has low atomic polarizability and low interaction strength. Moreover, the larger rotational constant of strontium than the one of rubidium necessitates higher laser intensities to fetch the same effect. When a typical strontium MOT temperature of 20 μK is considered Zelevinsky *et al.* (2006), a non-resonant field intensity about 5.0 10^9 W/cm^2 is required to bring the resonance towards corresponding energies. As observed in the case of rubidium, 1D model derived by using adiabatic approximation underestimates the shift in energy with high non-resonant field intensities. The deviation between the resonance energies calculated in 1D and 2D becomes large for higher intensities than 2.0 10^9 W/cm^2 as plotted in Fig. 5.8.

$^{88}Sr_2 X^1\Sigma_g^+$ possesses several shape resonances. Other resonances, an l-wave resonance corresponding to J=8 rotational quantum number is found around 5018μK and a q-wave resonance corresponding to J=12 rotational quantum number is found around 3042μK. By increasing the non-resonant field intensity, the position of these resonances move towards lower temperatures, too. It is observed that the resonance with highest rotational quantum number moves

[1] Please note the different scales of c_J^I for different J's.

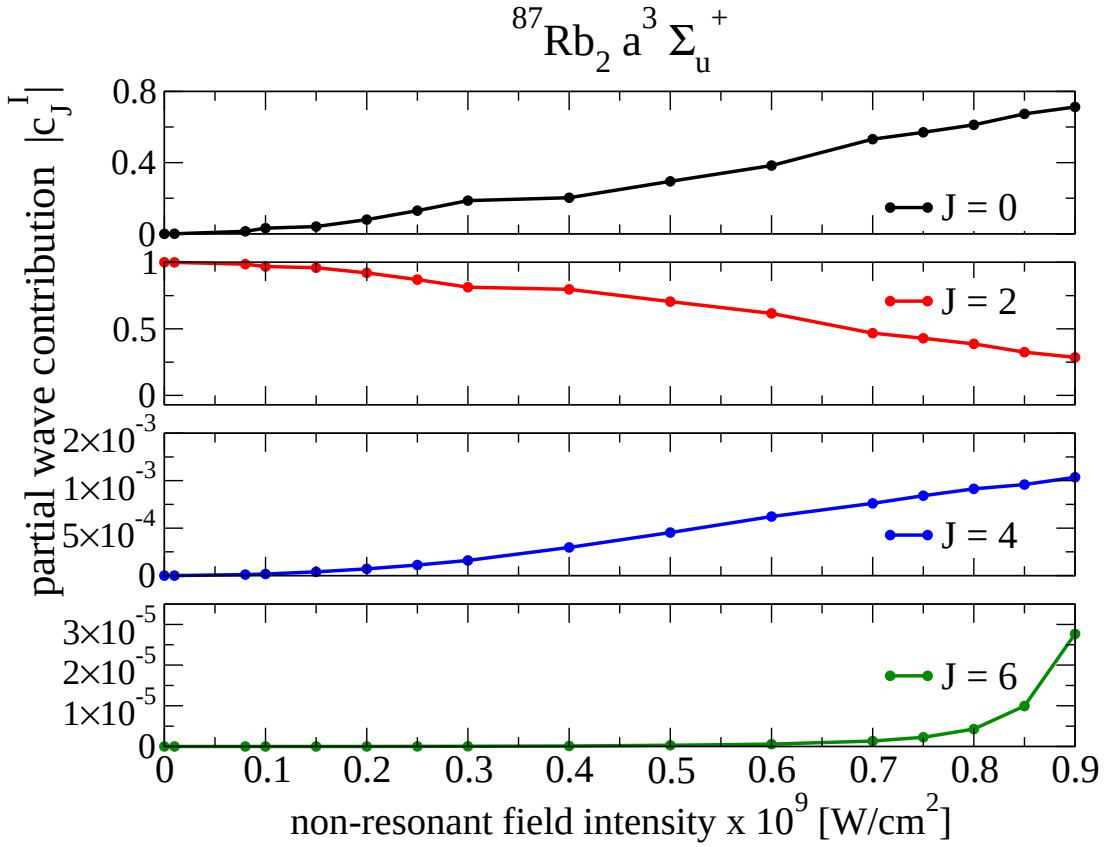

Figure 5.7: Contribution from the field-free rotational states with the lowest four J quantum number to the resonance with respect to applied non-resonant field intensity. Since the coupling mixes only partial waves of the same parity, only the states with even J's have non-zero contribution.

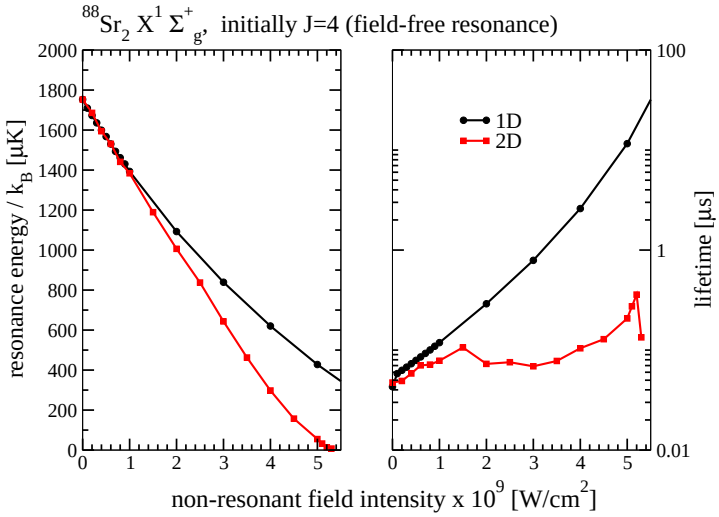

Figure 5.8: Energy (left panel) and lifetime (right panel) of the shape resonance on the $^{88}Sr_2X^1\Sigma_g^+$ potential surface as a function of applied non-resonant laser field intensity is plotted. In 1D model resonance position and lifetime is determined by employing CAP method while in 2D model they are calculated by determining the peak width and peak position of the rotational constants.

fastest in the presence of the non-resonant laser field and within the range of considered laser intensities, the q-wave resonance disappears.

The l-wave resonance is narrower and its lifetime is longer than the g-wave resonance. As explained in Section 5.2, a shape resonance can be distinguished by searching the expectation value of the rotational constant $< B >$ versus the energy of the rovibrational states Londoño *et al.* (2010). The expectation value of the rotational constant is plotted in Fig. 5.9 as a function of energy and the emerging resonances are indicated by the corresponding letter. The position of the l-wave resonance cathes the g-wave resonance when the non-resonant field intensity reaches 6.0 10^8 W/cm^2 first and then when it reaches 3.0 10^9 W/cm^2. The increase of laser intensity leads to strong coupling of rotational and vibrational motion and causes an avoided crossing González-Férez & Schmelcher (2005b). As in the case of rubidium d-wave shape resonance, increasing non-

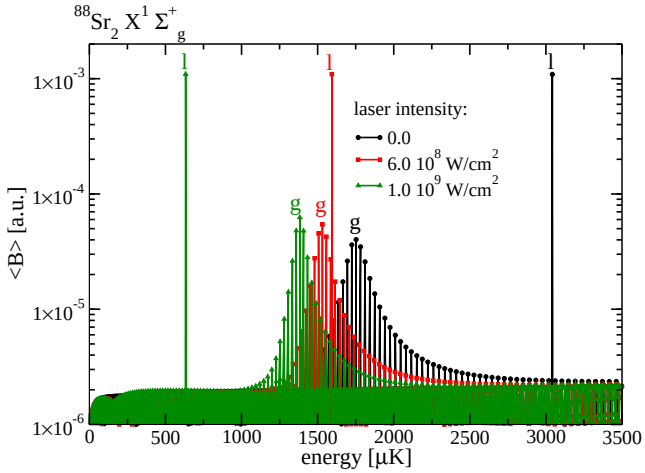

Figure 5.9: The expectation value of the rotational constant as a function of energy. The position of the resonance varies with respect to applied non-resonant laser field intensities. The black, red and green curves represent the field-free case and the cases when laser fields with intensities of I = 6.0 10^8 W/cm^2 and I = 1.0 10^9 W/cm^2 are applied, respectively. The letters "*g*" and "*l*" stand for the labelling of g-wave and l-wave resonances.

resonant field intensity first increases the lifetime of the resonance but then decreases due to strong mixing of purely scattering state lifetime of the resonance. Since the l-wave resonance in strontium moves quicker to lower energies than the g-wave resonance, both resonances come close to each other for intensities around 3.0 10^9 W/cm^2, when an avoided crossing occurs. As a consequence, the lifetime of the g-wave resonance starts increasing again around this intensity, as indicated in the right panel of Fig. 5.8. Contribution from the rotational states to the strontium initial J = 4 resonance is plotted in Fig. 5.10. As the non-resonant laser intensity increases a substantial amount of first J = 2 and then J = 0 is mixed in to the field-free J = 4 state. Due to the coupling of l-wave and the k-wave resonances, a rapid rise in the weight of J=8 is observed for the intensity above 3.0 10^9 W/cm^2.

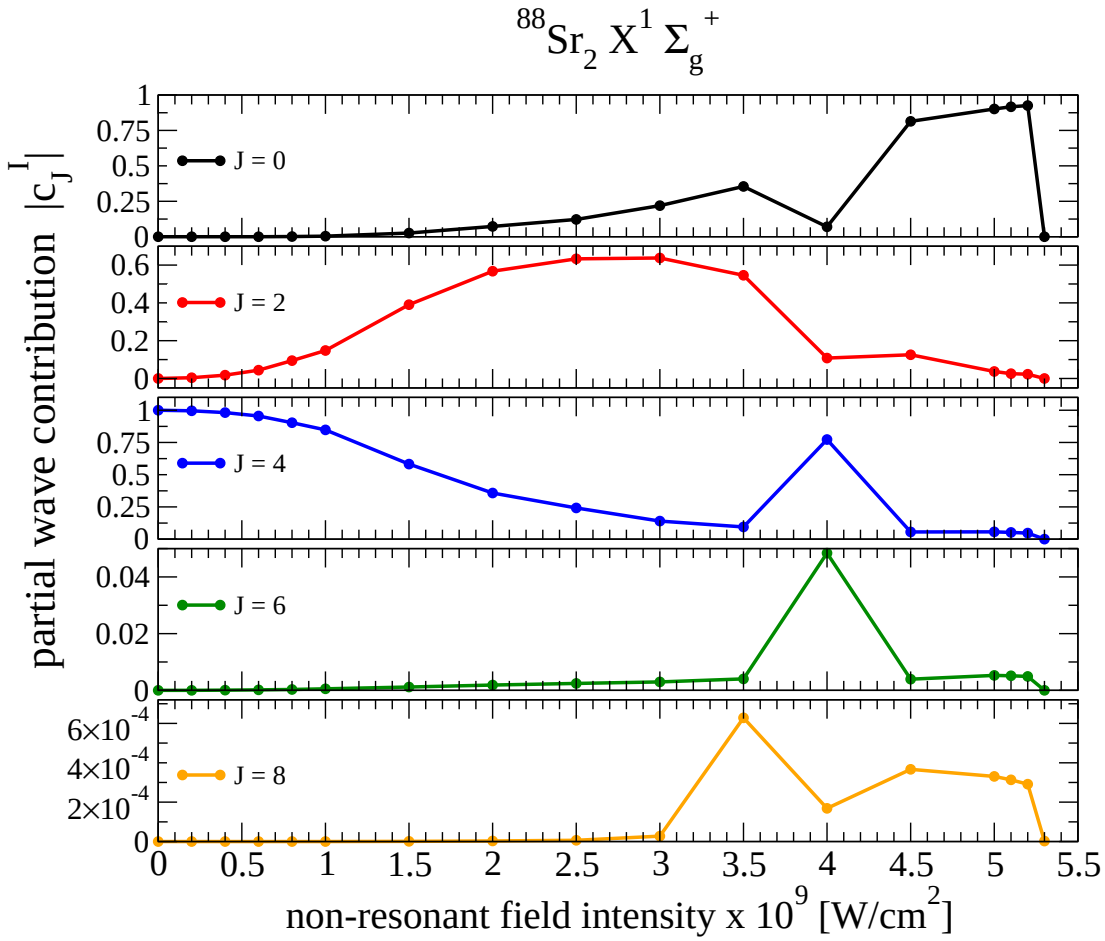

Figure 5.10: Contribution from the field-free rotational states with the lowest five J quantum number to the resonance with respect to applied non-resonant field intensity. Since the coupling mixes only partial waves of the same parity, only the states with even J's have non-zero contribution.

5.4 Generating Non-adiabatic Dynamics by Using Short Pulses

In the previous sections, effect of the non-resonant laser on the system is studied in the adiabatic time frame. If the interaction of the system with the laser field is adiabatic, the dynamics are slow in a way to allow the system can evolve adiabatically and yield to its initial status. This process is a reversible process. On the otherhand, if the interaction is non-adiabatic, the states of the system cannot turn back to their initial status in the time scale of the process. Generation of non-adiabatic conditions is studied by many researchers in different contexts Averbukh & Perelman (1989); Mitrić *et al.* (2006); Wohlgemuth *et al.* (2011). The created wavepackets are coherent superpositions of a finite number of quantum states and the fast laser switch-off leaves the system permanently into a state which is different than the initial state. The decisive parameter of this case in order to classify the type of the interaction as adiabatic or non-adiabatic is the τ_{rot} rotational period in the case of interest Lemeshko & Friedrich (2010); Owschimikow *et al.* (2009). If the pulse duration is much longer(shorter) than the rotational period the interaction is categorized as an adiabatic(non-adiabatic) interaction.

$^{87}Rb_2$ $a^3\Sigma_u^+$ triplet lowest potential is used for the non-adiabatic dynamics case study. The rotational constant B is calculated as

$$< B >_{v,<J^2>} = < v, < J^2 > |\frac{\hbar^2}{2\mu\hat{\mathbf{R}}^2}|v, < J^2 >> \tag{5.10}$$

where μ is the reduced mass of $^{87}Rb_2$ and $|v, < J^2 >>$ stands for the rovibrational state with v vibrational and J angular momentum quantum numbers. The rotational period is inversely related with the rotational constant as $\tau_{rot} = \pi\hbar/B$ and calculated to be 82 ns by using the last bound level. The non-adiabatic pulses with fwhm of 800 ps, 1500 ps and 5000 ps are employed to simulate dynamics of the system.

The largest enhancement in the short range pair-density for the 105μK energetic scattering state with J=0 is calculated by taking the ratio of the area

below the field-dressed wavefunction $\varphi^*(R;\theta)$ and the field-free wavefunction $\varphi^0(R;\theta)$ up to inter-nuclear seperation of R_{max} = 116 bohr as $\int_0^{R_{max}} dR \int \varphi^*(R;\theta) d\cos\theta / \int_0^{R_{max}} dR \int \varphi^0(R;\theta) d\cos\theta$. This state energetically corresponds to the temperature of the MOT and the photoassociation is optimally favorable in the spatial region where the outermost maximum of this initial scattering wavefunction lies. The propagation times are chosen to be more than 5 **x** fwhm of the employed pulses. In order to represent the rotational grid 20 angular grid points corresponding to J_{max} = 19 included. As the fwhm increases oscillation is observed in the maximum enhancement versus laser intensity curve for large laser intensities, cf. green curve in the upper panel of Fig. 5.11. The interaction with the weak laser pulses, i.e. intensities below 1.0 10^9 W/cm^2, results very similar enhancement ratios in the outer most maxima of the wavefunctions independent from the pulse duration. In the lower panel of Fig. 5.11 the rotational contributions $|c_J^I|$ of lowest four even rotational states at the end of propagation are plotted. Increasing the non-resonant laser intensity mixes rotational states in a similar fashion observed in the adiabatic scheme, cf. Fig. 5.7.

Time-dependent behavior of the calculated enhancement and the rotational contributions $|c_J^I|$[t] are exemplified with non-adiabatic pulses of 5000 ps fwhm for three different maximum non-resonant field intensities and plotted in Fig. 5.12. Following the interaction with the non-resonant laser, the wavepacket oscillates in the potential energy surface. When it is reflected from the effective rotational barrier, e.g. Eq. 5.2, the amplification in the outermost maximum of the wavepacket leads to enhancement increase. The period of this behavior depends on the pulse duration and the amplitude depends on the applied laser intensity. This reinforces the interpretation of the oscillations in the enhancement ratio as due to the oscillations of the wavepacket in the potential well. For low laser intensities, this oscillation averages out while for higher laser intensities it does not. This can be monitored by comparing the purple dashed line in the upper panel of Fig. 5.12 which indicates the initial status of the enhancement ratio and the oscillation in the enhancement ratio obtained by employing pulses with different intensities. If the laser intensity is high, the oscillation also decays as observed during the propagation with a

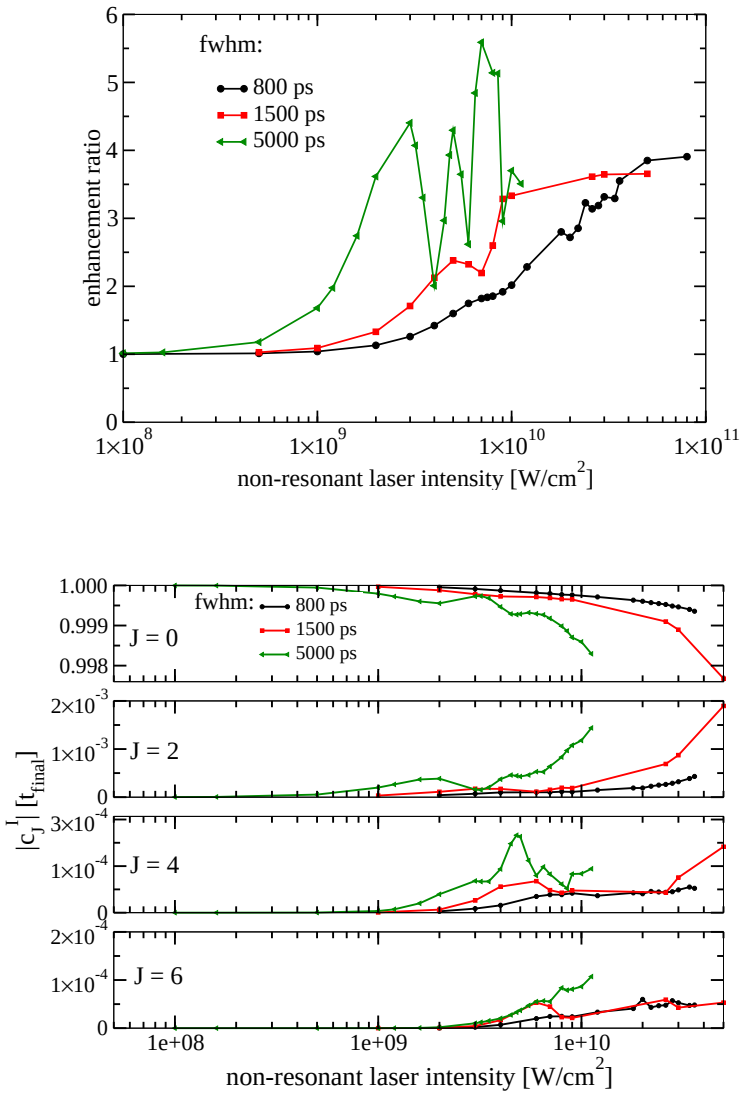

Figure 5.11: Upper panel: The maximum enhancement in the outermost maximum of the 105μK energetic scattering state vs. pulse intensity. The non-adiabatic dynamics are studied by employing pulses with fwhm of 800 ps (black curve), 1500 ps (red curve) and 5000 ps (green curve). The propagation times are chosen to be 5 **x** fwhm of the employed pulse. A rotational grid of 20 angular grid points is employed in order to capture the interaction dynamics with the strong field. Lower panel: Contribution of the rotational states with J=0, J=2, J=4 and J=6 at the end of propagation versus applied non-resonant field intensity obtained by using pulses with fwhm of 800 ps (black curve), 1500 ps (red curve) and 5000 ps (green curve).

non-resonant pulse of I = 1.12 10^{10} W/cm^2 maximum intensity (green curve of the same figure). For the lower intensities, the created wavepacket is composed of essentially few rotational levels. Since these few levels are expected to have similar rotational periods, then the wavepacket goes back and forth in the potential in a coherent way, i.e. without spreading, during the considered propagation times. However, for the larger intensities, more and more rotational levels are populated. Then it becomes difficult for the wavepacket to stay focused, and it spreads inside the potential more with time. This results in the oscillation being of smaller amplitude and decaying to zero. Another argumentation for this mechanism involves tunneling effects. For very high intensities, the created wavepacket at the effective rotational barrier is quite energetic and it has high amplitude. In this intensity regime lowering the rotational barrier drastically can make it possible that some population leaks out by the tunnel effect.

The time-dependent rotational contributions $|c_J^I|$[t] evolve during the time as plotted in the lower panel of Fig. 5.12. The normalized pulse is indicated by the purple dotted line. Oscillation in the $|c_J^I|$[t] curve is observed when the pulse is strong but after the pulse is over, the field-free states are no longer coupled thus the $|c_J^I|$ coefficients reach a constant value. The change in the energy of the system is observed as a function of time and plotted in Fig. 5.13. The total energy of the system $< \hat{\mathbf{H}}_2 >$ is initially equal to the energy of the initial state, i.e. 105μK. Once the laser pulse is over, total energy reaches a value of initial energy plus the energy transmitted by the pulse as shown in the uppermost panel of Fig. 5.13. The potential energy of the system $< V_g(\hat{\mathbf{R}}) >$, the vibrational kinetic energy $< \hat{\mathbf{T}}_{\mathbf{R}} >$ of the system and the rotational energy of the system $< \dfrac{\hat{\mathbf{J}}^2}{2\mu\hat{\mathbf{R}}^2} >$ are displayed in the second, third and in the lowest panel of the same figure, respectively.

The vibrational energy of the system is modified when the pulse is effective and oscillates with the same period of the enhancement ratio after the pulse is over. When laser pulse has 1.2 10^9 W/cm^2 intensity, only few rotational states are involved to the dynamics. The energy difference between rotational states with even J's can be estimated to be 2 B (4J +6) Herzberg (1989) within the

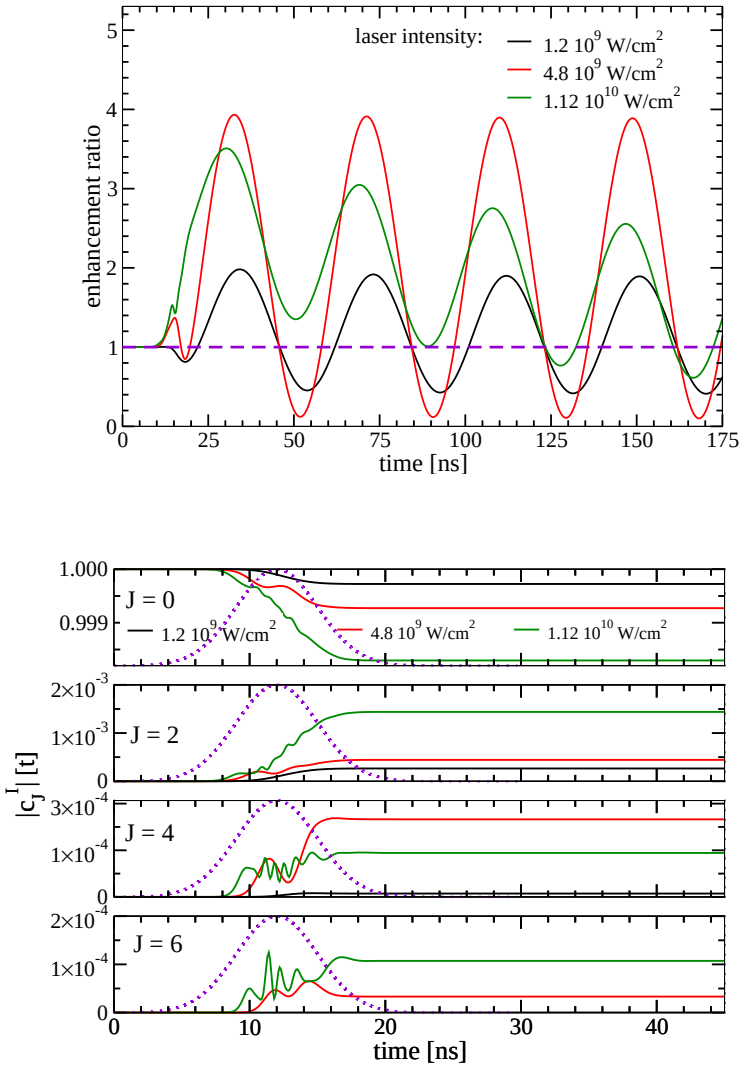

Figure 5.12: Upper panel: Time-dependent enhancement obtained by using pulses of 5000 ps fwhm with maximum non-resonant laser intensities of 1.2 10^9 W/cm^2 (black curve), 4.8 10^9 W/cm^2 (red curve) and 1.12 10^{10} W/cm^2 (green curve). The enhancement varies periodically during the propagation and the period of this behavior is around 40 ns for each non-resonant laser intensity. Lower panel: Corresponding time-dependent rotational contributions c_J^I[t] for lowest four even rotational states with respect the same color coding. The temporal dependence of the pulse is indicated by the purple dotted curve. Please note the c_J^I[t] has a narrow scale.

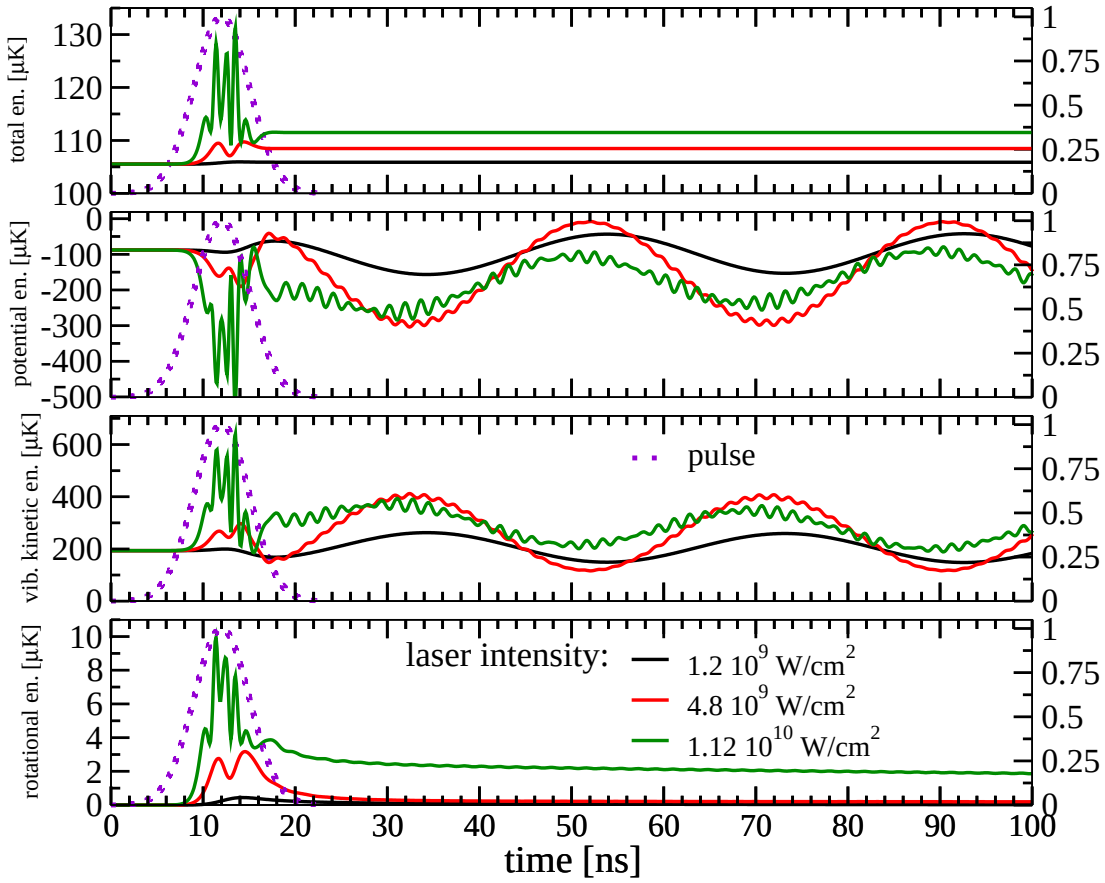

Figure 5.13: Energy of the system when non-resonant pulses of 5000 ps fwhm are employed with the laser intensities of 1.2 10^9 W/cm^2 (black curve), 4.8 10^9 W/cm^2 (red curve) and 1.12 10^{10} W/cm^2 (green curve). The duration of pulse is indicated by the purple dotted curve. Uppermost panel: Total energy of the system. Second panel: Potential energy of the system. Third panel: Vibrational kinetic energy of the system. Lowest panel: Rotational energy of the system. It is modulated when the pulse is on and decays slowly after the pulse is switched off.

rigid-rotor approximation. From the Fig. 5.12 it can be seen that for low intensity mostly states with J=0 and J=2 are populated. For higher non-resonant pulse intensities, more rotational states are populated and thus a beating pattern on the main oscillation of vibrational and potential energy is observed. The period of the oscillation is obtained by doing the Fourier transformation. When the laser pulses of intensities of 1.2 10^9 W/cm^2, 4.8 10^9 W/cm^2 and 1.12 10^{10} W/cm^2 are employed, the period of the main vibrational energy oscillation for each intensity is determined to be 42.14 ns, 41.79 ns and 38.35 ns, respectively. For I = 4.8 10^9 W/cm^2 (red curve), modulations with periods of 1.58 ns, 1.64 ns and 1.86 ns and for I = 1.12 10^{10} W/cm^2 (green curve), modulations with periods of 1.58 ns, 1.88 ns and 2.78 ns are observed.

The rotational energy transmitted to the system is modified when the pulse is effective, too. After the pulse is over it reaches a certain value depending on the employed non-resonant pulse intensity and decays out smoothly. The energy transmitted to the system via rotations can only reach to the order of 10 μK, c.f. green curve of the lowest panel in Fig. 5.13. This energy is quite low compared to the energy transmitted via vibrations. However, the vibrational energy, i.e. $< V_g(\hat{\mathbf{R}}) > + < \hat{\mathbf{T}}_{\mathbf{R}} >$ oscillates between the potential and vibrational kinetic energies during the propagation, c.f. the second and the third panel of Fig. 5.13. Therefore, qualitatively the increase in the total energy of the system stays in the same order of the rotational energy increase.

5.5 Envisioned Scheme for Photoassociation: Pair Density Enhancement by Moving the Resonance

The photoassociation efficiency is limited by the low pair density at large internuclear separation of atoms around Condon point where the photoassociation laser induces a resonant transition from the initial colliding atom pair to a weakly bound level of the electronically excited state potential of the molecule as shown in Fig. 4.2. For alkali and alkaline earth metals typical photoassociation distances vary between 40 to 200 bohrs depending on the chosen initial ground state and the final electronically excited state. Photoassociation of

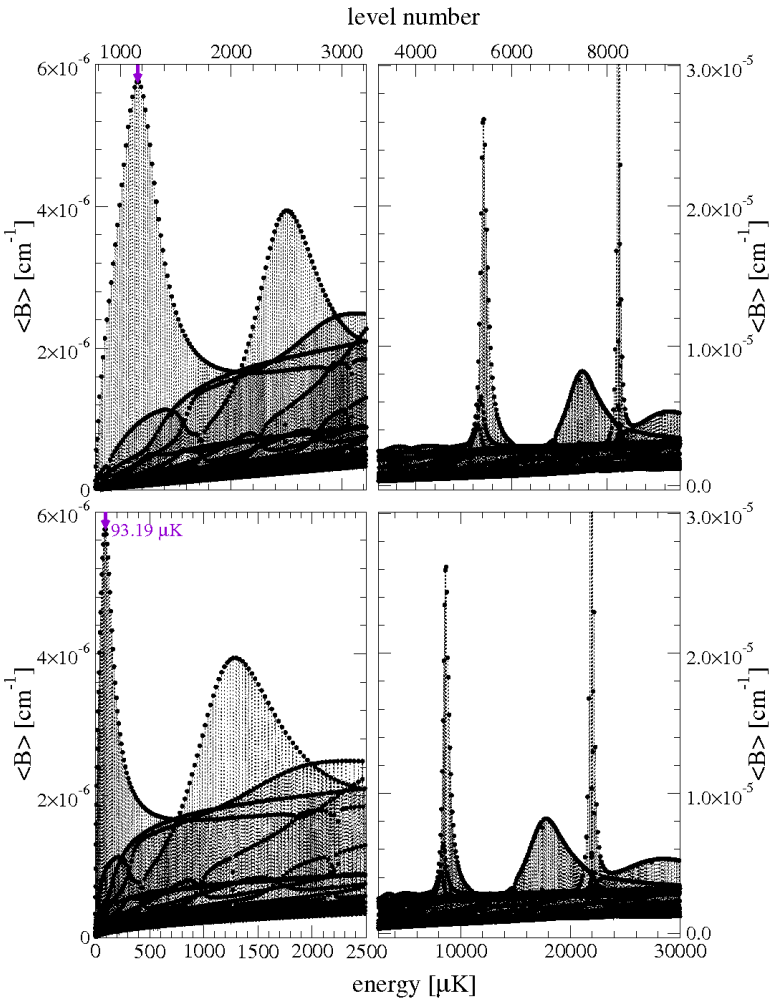

Figure 5.14: Rotational constant $< B >$ versus energy obtained after the pulse of 5000 ps width and 1.2 10^9 W/cm^2 intensity is over. In the upper panels the rotational constant is shown with respect to the rovibrational state number and in the lower panels the rotational constant is plotted as a function of the energy. Left panels focuses on the lower energy regions and the right panels focuses on the high energy regions. The first observed quasi-bound state and its energy is indicated by the purple arrow.

ultracold atoms is compromised between large scattering amplitude at large internuclear separations and high binding energies at short internuclear separations. Colliding atom pairs around the Condon point can be efficiently transform into *ground* state molecules in a pump-dump scheme, by using pulses in the nano-Joule energy scale Koch *et al.* (2006c). Even in this scheme the number of created molecules does not exceed 1 to 10 per pulse depending on the initial atomic density of the MOT Koch *et al.* (2006a).

A new scheme is proposed to increase the number of photoassociated molecules by controlling a shape resonance to increase the initial atomic pair density close to the Condon point. A shape resonance shows a quasi-bound structure due to the trapping of atom pair inside the rotational barrier as indicated in the lowest panel of Fig. 5.1. If this happens at internuclear separations where photoassociation is feasible, large atom pair density boosts photoassociation probability. The photoassociation laser pulse can easily photoassociate all atom pairs in the Franck-Condon window Koch *et al.* (2006a,b) so an increase of the pair density in the Franck-Condon window readily translates into an improved photoassociation probability. However, the natural shape resonances of alkali and alkaline earth metals typically occur at higher temperatures than MOT temperatures. This leads to low contribution to the thermal weight $e^{-E_{nJ}/k_B T_{MOT}}$. In this proposed scheme, application of a non-resonant laser shifts the resonance to energies closer to the trap temperature, so that the initial distribution of atom pairs has a larger overlap with the excited state of interest. In this scheme the non-resonant laser is switched on very slowly compared to the rotational period of the atom pairs. The thermal cloud of atoms follows the field of the non-resonant laser *adiabatically*. The field-free eigenstates are thus transformed into field-dressed states resulting from the Hamiltonian given in Eq. 5.1. This operation modifies the density matrix. In the second step a resonant pulse can be switched on to transfer prepared initial atom pairs to the bound levels. The enhancement in the number of molecules by using this scheme is calculated by taking the ratio of the field-dressed to the field-free thermal pair densities and plotted in Fig. 5.15. It is observed that application of the non-resonant laser increases the pair density at the inter-nuclear separations where the photoassociation is favorable. Bringing the resonance close to the MOT

temperature increases the enhancement since in this way the thermal weight of the resonant state is larger. This enhancement mechanism can be also interpreted with different words: At lower temperatures the thermal distribution becomes narrower. Therefore, when the position of the resonance coincides with T_{MOT}, the increase in the enhancement is much larger, the resonance is sharper.

By applying I = 0.9 10^9 W/cm^2 non-resonant laser intensity, the resonance could be controlled down to 150 μK on $^{87}Rb_2$ a $^3\Sigma_u$(5s+5s) lowest triplet potential energy surface. It is expected to obtain the maximum enhancement with these parameters. However, the enhancements at 100 and 50 μK trap temperatures are larger than the enhancement at 150 μK. Because the initial field-free pair density at 150 μK has been already effected from the presence of the shape resonance while this effect is weaker if the trap temperatures are 100 or 50 μK. Thus for 150 μK, the ρ_0 is already larger then the ρ_0s of the trap temperatures 100 or 50 μK. This decreases the enhancement ratio ρ_I / ρ_0 at 150 μK with respect to the lower trap temperatures. Pair densities at the trap temperatures 300, 150, 100 and 50 μK are plotted in Fig. 5.16 for the field-free case, with the non-resonant field intensities I = 0.5 10^9 and I = 0.9 10^9 W/cm^2. At the distances shorter than the last maximum, the pair density shows enhancement with respect to the applied field, too. However, at these very short inter-nuclear separations the wavefunctions have very strong oscillations and they cannot be directly associated with the molecular transitions when a photoassociation pulse is applied onto this pair distribution. The largest effect of the pair distribution enhancement on the photoassociation is expected to be at inter-nuclear separations close to the outermost maximum of the pair distribution which is determined to be 85 bohr for $^{87}Rb_2$ a $^3\Sigma_u$(5s+5s) lowest triplet potential.

Photoassociation of ultracold atoms with a non-resonant laser field enhancement regards two time scales: Time scale of the non-resonant control laser and time scale of the photoassociation pulse. The time scale of the control laser is determined by the adiabaticity requirement with respect to the rotational motion and it should be slower than the rotational time scale. The time scale of the photoassociation pulse is determined by the vibrational levels to populate

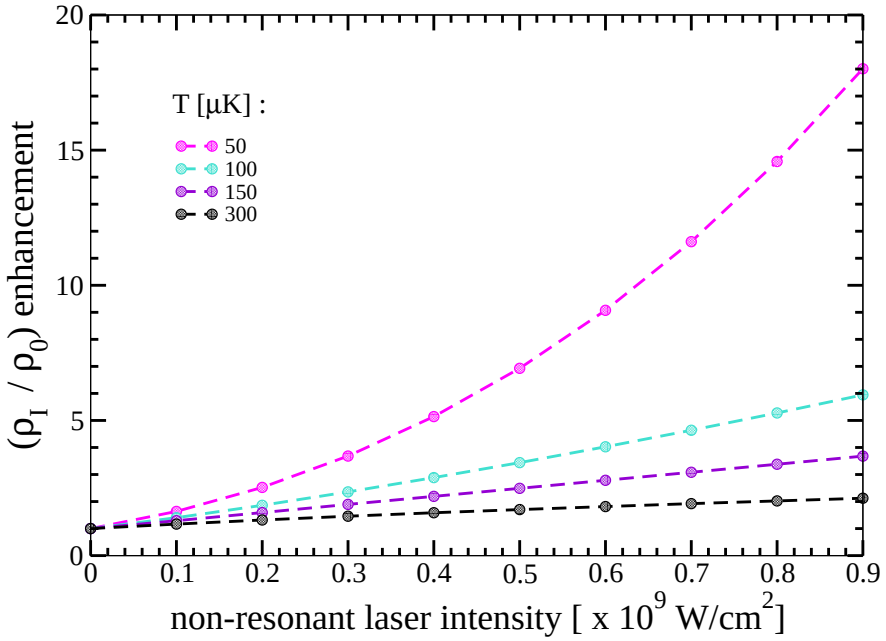

Figure 5.15: Initial pair density enhancement in 1D by using $^{87}Rb_2$ a $^3\Sigma_u$(5s+5s) lowest triplet potential energy surface. Each curve represents enhancement in the initial pair distribution which is calculated by taking the ratio of the field-dressed (ρ_I) and field-free (ρ_0) pair densities given in Eq. 3.26 for each applied non-resonant field intensity at 85 bohr inter-nuclear separation; where the photoassociation is most favorable. When the trap temperatures 300, 150, 100 and 50 μK are considered (black, violet, turquoise, magenta curves, respectively), the highest pair density enhancement is found to occur for the lowest temperature, 50 μK.

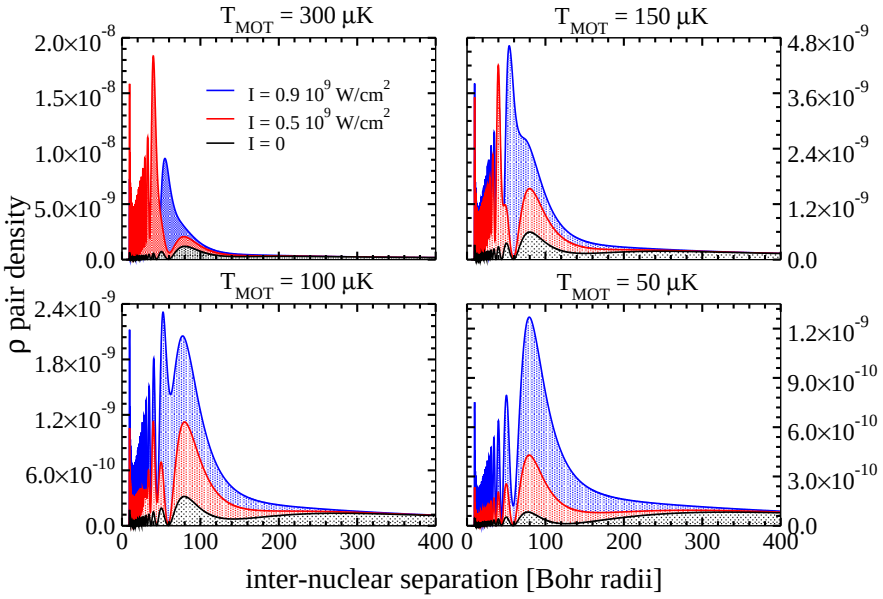

Figure 5.16: Pair densities on $^{87}Rb_2$ a $^3\Sigma_u$(5s+5s) lowest triplet potential surface for the cases field-free, I = 0.5 10^9 and I = 0.9 10^9 W/cm^2 non-resonant field intensities calculated with respect to Eq. 3.26 (black, red and blue curves, respectively) for the trap temperatures 300, 150, 100 and 50 μK.

and corresponding optimal pulse width. This usually corresponds to a few picoseconds for transform limited pulses, but it can be longer for shaped, e.g. chirped pulses.

Rotational period of the last bound level of $^{87}Rb_2 a^3\Sigma_u^+$ triplet lowest potential is found to be 82 ns and rotational period of $^{88}Sr_2 X^1\Sigma_g^+$ is found to be 36.5 ns. Although it is difficult to attribute rotational period to regular scattering states, quasi-bound character of the shape resonance allows to defining its rotational period. The rotational periods are calculated to be 2 ms for d-wave and 350 ns for g-wave field-free resonances of the mentioned potential energy surfaces, respectively. During the laser control, the modified lifetime of the resonant state should stay sufficiently long in order to allow adiabatic switching of the non-resonant laser field. From Fig. 5.6 it can be seen that the lifetime of the d-wave resonance of Rb_2 is on the order of hundreds of ns, and from Fig. 5.8 the lifetime of the g-wave resonance of Sr_2 is on the order of microseconds. Thus, in both cases it seems that picosecond pulses should be sufficiently short to profit from the population accumulated at short range to produce a large number of molecules to enhance the photoassociation probability as compared to the case without resonant enhancement.

5.6 Conclusion and Outlook

In this chapter of the thesis naturally existing shape resonances of alkaline and alkaline earth dimers are manipulated by employing non-resonant external lasers in order to increase the initial atomic pair density close to the inter-nuclear separations where photoassociation is feasible. The effect of the non-resonant laser brings the energy of the resonant state close to the energies those corresponding to the typical MOT temperatures of the system. Thus, the thermal weight of a shape resonance is amplified and initial pair density is enhanced. Firstly, this effect is explained in terms of 1D models where the effect of the non-resonant field is stored within the rotational barrier. Application of the field lowers the barrier height and thus the position of the resonance. However, the rotational mixing caused by the intermediate and high laser amplitudes is not fully covered by the 1D model. By including the angular degree

of freedom the model is extended to 2D and the effect of rotational mixing is covered. The decisive parameter of feasibility for photoassociation is the rotational period in this system. A shape resonance is a quasi-bound state with a finite lifetime. In order to achieve enhanced photoassociation in this scheme, the lifetime of the resonance is desired to be longer than the rotational period. Therefore, the feasibility analysis is done for lifetime as well as the resonance position as a function of applied non-resonant laser intensity. The effect of the time scale of non-resonant laser is also studied. In the adiabatic scheme, the initial atomic ensemble follows the field adiabatically, e.g. the field-free states of the system turn into field-dressed states adiabatically and the process is reversible. In the other hand, non-adiabatic dynamics are observed when a shorter laser pulse compared to the rotational period of the system is applied onto the atomic ensemble. The effect of these short pulses is studied in terms of pulse intensity and the pulse duration. By applying a prior laser to the initial atomic ensemble, more than an order of magnitude enhancement is obtained in the initial pair density. The enhancement is mainly restricted by the rotational mixing of the states with non-resonant character. In this study, the effect of the field is studied via one pure state which represents energetically the best the MOT. By employing polarization effects to the system is planned to be studied. Thus, a coherent control scheme with many control knobs is aimed to be developed.

Acknowledgements

It is my pleasure to thank the people and the organizations who made this dissertation possible.

I am truly indebted and thankful to the Physics Department of the Freie Universität Berlin for giving me the support I needed to complete my Ph.D. studies. I would like to thank Dr. Roland Mitrić for taking over the supervision of my studies and for stimulating discussions. I would like to thank Prof. Dr. Christiane Koch for her guidance and for making it possible to start my Ph.D. studies in Berlin. This Ph.D. work would not have been finished without the support of Prof. Dr. Ludger Wöste. I also thank him for giving me the opportunity to collaborate with his group. During this collaboration I had the chance to work with very nice colleagues from the AG Wöste. In particular I would like to mention Dr. Albrect Lindinger, Dr. Andrea Merli, Dr. Fabian Weise and Frau Frauke Eimer who carried out the femtosecond photoassociation experiments together with other AG Wöste co-workers. I would like to also thank Dr. Cristina Stanca-Kaposta for fruitful discussions.

I would also like to warmly thank Prof. Dr. Bretislav Friedrich and Dr. Mikhail Lemeshko for the inspiring discussions on controlling a shape resonance with non-resonant lasers. I would like to acknowledge Dr. Rosario González-Férez for her contributions to the computer code which included a rotational degree of freedom.

I thank the members of the dissertation committee for the time they have invested in evaluating this thesis.

I would like to gratefully acknowledge Gabriele and Dieter Herrmann for their help and warm friendship during my stay in Berlin.

The guidance and help of the women's representative of our department Dr. Beate Schattat has been vital to the accomplishment of this dissertation, together with all kinds of administrative support of Frau Angelica Pasanec from the Ph.D. and Habilitation Office.

I wish to thank Prof. Dr. Piet Brouwer for hosting me with great hospitality during the last months of my stay in his group. I thank to Prof. Dr. E.K.U. Gross for the opportunity to join in on the fruitful discussions in his coffee seminars. My time at the Freie Universität Berlin was made enjoyable, in a large part by many friends and colleagues that I spent time with. I am grateful for the time spent with my roommates Herr Christian Schwenke, Dr. Mamadou Ndong, Dr. Tobias Micklitz and friends Frau Mónika Hejjas, Frau Monika Pawlowska, Dr. Angelica Zacarias and members of AG Gross.

I would also like to express my gratitude to Dr. Jordi Mur-Petit for constructive discussions and for his support as a friend as well as a colleague.

For technical assistance with the computer systems, I would like to acknowledge Herr Jens Dreger, Herr Philipp Neuser and Herr Andreas Ziehm from ZEDV and Dr. Loris Bennett from ZEDAT.

My Ph.D. study was generously financed by the German Research Foundation (DFG), the Dahlem Research School, the Physics Department and the Women's Fund of the Physics Department of the Freie Universität Berlin.

Finally, my warmest thanks goes to my mother Münire Küçükçalık and to my father Mehmet Naci Ağanoğlu for their lifelong support.

Publications

Frauke Eimer, Fabian Weise, Andrea Merli, Sascha Birkner, Franziska Sauer, Ludger Wöste, Albrecht Lindinger, Ruzin Ağanoğlu, Christiane P. Koch, Wenzel Salzmann, Terry Mullins, Simone Götz, Roland Wester, Matthias Weidemüller: *Spectrally resolved coherent transient signal for ultracold rubidium molecules*, Eur. Phys. J. D. 54, 711 - 714 (2009).

Andrea Merli, Frauke Eimer, Fabian Weise, Albrecht Lindinger, Wenzel Salzmann, Terry Mullins, Simone Götz, Roland Wester, Matthias Weidemüller, Ruzin Ağanoğlu, Christiane P. Koch: *Photoassociation and coherent transient dynamics in the interaction of ultracold rubidium atoms with shaped femtosecond pulses. II. Theory*, Phys. Rev. A, 80, 063417 (2009).

Fabian Weise, Andrea Merli, Frauke Eimer, Sascha Birkner, Franziska Sauer, Ludger Wöste, Albrecht Lindinger, Wenzel Salzmann, Terence G. Mullins, Roland Wester, Matthias Weidemüller, Ruzin Ağanoğlu, Christiane P. Koch: *Characteristic oscillations in the coherent transients of ultracold rubidium molecules using red and blue detuned pulses for photoassociation*, J. Phys. B, 42 , 215307 (2009).

Ruzin Ağanoğlu, Mikhail Lemeshko, Bretislav Friedrich, Rosario González-Férez, Christiane P. Koch: *Controlling a diatomic shape resonance with non-resonant light*, arXiv:1105.0761v1 [physics.atom-ph] (2011)

Short Curriculum Vitae

The resume is not available online for data protection reasons.

Der Lebenslauf ist in der Online-Version aus Gründen des Datenschutzes nicht enthalten.

References

ALMAZOR, M.L., DULIEU, O., MASNOU-SEEUWS, F., BEUC, R. & PICHLER, G. (2001). Formation of ultracold molecules via photoassociation with blue detuned laser light. *The European Physical Journal D - Atomic, Molecular, Optical and Plasma Physics*, **15**, 355–363, 10.1007/s100530170152. 27

APPLEQUIST, J., CARL, J.R. & FUNG, K.K. (1972). Atom dipole interaction model for molecular polarizability. application to polyatomic molecules and determination of atom polarizabilities. *Journal of the American Chemical Society*, **94**, 2952–2960. 13, 14

ATKINS, P.W. & FRIEDMAN, R.S. (2010). *Molecular Quantum Mechanics*. Oxford University Press, USA, 5th edn. 10, 12

AĞANOĞLU, R., LEMESHKO, M., FRIEDRICH, B., GONZÁLEZ-FÉREZ, R. & KOCH, C.P. (2011). Controlling a diatomic shape resonance with non-resonant light. *arXiv:1105.0761v1 [physics.atom-ph]*. 22, 26, 68, 70, 75, 76

AVERBUKH, I. & PERELMAN, N. (1989). Fractional revivals: Universality in the long-term evolution of quantum wave packets beyond the correspondence principle dynamics. *Physics Letters A*, **139**, 449 – 453. 83

BALINT-KURTI, G.G., DIXON, R.N. & MARSTON, C.C. (1992). Grid methods for solving the schrödinger equation and time dependent quantum dynamics of molecular photofragmentation and reactive scattering processes. *International Reviews in Physical Chemistry*, **11**, 317–344. 15

BAČIĆ, Z. & LIGHT, J.C. (1989). Theoretical Methods for Rovibrational States of Floppy Molecules. *Annu. Rev. Phys. Chem.*, **40**, 469–498. 72

BETHLEM, H.L., BERDEN, G., CROMPVOETS, F.M.H., JONGMA, R.T., VAN ROIJ, A.J.A. & MEIJER, G. (2000). Electrostatic trapping of ammonia molecules. *Nature*, **402**, 491–494. 67

BOESTEN, H.M.J.M., TSAI, C.C., VERHAAR, B.J. & HEINZEN, D.J. (1996). Observation of a shape resonance in cold-atom scattering by pulsed photoassociation. *Phys. Rev. Lett.*, **77**, 5194–5197. 67

BOESTEN, H.M.J.M., TSAI, C.C., GARDNER, J.R., HEINZEN, D.J. & VERHAAR, B.J. (1997). Observation of a shape resonance in the collision of two cold $rb87$ atoms. *Phys. Rev. A*, **55**, 636–640. 67

BORISOV, A.G. (2001). Solution of the radial schrdinger equation in cylindrical and spherical coordinates by mapped fourier transform algorithms. *Journal of Chemical Physics*, **114**, 7770–7777. 20

BÖTTCHER, C.J.F. (1973). *Theory of Electric Polarization, Vol. I-II*. Elsevier, Amsterdam. 13

BÜCHLER, H.P., DEMLER, E., LUKIN, M., MICHELI, A., PROKOF'EV, N., PUPILLO, G. & ZOLLER, P. (2007). Strongly correlated 2d quantum phases with cold polar molecules: Controlling the shape of the interaction potential. *Phys. Rev. Lett.*, **98**, 060404. 26

BURNETT, K., JULIENNE, P.S., LETT, P.D., TIESINGA, E. & WILLIAMS, C.J. (2002). Quantum encounters of the cold kind. *Nature*, **416**, 225–232. 25, 26

CARR, L.D., DEMILLE, D., KREMS, R.V. & YE, J. (2009). Cold and ultracold molecules: science, technology and applications. *New Journal of Physics*, **11**, 055049. 26

CHAKRABORTY, D., HAZRA, J. & DEB, B. (2011). Resonant enhancement of the ultracold photoassociation rate by an electric field-induced anisotropic interaction. *Journal of Physics B: Atomic, Molecular and Optical Physics*, **44**, 095201. 26

CHANG, T.Y. (1967). Moderately long-range interatomic forces. *Rev. Mod. Phys.*, **39**, 911–942. 4

COHEN-TANNOUDJI, C., DIU, B., LALOE, F. & DUI, B. (2006). *Quantum Mechanics (2 vol. set)*. Wiley-Interscience. 4, 10

COOLEY, J.W. & TUKEY, J.W. (1965). An algorithm for the machine calculation of complex fourier series. *Mathematics of Computation*, **19**, pp. 297–301. 18

DASHEVSKAYA, E.I., VORONIN, A.I. & NIKITIN, E.E. (1969). Theory of excitation transfer in collisions between alkali atoms. i. identical partners. *Canadian Journal of Physics*, **47**, 1237–1248. 5

DEIGLMAYR, J., AYMAR, M., WESTER, R., WEIDEMÜLLER, M. & DULIEU, O. (2008). Calculations of static dipole polarizabilities of alkali dimers: Prospects for alignment of ultracold molecules. *J. Chem. Phys.*, **129**, 064309. xviii, 69, 70

DEVOE, H. (1965). Optical properties of molecular aggregates. ii. classical theory of the refraction, absorption, and optical activity of solutions and crystals. *Journal of Chemical Physics*, **43**, 3199–3208. 13

DION, C.M., DRAG, C., DULIEU, O., LABURTHE TOLRA, B., MASNOU-SEEUWS, F. & PILLET, P. (2001). Resonant coupling in the formation of ultracold ground state molecules via photoassociation. *Phys. Rev. Lett.*, **86**, 2253–2256. 2, 25

DOOLEY, P.W., LITVINYUK, I.V., LEE, K.F., RAYNER, D.M., SPANNER, M., VILLENEUVE, D.M. & CORKUM, P.B. (2003). Direct imaging of rotational wave-packet dynamics of diatomic molecules. *Phys. Rev. A*, **68**, 023406. 3

DUDOVICH, N., ORON, D. & SILBERBERG, Y. (2002). Coherent transient enhancement of optically induced resonant transitions. *Phys. Rev. Lett.*, **88**, 123004. 43, 56

EIMER, F., WEISE, F., MERLI, A., BIRKNER, S., SAUER, F., WÖSTE, L., LINDINGER, A., AĞANOĞLU, R., KOCH, C.P., SALZMANN, W., MULLINS, T., GÖTZ, S., WESTER, R. & WEIDEMÜLLER, M. (2009). Spectrally resolved coherent transient signal for ultracold rubidium molecules. *The European Physical Journal D - Atomic, Molecular, Optical and Plasma Physics*, **54**, 711–714, 10.1140/epjd/e2009-00212-8. 3, 30, 61

FATTAL, E., BAER, R. & KOSLOFF, R. (1996). Phase space approach for optimizing grid representations: The mapped fourier method. *Phys. Rev. E*, **53**, 1217–1227. 17, 18

FERRARI, G., DRULLINGER, R.E., POLI, N., SORRENTINO, F. & TINO, G.M. (2006a). Cooling of sr to high phase-space density by laser and sympathetic cooling in isotopic mixtures. *Phys. Rev. A*, **73**, 023408. 69

FERRARI, G., POLI, N., SORRENTINO, F. & TINO, G.M. (2006b). Long-lived bloch oscillations with bosonic sr atoms and application to gravity measurement at the micrometer scale. *Phys. Rev. Lett.*, **97**, 060402. 69

FIORETTI, A., COMPARAT, D., CRUBELLIER, A., DULIEU, O., MASNOU-SEEUWS, F. & PILLET, P. (1998). Formation of cold $cs2$ molecules through photoassociation. *Phys. Rev. Lett.*, **80**, 4402–4405. 25

FLAMBAUM, V.V. & KOZLOV, M.G. (2007). Enhanced sensitivity to the time variation of the fine-structure constant and m_p/m_e in diatomic molecules. *Phys. Rev. Lett.*, **99**, 150801. 26

FLEISCHER, S., KHODORKOVSKY, Y., PRIOR, Y. & AVERBUKH, I.S. (2009). Controlling the sense of molecular rotation. *New Journal of Physics*, **11**, 105039. 24

GABBANINI, C., FIORETTI, A., LUCCHESINI, A., GOZZINI, S. & MAZZONI, M. (2000). Cold rubidium molecules formed in a magneto-optical trap. *Phys. Rev. Lett.*, **84**, 2814–2817. 25

GAO, B. (1998). Quantum-defect theory of atomic collisions and molecular vibration spectra. *Phys. Rev. A*, **58**, 4222–4225. 69

GAO, B. (2009). Analytic description of atomic interaction at ultracold temperatures: The case of a single channel. *Phys. Rev. A*, **80**, 012702. 69

GONZÁLEZ-FÉREZ, R. & SCHMELCHER, P. (2005a). Electric-field-induced adiabaticity in the rovibrational motion of heteronuclear diatomic molecules. *Phys. Rev. A*, **71**, 033416. 24

GONZÁLEZ-FÉREZ, R. & SCHMELCHER, P. (2005b). Rotation-vibration mixing of heteronuclear dimers in strong electric fields. *Europhys. Lett.*, **72**, 555–561. 24, 80

GONZÁLEZ-FÉREZ, R. & SCHMELCHER, P. (2009). Impact of electric fields on highly excited rovibrational states of polar dimers. *New Journal of Physics*, **11**, 055013. 75

GOTTLIEB, D. & ORSZAG, S.A. (2009). *Numerical analysis of spectral methods: Theory and applications.*. Pa: Soc. for Industrial and Applied Mathematics, Philadelphia. 17

HERZBERG, G. (1989). *Molecular Spectra and Molecular Structure*, vol. I. Robert E. Krieger Publishing Company, Florida. 86

JONES, K.M., TIESINGA, E., LETT, P.D. & JULIENNE, P.S. (2006). Ultracold photoassociation spectroscopy: Long-range molecules and atomic scattering. *Rev. Mod. Phys.*, **78**, 483–535. 5, 26, 29

JULIENNE, P.S. (1996). Cold binary atomic collisions in a light field. *Journal of Research of the National Institute of Standards and Technology*, **101**. 27

JULIENNE, P.S. (2009). Ultracold molecules from ultracold atoms: a case study with the krb molecule. *Faraday Discuss.*, **142**, 361–388. 25

JULIENNE, P.S. & VIGUÉ, J. (1991). Cold collisions of ground- and excited-state alkali-metal atoms. *Phys. Rev. A*, **44**, 4464–4485. 5

KALLUSH, S. & KOSLOFF, R. (2006). Improved methods for mapped grids: Applied to highly excited vibrational states of diatomic molecules. *Journal of Chemical Physics*, **433**, 221 – 227. 19

KOCH, C.P., KOSLOFF, R., LUC-KOENIG, E., MASNOU-SEEUWS, F. & CRUBELLIER, A. (2006a). Photoassociation with chirped laser pulses: calculation of the absolute number of molecules per pulse. *Journal of Physics B: Atomic, Molecular and Optical Physics*, **39**, S1017. 22, 23, 91

KOCH, C.P., KOSLOFF, R. & MASNOU-SEEUWS, F.M.C. (2006b). Short-pulse photoassociation in rubidium below the d_1 line. *Phys. Rev. A*, **73**, 043409. 2, 91

KOCH, C.P., LUC-KOENIG, E. & MASNOU-SEEUWS, F.M.C. (2006c). Making ultracold molecules in a two-color pump-dump photoassociation scheme using chirped pulses. *Phys. Rev. A*, **73**, 033408. 29, 91

KOKOOULINE, V., DULIEU, O., KOSLOFF, R. & MASNOU-SEEUWS, F. (1999). Mapped fourier methods for long-range molecules: Application to perturbations in the rb(0_u^+) photoassociation spectrum. *The Journal of Chemical Physics*, **110**, 9865–9876. 18

KOSLOFF, R. (1988). Time-dependent quantum-mechanical methods for molecular dynamics. *The Journal of Physical Chemistry*, **92**, 2087–2100. 15, 18, 20

KOSLOFF, R. (1994). Propagation methods for quantum molecular dynamics. *Annual Review of Physical Chemistry*, **45**, 145–178. 20

KREMS, R.V. (2006). Controlling collisions of ultracold atoms with dc electric fields. *Phys. Rev. Lett.*, **96**, 123202. 66

LANDAU, L.D. & LIFSHITZ, E.M. (1980). *Statistical Physics, Third Edition, Part 1: Volume 5 (Course of Theoretical Physics, Volume 5)*. Butterworth-Heinemann, 3rd edn. 22

LEFORESTIER, C., BISSELING, R.H., CERJAN, C., FEIT, M.D., FRIESNER, R., GULDBERG, A., HAMMERICH, A., JOLICARD, G., KARRLEIN, W., MEYER, H.D., LIPKIN, N., RONCERO, O. & KOSLOFF, R. (1991). A comparison of different propagation schemes for the time dependent schroedinger equation. *Journal of Computational Physics*, **94**, 59 – 80. 20

LEMESHKO, M. & FRIEDRICH, B. (2009). Probing weakly bound molecules with nonresonant light. *Phys. Rev. Lett.*, **103**, 053003. 3, 68, 72, 73

LEMESHKO, M. & FRIEDRICH, B. (2010). Fine-tuning molecular energy levels by nonresonant laser pulses. *The Journal of Physical Chemistry A*, **114**, 9848–9854. 76, 83

LEMOINE, D. (2000). Optimized grid representations in curvilinear coordinates: the mapped sine fourier method. *Chemical Physics Letters*, **320**, 492 – 498. 20

LEROY, R.J. & BERNSTEIN, R.B. (1970). Dissociation energy and long-range potential of diatomic molecules from vibrational spacings of higher levels. *J. Chem. Phys*, **52**, 3869–3879. 5

LETT, P.D., HELMERSON, K., PHILLIPS, W.D., RATLIFF, L.P., ROLSTON, S.L. & WAGSHUL, M.E. (1993). Spectroscopy of $na2$ by photoassociation of laser-cooled na. *Phys. Rev. Lett.*, **71**, 2200–2203. 25

LI, Z. & KREMS, R.V. (2007). Electric-field-induced feshbach resonances in ultracold alkali-metal mixtures. *Phys. Rev. A*, **75**, 032709. 66

LIDE, D.R., ed. (2003). *CRC handbook of chemistry and physics*. CRC Press LLC, 84th edn. 69

LIGHT, J.C., HAMILTON, I.P. & LILL, J.V. (1985). Generalized discrete variable approximation in quantum mechanics. *J. Chem. Phys.*, **82**, 1400–1409. 72

LONDOÑO, B.E., MAHECHA, J.E., LUC-KOENIG, E. & CRUBELLIER, A. (2010). Shape resonances in ground-state diatomic molecules: General trends and the example of rbcs. *Phys. Rev. A*, **82**, 012510. 67, 69, 74, 80

LUC-KOENIG, E., KOSLOFF, R., MASNOU-SEEUWS, F. & VATASESCU, M. (2004). Photoassociation of cold atoms with chirped laser pulses: Time-dependent calculations and analysis of the adiabatic transfer within a two-state model. *Phys. Rev. A*, **70**, 033414. 54

MACHHOLM, M., GIUSTI-SUZOR, A. & MIES, F.H. (1994). Photoassociation of atoms in ultracold collisions probed by wave-packet dynamics. *Phys. Rev. A*, **50**, 5025–5036. 2, 22

MANDELSHTAM, V.A. & TAYLOR, H.S. (1997). A low-storage filter diagonalization method for quantum eigenenergy calculation or for spectral analysis of time signals. *J. Chem. Phys.*, **106**, 5085–5090. 45

MARGENAU, H. (1939). Van der waals forces. *Rev. Mod. Phys.*, **11**, 1–35. 4

MARINESCU, M. & DALGARNO, A. (1995). Dispersion forces and long-range electronic transition dipole moments of alkali-metal dimer excited states. *Phys. Rev. A*, **52**, 311–328. 5

MARINESCU, M. & YOU, L. (1998). Controlling atom-atom interaction at ultralow temperatures by dc electric fields. *Phys. Rev. Lett.*, **81**, 4596–4599. 66

MARTE, A., VOLZ, T., SCHUSTER, J., DÜRR, S., REMPE, G., VAN KEMPEN, E.G.M. & VERHAAR, B.J. (2002). Feshbach resonances in rubidium 87: Precision measurement and analysis. *Phys. Rev. Lett.*, **89**, 283202. 35, 69

MASNOU-SEEUWS, F. & PILLET, P. (2001a). Formation of ultracold molecules. *Advances in Atomic, Molecular, and Optical Physics*, **47**. 29

MASNOU-SEEUWS, F. & PILLET, P. (2001b). Formation of ultracold molecules ($t <= 200\mu k$) via photoassociation in a gas of laser-cooled atoms. *Advances In Atomic, Molecular, and Optical Physics*, **47**, 53 – 127. 5

MEATH, W.J. (1972). The structure of the multipole treatment of intermolecular forces. *American Journal of Physics*, **40**, 21–27. 5

MERLI, A., EIMER, F., WEISE, F., LINDINGER, A., SALZMANN, W., MULLINS, T., GÖTZ, S., WESTER, R., WEIDEMÜLLER, M., AĞANOĞLU, R. & KOCH, C.P. (2009). Photoassociation and coherent transient dynamics in the interaction of ultracold rubidium atoms with shaped femtosecond pulses. ii. theory. *Phys. Rev. A*, **80**, 063417. xiii, 3, 30, 32, 43, 49, 50, 55

MICHELI, A., BRENNEN, G.K. & ZOLLER, P. (2006). A toolbox for lattice-spin models with polar molecules. *Nature Physics*, **2**, 341–347. 26

MICKELSON, P.G., MARTINEZ DE ESCOBAR, Y.N., YAN, M., DESALVO, B.J. & KILLIAN, T.C. (2010). Bose-einstein condensation of $sr88$ through sympathetic cooling with $sr87$. *Phys. Rev. A*, **81**, 051601. 69

MILLER, J.D., CLINE, R.A. & HEINZEN, D.J. (1993). Photoassociation spectrum of ultracold rb atoms. *Phys. Rev. Lett.*, **71**, 2204–2207. 25

MITRIĆ, R., BONAČIĆ-KOUTECKÝ, V., PITTNER, J. & LISCHKA, H. (2006). Ab initio nonadiabatic dynamics study of ultrafast radiationless decay over conical intersections illustrated on the na3f cluster. *J. Chem. Phys.*, **125**, 024303. 83

MONMAYRANT, A., CHATEL, B. & GIRARD, B. (2006). Quantum state measurement using coherent transients. *Phys. Rev. Lett.*, **96**, 103002. 43

MOVRE, M. & PICHLER, G. (1977). Resonance interaction and self-broadening of alkali resonance lines. i. adiabatic potential curves. *Journal of Physics B: Atomic and Molecular Physics*, **10**, 2631. 5

MULLINS, T., SALZMANN, W., GÖTZ, S., ALBERT, M., ENG, J., WESTER, R., WEIDEMÜLLER, M., WEISE, F., MERLI, A., WEBER, S.M., SAUER, F., WÖSTE, L. & LINDINGER, A. (2009). Photoassociation and coherent transient dynamics in the interaction of ultracold rubidium atoms with shaped femtosecond pulses. i. experiment. *Phys. Rev. A*, **80**, 063416. x, 30, 31, 32, 46

NAGEL, S.B., MICKELSON, P.G., SAENZ, A.D., MARTINEZ, Y.N., CHEN, Y.C., KILLIAN, T.C., PELLEGRINI, P. & CÔTÉ, R. (2005). Photoassociative spectroscopy at long range in ultracold strontium. *Phys. Rev. Lett.*, **94**, 083004. 69

NEUHAUSER, D. (1990). Bound state eigenfunctions from wave packets: Time-energy resolution. *J. Chem. Phys.*, **93**, 2611–2616. 45

NIKOLOV, A.N., EYLER, E.E., WANG, X.T., LI, J., WANG, H., STWALLEY, W.C. & GOULD, P.L. (1999). Observation of ultracold ground-state potassium molecules. *Phys. Rev. Lett.*, **82**, 703–706. 25

NIKOLOV, A.N., ENSHER, J.R., EYLER, E.E., WANG, H., STWALLEY, W.C. & GOULD, P.L. (2000). Efficient production of ground-state potassium molecules at sub-mk temperatures by two-step photoassociation. *Phys. Rev. Lett.*, **84**, 246–249. 25

ORTIGOSO, J., RODRÍGUEZ, M., GUPTA, M. & FRIEDRICH, B. (1999). Time evolution of pendular states created by the interaction of molecular polarizability with a pulsed nonresonant laser field. *J. Chem. Phys*, **110**, 3870–3875. 3

OSPELKAUS, S., NI, K.K., WANG, D., DE MIRANDA, M.H.G., NEYENHUIS, B., QUÉMÉNER, G., JULIENNE, P.S., BOHN, J.L., JIN, D.S. & YE, J. (2010). Quantum-state controlled chemical reactions of ultracold potassium-rubidium molecules. *Science*, **327**, 853–857. 25

OWSCHIMIKOW, N., SCHMIDT, B. & SCHWENTNER, N. (2009). State selection in nonresonantly excited wave packets by tuning from nonadiabatic to adiabatic interaction. *Phys. Rev. A*, **80**, 053409. 83

PARK, S.J., SUH, S.W., LEE, Y.S. & JEUNG, G.H. (2001). Theoretical study of the electronic states of the rb2 molecule. *Journal of Molecular Spectroscopy*, **207**, 129 – 135. 35, 69

PELLEGRINI, P., GACESA, M. & CÔTÉ, R. (2008). Giant formation rates of ultracold molecules via feshbach-optimized photoassociation. *Phys. Rev. Lett.*, **101**, 053201. 66

PERSHAN, P.S., VAN DER ZIEL, J.P. & MALMSTROM, L.D. (1966). Theoretical discussion of the inverse faraday effect, raman scattering, and related phenomena. *Phys. Rev.*, **143**, 574–583. 71

POSCHINGER, U., SALZMANN, W., WESTER, R., WEIDEMÜLLER, M., KOCH, C.P. & KOSLOFF, R. (2006). Theoretical model for ultracold molecule formation via adaptive feedback control. *Journal of Physics B: Atomic, Molecular and Optical Physics*, **39**, S1001. 38

RISS, U.V. & MEYER, H.D. (1993). Calculation of resonance energies and widths using the complex absorbing potential method. *Journal of Physics B: Atomic, Molecular and Optical Physics*, **26**, 4503. 73

SALZMANN, W., POSCHINGER, U., WESTER, R., WEIDEMÜLLER, M., MERLI, A., WEBER, S.M., SAUER, F., PLEWICKI, M., WEISE, F., ESPARZA, A.M., WÖSTE, L. & LINDINGER, A. (2006). Coherent control with shaped femtosecond laser pulses applied to ultracold molecules. *Phys. Rev. A*, **73**, 023414. 32

SALZMANN, W., MULLINS, T., ENG, J., ALBERT, M., WESTER, R., WEIDEMÜLLER, M., MERLI, A., WEBER, S.M., SAUER, F., PLEWICKI, M., WEISE, F., WÖSTE, L. & LINDINGER, A. (2008). Coherent transients in the femtosecond photoassociation of ultracold molecules. *Phys. Rev. Lett.*, **100**, 233003. 30, 32

SHAPIRO, M. & BRUMER, P. (2003). *Principles of the Quantum Control of Molecular Processes*. Wiley Interscience, New York. 29, 38

SILBERSTEIN, L. (1917). Vii. molecular refractivity and atomic interaction. *Philosophical Magazine Series 6*, **33**, 92–128. 13, 14

STEIN, A., KNÖCKEL, H. & TIEMANN, E. (2008). Fourier-transform spectroscopy of $sr2$ and revised ground-state potential. *Phys. Rev. A*, **78**, 042508. 69

STWALLEY, W.C., UANG, Y.H. & PICHLER, G. (1978). Pure long-range molecules. *Phys. Rev. Lett.*, **41**, 1164–1167. 5

STWALLEY, W.C., GOULD, P.L. & EYLER, E.E. (2009). *Ultracold Molecule Formation by Photoassociation*. CRC Press. 26

TAL-EZER, H., KOSLOFF, R. & CERJAN, C. (1992). Low-order polynomial approximation of propagators for the time-dependent schroedinger equation. *Journal of Computational Physics*, **100**, 179 – 187. 20

TANNOR, D.J. (2007). *Introduction to Quantum Mechanics A Time-Dependent Perspective*. University Science Press, Sausalito. 20

THORSHEIM, H.R., WEINER, J. & JULIENNE, P.S. (1987). Laser-induced photoassociation of ultracold sodium atoms. *Phys. Rev. Lett.*, **58**, 2420–2423. 25

TOWNSEND, C.G., EDWARDS, N.H., ZETIE, K.P., COOPER, C.J., RINK, J. & FOOT, C.J. (1996). High-density trapping of cesium atoms in a dark magneto-optical trap. *Phys. Rev. A*, **53**, 1702–1714. 30

VALA, J., DULIEU, O., MASNOU-SEEUWS, F., PILLET, P. & KOSLOFF, R. (2000). Coherent control of cold-molecule formation through photoassociation using a chirped-pulsed-laser field. *Phys. Rev. A*, **63**, 013412. 29, 54

VARDI, A., ABRASHKEVICH, D., FRISHMAN, E. & SHAPIRO, M. (1997). Theory of radiative recombination with strong laser pulses and the formation of ultracold molecules via stimulated photo-recombination of cold atoms. *The Journal of Chemical Physics*, **107**, 6166–6174. 29

WANG, H., GOULD, P.L. & STWALLEY, W.C. (1997). Long-range interaction of the 39k(4s)+39k(4p) asymptote by photoassociative spectroscopy. i. the 0g pure long-range state and the long-range potential constants. *J. Chem. Phys.*, **106**, 7899–7912. 35

WEISE, F., MERLI, A., EIMER, F., BIRKNER, S., SAUER, F., WÖSTE, L., LINDINGER, A., SALZMANN, W., MULLINS, T.G., WESTER, R., WEIDEMÜLLER, M., AĞANOĞLU, R. & KOCH, C.P. (2009). Characteristic oscillations in the coherent transients of ultracold rubidium molecules using red and blue detuned pulses for photoassociation. *Journal of Physics B: Atomic, Molecular and Optical Physics*, **42**, 215307. xiv, 3, 30, 52

WILLNER, K., DULIEU, O. & MASNOU-SEEUWS, F. (2004). Mapped grid methods for long-range molecules and cold collisions. *Chemical Physics Letters*, **120**, 548–561. 20

WOHLGEMUTH, M., BONAČIĆ-KOUTECKÝ, V. & MITRIĆ, R. (2011). Time-dependent density functional theory excited state nonadiabatic dynamics combined with quantum mechanical/molecular mechanical approach: Photodynamics of indole in water. *J. Chem. Phys.*, **135**, 054105. 83

WYATT, R.E. & ZHANG, J.Z.H., eds. (1996). *Dynamics of Molecules and Chemical Reactions*. Taylor & Francis, New York. 15, 17

ZELEVINSKY, T., BOYD, M.M., LUDLOW, A.D., IDO, T., YE, J., CIURYŁO, R., NAIDON, P. & JULIENNE, P.S. (2006). Narrow line photoassociation in an optical lattice. *Phys. Rev. Lett.*, **96**, 203201. 78

ZELEVINSKY, T., BLATT, S., BOYD, M.M., CAMPBELL, G.K., LUDLOW, A.D. & YE, J. (2008). Highly coherent spectroscopy of ultracold atoms and molecules in optical lattices. *ChemPhysChem*, **9**, 375–382. 69

ZEWAIL, A.H. (2000). Femtochemistry: Atomic-scale dynamics of the chemical bond. *The Journal of Physical Chemistry A*, **104**, 5660–5694. 29